

Silicon photonics based MEMS tunable polarization rotator for optical communications

SANDIPAN DAS



KTH Electrical Engineering

Master's Degree Project in
Micro and Nanosystems
Second level, 30 ECTS
Stockholm, Sweden July, 2016



KTH Electrical Engineering

Silicon photonics based MEMS tunable polarization rotator for optical communications

Sandipan Das

Stockholm, July 7, 2016

Acknowledgement

I would like to thank many people who have helped me throughout the completion of this thesis work. The first and foremost are my parents and my wife, who have always supported and encouraged me patiently all along my work.

I am also thankful to my supervisor, Carlos Errando Herranz, who is captivating, honest, and has always believed in my abilities as well as guided me throughout the thesis work. I am also thankful to my examiner at KTH, Prof. Kristinn B. Gylfason, who has always provided his insightful comments on the thesis work and report drafts. I would also like to thank Prof. Norvald Stol, for being my supervisor at NTNU and keeping an eye on my progress. I am grateful to Prof. Mark Smith at KTH for sharing his experiences and running the Maskerspace at KTH Kista campus for all students, which instilled my research interests in integrated electronics.

I must also acknowledge the NordSecMob consortium for choosing me as a candidate for their generous scholarship, without which I could not have done my MSc studies at NTNU and KTH. My thanks must go also to the NordSecMob coordinators Aino Roms at Aalto University, Mona Nordaune at NTNU and May-Britt Eklund-Larsson at KTH, who have always helped me with all administrative matters throughout my studies.

Finally, I would also like to thank all the people in Micro and Nano Systems at KTH for making the work environment so friendly and relaxed, so that I could cultivate and nurture my thoughts during the thesis work.

Abstract

There has been a huge surge in data traffic all over the world due to the rise of streaming media services and connected devices. The current demand in data traffic has already pushed the optical fiber in the internet architecture to the network edges and the trend is to push it as close as possible, to the CPU. Silicon photonics addresses this challenge by enabling miniaturized optical devices that use light to move huge amounts of data at very high speeds with extremely low power. To further improve the data transmission capacity, one can make use of different polarizations of light. However, to take advantage of different polarizations, devices with on-chip polarization rotation capability are required. This is achieved by a tunable polarization rotator. Moreover, full control of polarization rotation can also be utilized to realize a new class of components in integrated photonics including polarization mode modulators, multiplexers, filters, as well as switches for advanced optical signal processing, coherent communications, and sensing.

This thesis introduces a novel tunable polarization rotator that uses microelectromechanical systems (MEMS) as its actuation principle. When voltage is applied to a MEMS tunable silicon cantilever, a mechanical movement occurs, which in turn affects the optical mode shape travelling through a waveguide, as a result of which the polarization is rotated. In this work, we have designed, fabricated, and characterized a MEMS tunable polarization rotator with a polarization extinction ratio of 10 dB, which works in 1530 nm - 1570 nm wavelength spectrum. In addition to the MEMS tunable polarization rotator, in this thesis, a free standing polarization beam splitter of length 1.4 μm , the shortest reported to-date to our knowledge, was designed, fabricated, and characterized. The tunable polarization rotator and beam splitter developed in this thesis have the potential to increase the bandwidth and flexibility of current optical communication networks, and find further applications in polarization diversity schemes for sensing.

Keywords: Silicon photonics, MEMS, Tunable polarization rotator, Polarization beam splitter

Contents

1	Introduction	1
1.1	Optical communication	1
1.2	Silicon photonics	3
1.3	Motivation for MEMS tunable polarization rotator	4
1.4	Objectives of the thesis	5
1.5	Outline of this thesis	5
2	Optical waveguide theory	6
2.1	Maxwell's equations	6
2.2	Transverse electromagnetic wave	8
2.3	Optical waveguides	8
2.3.1	Planar waveguides	9
2.3.2	Channel waveguides	10
2.4	Eigenvalues and wave modes	10
2.5	Polarization	11
2.5.1	TE mode	13
2.5.2	TM mode	13
2.5.3	Quasi-TE and Quasi-TM mode	13
2.6	Jones calculus	13
2.6.1	Jones vector	13
2.6.2	Jones matrix	14
2.6.3	Jones matrix for polarizing optical systems	14
2.6.3.1	Polarizer	15
2.6.3.2	Wave plates	15
2.7	Poincaré sphere and state of polarization	15
2.8	Stoke's parameter	16
2.9	Coupled mode theory	17
2.10	Figures of merit	19
2.10.1	Confinement factor	20
2.10.2	Polarization extinction ratio	20
2.10.3	Insertion loss	20
3	State of the art	21
3.1	Polarization rotator (PR)	21
3.2	Optical fiber PR	21

3.3	On-chip PR	22
3.3.1	Passive PR	22
3.3.1.1	Mode coupling	22
3.3.1.2	Mode evolution	24
3.3.1.3	Mode hybridization	25
3.3.2	Active PR	27
3.3.2.1	Tunable PR with thermo-optic effect	27
3.3.2.2	Tunable PR using Berry's phase	28
3.3.3	Other polarization tuning mechanisms	30
3.3.3.1	Thermal tuning	30
3.3.3.2	MEMS tuning	30
4	Design and simulation	31
4.1	Approach	31
4.2	Designing TPR	31
4.2.1	Design principle	31
4.2.2	Design: Mode hybridization based single stair Si waveguide with air cladding	32
4.2.2.1	Waveguide geometry	32
4.2.2.2	Optimized dimensions of primary PR waveguide	33
4.2.2.3	Optimized dimensions of MEMS waveguide	38
4.2.2.4	Design of primary PR waveguide with MEMS waveguide	39
4.2.2.5	Device tolerance	41
4.3	Designing auxiliary components for measurement setup	42
4.3.1	Grating coupler design	44
4.3.2	Taper with bridge design	44
4.3.3	Polarization beam splitter design	45
5	Fabrication	48
5.1	Piranha bath	48
5.2	HSQ resist spin	48
5.3	First e-beam exposure	48
5.4	First dry etch step	50
5.5	ZEP7000 spin	50
5.6	Second e-beam exposure	50
5.7	Second dry etch step	50
5.8	Wet etching and critical point drying	50
5.9	Fabricated product	51
6	Experiments	55
6.1	Unit tests	55
6.2	Characterization	56
6.2.1	Polarization beam splitter	56
6.2.2	Passive polarization rotator	57

6.2.3	Active polarization rotator	58
6.3	Analysis	61
7	Discussion	62
7.1	Limitations	63
7.2	Future work	63
8	Conclusions	65
Appendix A: Abbreviations		66
Appendix B: Code for graph generation		68
Bibliography		70

1

Chapter 1

Introduction

1.1 Optical communication

Communication and collective thinking are the key to the development of human civilization. This development is driven by data - “The new oil of this digital era”. With the rise of media streaming services, there has been a huge surge in data traffic all over the world. It has also been estimated that by 2020 there will be 38.5 billion connected Internet of Things (IoT) devices [1, 2], and all devices that can be connected will be connected. Ericsson’s mobility report [3] estimates that 70% of world’s population will use smart-phones by 2020 and 90% of the world’s population over 6 years old will have a mobile phone by 2020. Today, only about 40% [4] of the world’s population use the internet. With more users and different connected devices, eventually data traffic is poised to grow exponentially, as shown in Fig. 1.1, as per Ericsson [5].

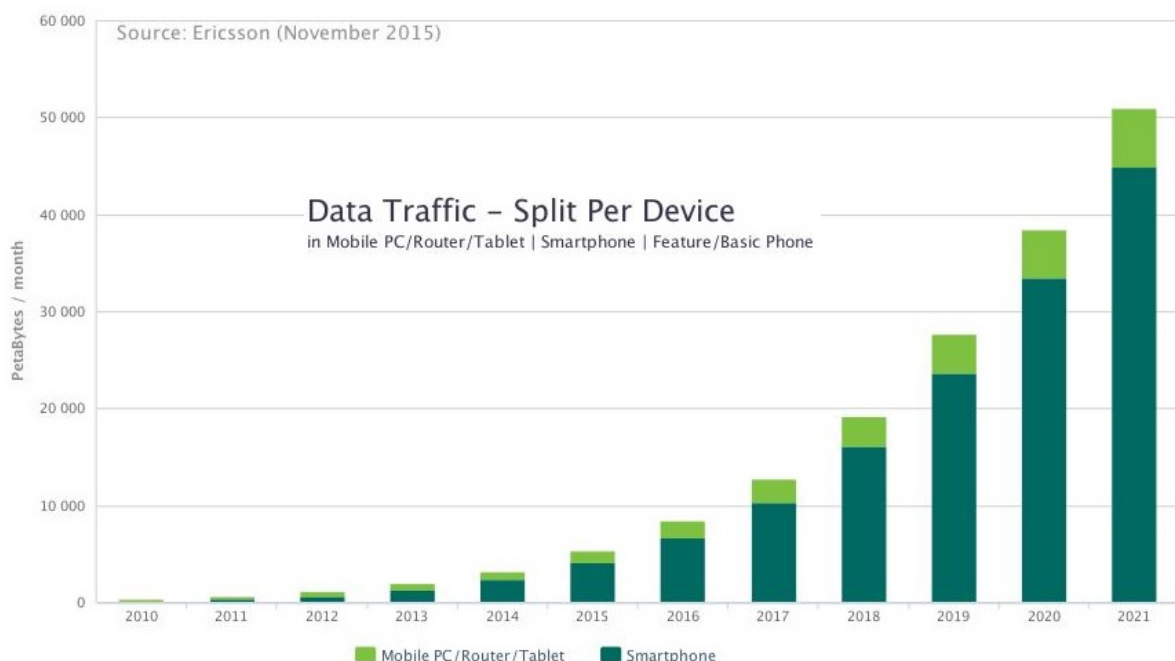


Figure 1.1: Data traffic growth forecast to 2021, as per Ericsson, generated using [5]

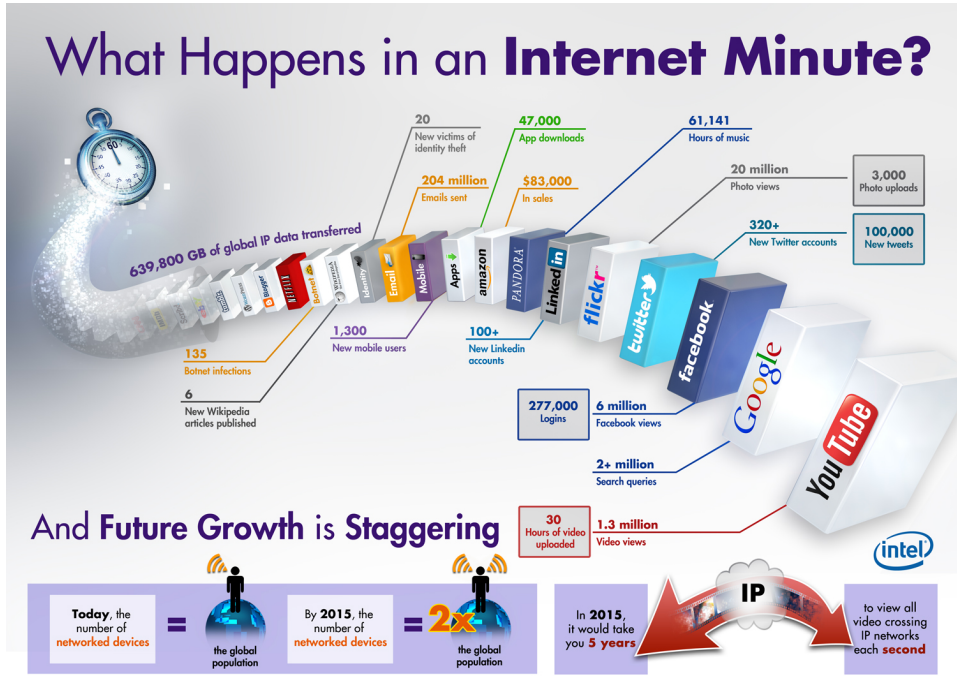


Figure 1.2: What happens on internet per minute [6]

Currently, as illustrated in Fig. 1.2, huge data is processed per minute, due to different Information and Communication Technology (ICT) services. Eventually, as more and more people use these different ICT services on different devices, this data growth will be higher than ever. So how is this data traffic managed currently? The answer is the optical fiber based metro and long haul networks, which forms the backbone of the modern communication systems. Optical fiber is chosen over previously used copper cables for the following reasons:

- **Greater bandwidth:** Fiber provides more bandwidth than copper and can transmit up to 100 Gbps and beyond, with very low power consumption.
- **Reliability and Immunity:** Fiber provides extremely reliable data transmission. It's completely immune to many environmental factors that affect copper cable such as, electromagnetic and radio-frequency interference, crosstalk and impedance problems.
- **Security:** Fiber doesn't radiate signals and is extremely difficult to tap, which provides better security than copper cables.
- **Less attenuation:** Fiber optic transmission results in less attenuation (losses) than copper cables.
- **Lightweight:** Fiber is lightweight, thin, and more durable than copper cable and takes up less space in cable trays.

1.2 Silicon photonics

The performance of optical fiber networks is remarkable and it is this backbone which gives us a great user experience. The current internet architecture has already pushed the optical fiber to the network edges and the trend is to push it as close to the processor as possible. This has already opened up a new trend of “siliconizing photonics” [7], which arose from the research in microelectronics and photonics industry.

The electronics industry has pushed the boundaries of processing power of Integrated Circuit(s) (IC) by adding more transistors, according to Moore’s Law. Until recently, the increase in the speed, efficiency, and processing power of conventional electronic devices were achieved largely through clustering and downscaling of components on a chip. However, this trend toward miniaturization has yielded unwanted effects in the form of significant increases in noise, power consumption, signal propagation delay and aggravates already to serious thermal management problems. As a result, traditional microelectronics will soon fall short of meeting market needs, inhibited by the thermal and bandwidth bottlenecks inherent in copper wiring. Comparison in between Intel’s processor speed and bus speed shows that although we have achieved good processing speed, the interconnects always find difficulty in catching up with the processing speed [8]. Annual global data center IP traffic will reach 10.4 zettabytes (863 exabytes per month) by the end of 2019, up from 3.4 zettabytes per year (287 exabytes per month) in 2014 [9]. Think of a server rack in a data center processing an average of this huge data per second, where interconnects between multiple processors in the server rack add up to a significant bottleneck. These bottlenecks can be overcome by substituting copper with optical interconnects using the current technology, which can also operate at lower power and better efficiency. Additionally, optical interconnects can also improve switching and transmission of electrical signals as well as reduce heat dissipation.

Although silicon is the material of choice for electronics, only from late 1980s silicon has been considered a practical option for Optoelectronic Integrated Circuit(s) (OEIC) solutions. Silicon has many properties that make it a good material for optics. First of all, the band gap of silicon ($\sim 1.1 \text{ eV}$) is such that the material is transparent to wavelengths commonly used for optical communication ($\sim 1.3 \mu\text{m}-1.6 \mu\text{m}$). Moreover, one can use standard Complementary Metal-Oxide Semiconductor (CMOS) processing techniques to sculpt optical waveguides onto the silicon surface. Similar to an optical fiber, these waveguides can be used to confine and direct light as it passes through the silicon [10] using total internal reflection. Due to the wavelengths typically used for optical transport and silicon’s high index of refraction, the sizes needed for these silicon waveguides are on the order of $0.5 \mu\text{m}-1 \mu\text{m}$. This makes silicon excellent for miniaturization of optical components. The fabrication and lithography requirements needed to process waveguides with these sizes exist today. Finally, it is CMOS-compatible, making it possible to process monolithic opto-electronic devices, which could bring higher speed, better functionality, power and size reduction, all at a lower cost.

Today, silicon photonics is a new approach to make miniaturized optical devices that use light to move huge amounts of data at very high speeds with extremely low power over a thin optical fiber rather than using electrical signals over a copper wire. Since

a large capital investment has already been done on perfecting the current fabrication technology and infrastructure, engineers are working on creating monolithic designs of integrated circuits which will use light instead of electrical signals [11]. Research institutes and industry, are trying to bridge this gap by creating highly integrated photonic and electronic components that combine the functionality of conventional CMOS circuits with the significantly enhanced performance of photonic solutions. Various kinds of silicon photonic devices, such as switches [12, 13, 14, 15], modulators [16, 17], photo-detectors [18, 19], delay lines [20, 21], sensors [22, 23, 24] etc. have been reported to date. This leads to a booming silicon photonics market, which is estimated to grow to 700 million USD by 2024 [25, 26] with a Compound Annual Growth Rate (CAGR) of 38%.

1.3 Motivation for MEMS tunable polarization rotator

The dynamic control of optical polarization rotation can be utilized to realize a new class of components in integrated photonics including polarization mode modulators, multiplexers, filters, and switches for advanced optical signal processing, coherent communications, and sensing. Advanced sensors can be designed since more spectrometric analysis can be done using tunable modes. Furthermore, the concept can be useful in situations where polarization tuning is necessary under adiabatic conditions; for example in photon entanglement, which promises the development of even smaller micro-electronic devices along with secure communication channels. Moreover, since the power consumption of the Tunable Polarization Rotator (TPR) is very low, this can be used for reconfiguration of network topology at low power.

Additionally, to keep up with bandwidth requirements using existing network infrastructure, spatial-division multiplexing techniques [27] are being contemplated, which uses multi-mode transmission. However, simply connecting the end of such fibers to an OEIC is far more complicated than standard fibers, because much more mechanical precision is required. Great care has to be taken to make sure light goes in exactly as intended [28]. Moreover, all photonic devices based on silicon waveguides are sensitive to polarization due to large structural birefringence, which induces substantial polarization dependent loss (PDL), polarization mode dispersion (PMD), and other polarization dependent wavelength characteristics ($\text{PD}\lambda$), limiting their usability. Also, in a complex OEIC system, polarization is a major issue because power can be exchanged between the polarization states in the presence of junctions, tapers, slanted sidewalls, bends, or other discontinuities. Therefore, sometimes, it is necessary to control polarization state, and it may also be necessary to rotate an incoming polarization state.

To overcome these challenges, a Polarization Rotator (PR) is engineered in silicon for OEIC, and various passive PR designs have already been demonstrated [29, 30, 31, 32, 33, 34, 35]. However, for dynamic control of optical polarization a TPR is required and some designs [36, 37] have also been demonstrated. The tuning is achieved by thermo-optic effect inducing cross-talk problems, which might change phase of the wave in other waveguides in a high density environment, as silicon is highly susceptible to thermal changes [38]. Hence, the packing density of these TPR using thermo-optic effect

is inefficient. Moreover, the TPR [37] uses out-of-plane ring cavity which inherits the narrow band spectral features of ring resonator thus limiting the bandwidth. Hence, the goal of this thesis is to realize an efficient TPR with high packing density, using Microelectromechanical systems (MEMS) tuning in C and L bands, at low power, without thermo-optic effect.

1.4 Objectives of the thesis

Main objective: To design and fabricate a low power TPR based on MEMS tuning.

Sub objectives: The areas which will be addressed are:

- Evaluate feasibility of MEMS based TPR.
- Design a MEMS TPR capable of tuning polarization in between the two fundamental waveguide modes.
- Demonstration of the MEMS based TPR with an extinction ratio of more than at least 10 dB for the two fundamental modes, in C and L bands.

1.5 Outline of this thesis

The outline of the thesis is as follows: Background, motivation and the research questions being addressed, is discussed in Chapter 1. Background literature of optical waveguide theory is discussed in Chapter 2. In Chapter 3, the current state of art for the available passive and active PR solutions are discussed. Here, also the working principle of the current available designs are explained along with the areas which can be improved. Chapter 4 discusses the design of the final system and the simulation results obtained. In Chapter 5, the fabrication details are provided along with the Scanning electron microscope (SEM) images of the fabricated product. Experiments and results are discussed in Chapter 6. In Chapter 7, the known limitations of the designed TPR are discussed along with future optimizations and work possibilities. Finally, the thesis is concluded with ending remarks in Chapter 8.

2

Chapter 2

Optical waveguide theory

To understand the working principle of PR it is important to look into the basic concepts of waveguides and the mathematics behind the propagation of Electromagnetic (EM) waves. Maxwell combined the electric and magnetic fields in a wave equation for a homogeneous medium. Moreover, to understand PR in waveguides, it also necessary to look into polarization of light and its formal representation using Jones Calculus. Additionally, Poincaré sphere and Stoke's parameter are required for a representation of state of polarization (SOP). Apart from these, different figures of merit (FOM) parameters are used to describe transmission parameters in a waveguide.

2.1 Maxwell's equations

A wave is a disturbance that propagates through a medium. Waves transfer both energy and momentum, without transferring any mass. EM radiation is the radiant energy released by varying EM field in the form of EM waves. A light wave is EM radiation at very high frequency. The frequency of visible light falls in between IR and UV EM waves. James Clerk Maxwell discovered that he could combine four simple equations,

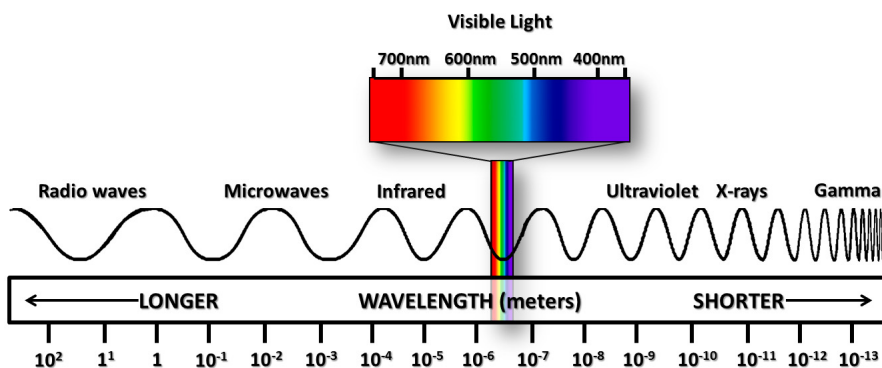


Figure 2.1: The EM wave spectrum

which had been previously discovered, along with a slight modification to describe self-propagating waves of oscillating electric and magnetic fields [39]. The understanding of

propagating light waves using Maxwell's equations in a dielectric medium, is the key to the construction of waveguides. Maxwell's equations relate the electric field E (V/m), magnetic field H (A/m), charge density ρ (C/m³), and current density J (A/cm²).

- **Maxwell's first equation (Gauss' Law):** The net electric flux through any closed surface is equal to $\frac{1}{\epsilon_m}$ times the charge density within that closed surface,

$$\nabla \cdot \mathbf{E} = \frac{\rho}{\epsilon_m}, \quad (2.1)$$

where ϵ_m the permittivity of the medium, and the del operator, ∇ , is given by:

$$\nabla = \left(\frac{\partial i}{\partial x}, \frac{\partial j}{\partial y}, \frac{\partial k}{\partial z} \right) \quad (2.2)$$

where i, j and k are unit vectors in the x, y and z directions respectively.

- **Maxwell's second equation (Gauss' Law for magnetic field):** The net magnetic flux through a closed surface is always zero, since magnetic monopoles do not exist.

$$\nabla \cdot \mathbf{H} = 0 \quad (2.3)$$

- **Maxwell's third equation (Faraday's law):** Induced electric field around a closed path is equal to the negative of the time rate of change of magnetic flux enclosed by the path.

$$\nabla \times \mathbf{E} = -\mu_m \frac{\partial \mathbf{H}}{\partial t} \quad (2.4)$$

where μ_m is the magnetic permeability of the medium.

- **Maxwell's fourth equation (Modification of Ampere's law):** The fourth equation states that magnetic fields can be generated in two ways: by electric current (this was the original "Ampere's law") and by changing electric fields (this was "Maxwell's addition") [40].

$$\nabla \times \mathbf{H} = J + \epsilon_m \frac{\partial \mathbf{E}}{\partial t} \quad (2.5)$$

where ϵ_m is the electric permittivity of the medium.

These equations combine into the following wave equation

$$\nabla^2 \mathbf{E} - \mu_m \epsilon_m \frac{\partial^2 \mathbf{E}}{\partial t^2} = \mu_m \frac{\partial J}{\partial t} + \frac{\nabla \rho}{\epsilon_m}, \quad (2.6)$$

using the curl of curl identity operation given by,

$$\nabla^2 \mathbf{E} = \nabla(\nabla \cdot \mathbf{E}) - \nabla \times (\nabla \times \mathbf{E}). \quad (2.7)$$

A general solution to the equation 2.6 in free space, in absence of charge is,

$$\mathbf{E}(z, t) = E_0(x, y)e^{i(\omega t \pm k_0 z)}, \quad (2.8)$$

where z is direction of propagation of wave in Cartesian coordinates, phase $\phi = \omega t \pm k_0 z$ and wave vector propagation constant, $k_0 = \frac{\partial \phi}{\partial t} = \frac{2\pi}{\lambda}$, in the direction of propagation of the wave. Similar calculations for the magnetic field, \mathbf{H} in free space yields,

$$\mathbf{H}(z, t) = H_0(x, y)e^{i(\omega t \pm k_0 z)} \quad (2.9)$$

2.2 Transverse electromagnetic wave

In the Fig. 2.2 the electric field and magnetic field propagate in directions perpendicular to each other. Moreover, the direction of propagation is also transverse to the EM field. Hence it is called Transverse Electromagnetic (TEM) wave. This is a special case of the wave equation in 2.6.

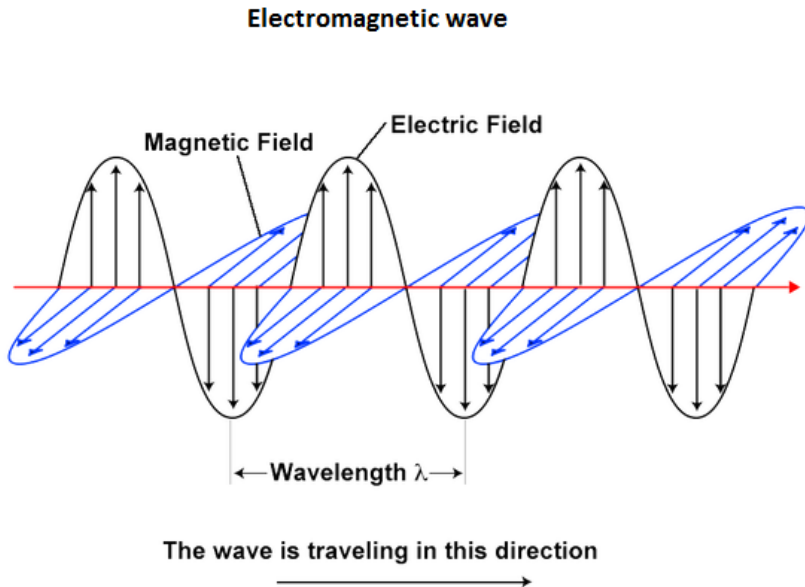


Figure 2.2: Propagation of TEM wave

2.3 Optical waveguides

The waveguide is the essential element of every photonic circuit, and can be characterized by the number of dimensions in which light is confined inside it [41]. A planar waveguide confines light in 1-D, which is simple for understanding of the wave propagation using

Maxwell's equations. However, for practical applications 2-D confinement is necessary and that is why channel waveguides are used. Structures like photonic crystals and waveguide cavities even have 3-D confinement properties. The propagation constant in waveguide varies according to n_{eff} , the effective Refractive index (RI) of the waveguide and is given by

$$k = n_{\text{eff}} k_0, \quad (2.10)$$

where,

$$n_{\text{eff}} = \sqrt{\varepsilon_m \mu_m}. \quad (2.11)$$

2.3.1 Planar waveguides

A simple planar waveguide consists of a high-index medium with height h surrounded by lower-index materials on the top and bottom sides, known as cladding. Planar waveguides are also called slab waveguides. The RI of the film is n_f . The RI of the substrate in lower cladding is n_s whereas, RI of the substrate in upper cladding is n_c .

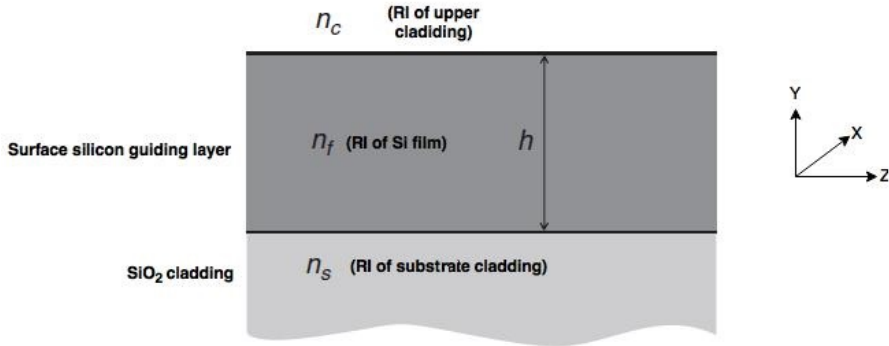


Figure 2.3: A typical planar waveguide where the film is infinite in XZ-plane

For planar waveguides the wave equation for electric field (2.8) and magnetic field (2.9) can be rewritten as follows:

$$\begin{cases} \mathbf{E}(z, t) = E_x(y) e^{i(\omega t \pm k_0 z)} \\ \mathbf{H}(z, t) = H_x(y) e^{i(\omega t \pm k_0 z)} \end{cases} \quad (2.12)$$

since in X-direction the film is infinite. After using the homogeneous wave equations for a planar waveguide the following Transverse Electric (TE) and Transverse Magnetic (TM) mode equations can be deduced:

$$\begin{cases} \nabla^2 E_x(y) + (k_0^2 n(y)^2 - k^2) E_x(y) = 0 \\ \nabla^2 H_x(y) + (k_0^2 n(y)^2 - k^2) H_x(y) = 0 \end{cases} \quad (2.13)$$

where $n(y)$ depends only on a single Cartesian coordinate $n_{\text{eff}} = n(y)$. These equations can be solved analytically using the various boundary conditions of the waveguides which help in deducing the nature of propagation of the wave in TE and TM mode.

2.3.2 Channel waveguides

As mentioned earlier channel waveguides provide confinement in 2-D, which helps in constructing practical waveguides. The three main types of channel waveguides are rib, strip and buried waveguides as depicted in 2.4. While the rib and strip waveguides are fabricated using etching techniques, the buried waveguide mostly relies on diffusion and epitaxial growth techniques for its fabrication.

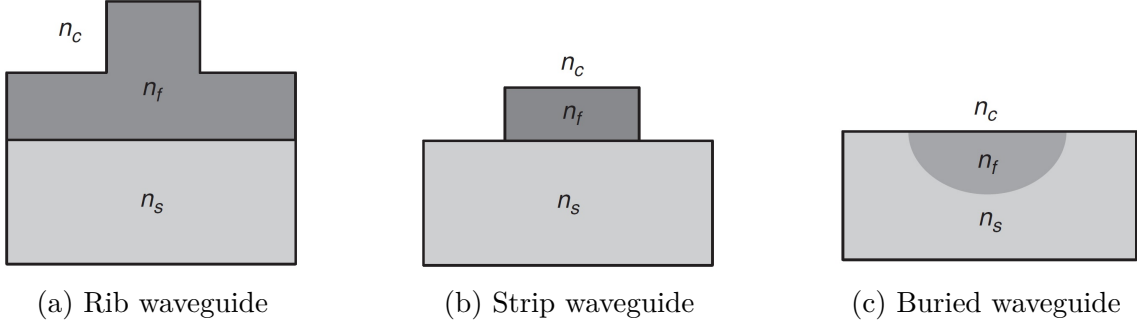


Figure 2.4: Different kinds of design for channel waveguides

Different kinds of numerical methods like Finite element method (FEM), Finite integration technique (FIT), Finite difference time domain (FDTD), Beam propagation method (BPM) have been developed to decipher the nature of light propagation in channel waveguides.

2.4 Eigenvalues and wave modes

In general, the electric field and magnetic field in the wave equation in 2.8 and 2.9 can be written in its constituent parts in Cartesian coordinates as:

$$\begin{cases} \mathbf{E} = E_x i + E_y j + E_z k \\ \mathbf{H} = H_x i + H_y j + H_z k \end{cases} \quad (2.14)$$

The generalized vectorial component of the electric and magnetic field of equation 2.13 for a traveling wave in Z direction can be combined into the Helmholtz equation as follows:

$$\nabla^2 \Psi(x, y, z) + k_0^2 n^2(x, y) \Psi(x, y, z) = 0 \quad (2.15)$$

where, $\Psi(x, y, z) = \psi(x, y) e^{-jkz}$ and then the equation 2.15 can be rewritten as,

$$\nabla_{xy}^2 \psi(x, y) + (k_0^2 n^2(x, y) - k^2) \psi(x, y) = 0. \quad (2.16)$$

The equation 2.16 can be solved for $\psi(x, y)$, using different numerical methods like FEM, FIT, BPM, FDTD. The numerical methods first decompose the waveguide into sufficient number small cells (more cells give more robust solution at the cost of increased

computing turns) and then discretization of the refractive index profile is performed. Next the field equations are discretized by replacing the derivatives by their finite difference representations in those cells. In this way a set of linear equations are obtained which can be solved using standard algebraic methods. In general, FIT has a much lower memory footprint.

For given ω , the resulting mode problem is an eigenproblem, solved for eigenvectors, i.e., mode profiles $\psi(x, y)$, and eigenvalues, from which the corresponding propagation constants k of the modes are computed. The geometry of the waveguide is given by the transverse dependence of ϵ , with effective RI profile, and by appropriately chosen boundary conditions. Each allowed solution is referred to as the **mode of propagation**. For example, when light travels through a rectangular waveguide different modes can be visualized as follows in Fig. 2.5.

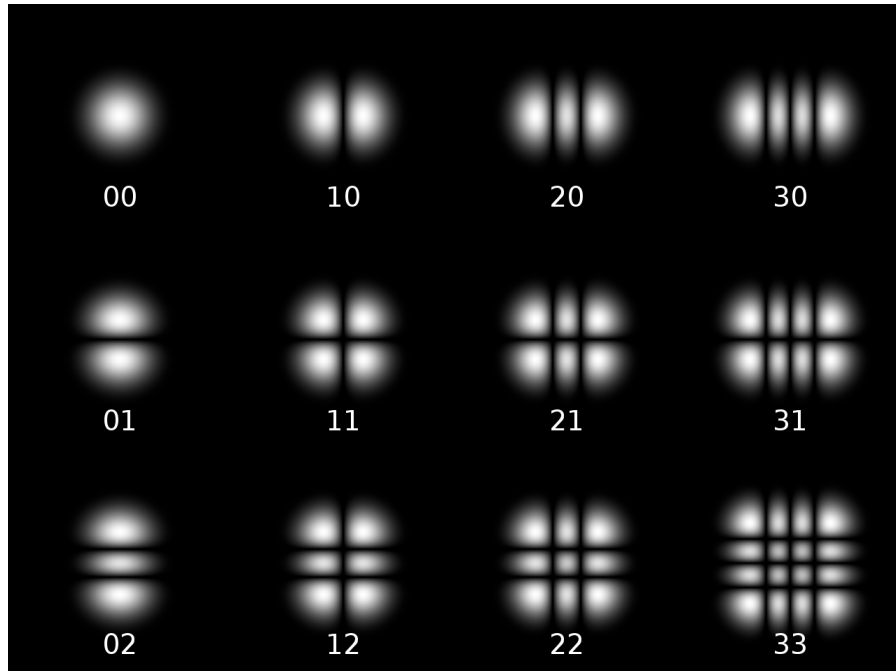
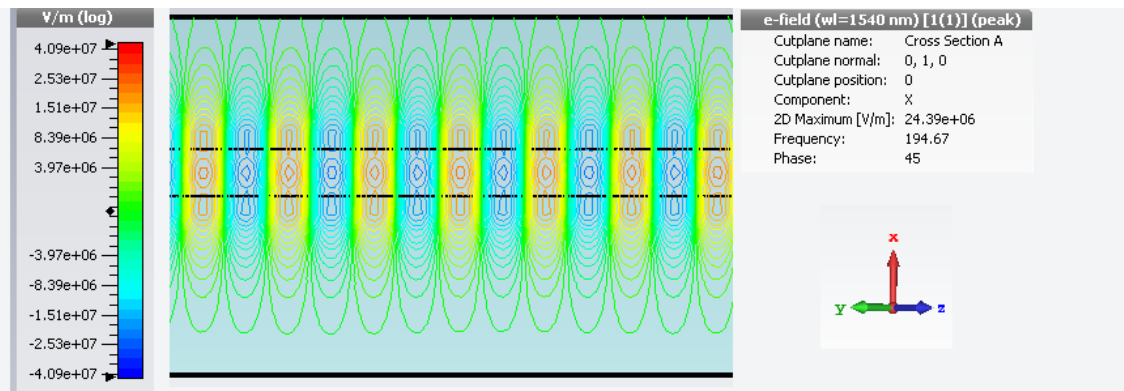


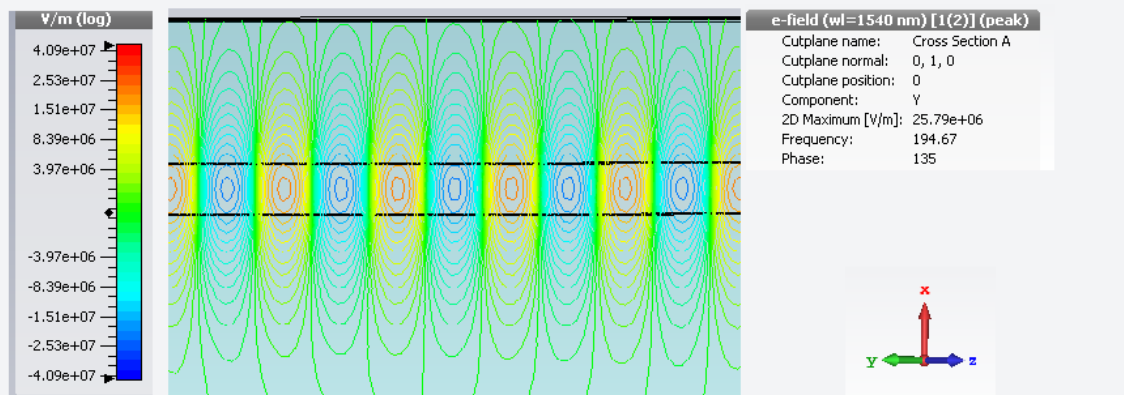
Figure 2.5: TEM modes labelled with corresponding indices. The indices describe the shape of the modes as $m+1$ columns and $n+1$ rows. i.e. TEM_{21} mode shape has 3 columns and 2 rows.

2.5 Polarization

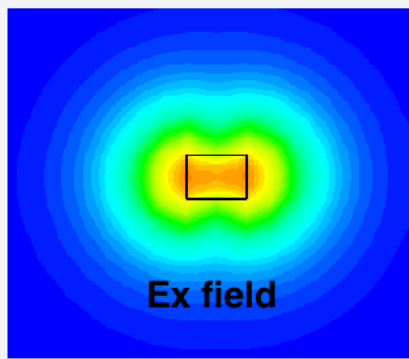
Polarization is a wave mode solution which fits in the waveguide and is represented by the direction of the electric field associated with the propagating wave. In the example in Fig. 2.2 the wave is linearly polarized since the electric field and magnetic field exist in one direction only. In a dielectric optical waveguide, light propagates in linearly polarized modes and the plane in which light is polarized is either vertical or horizontal to the direction of wave, as shown in Fig. 2.6 in single-mode.



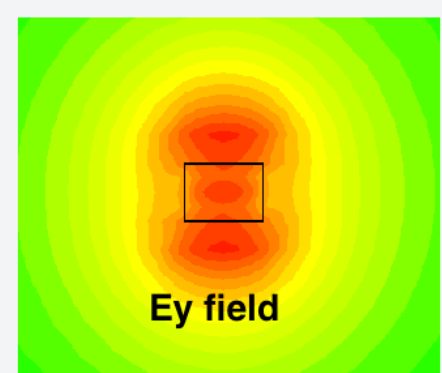
TE fundamental mode viewed from top on Y-cutplane



TM fundamental mode viewed from top on Y-cutplane



TE fundamental mode viewed on Z-cutplane



TM fundamental mode viewed on Z-cutplane

Figure 2.6: TE and TM fundamental mode in a waveguide using CST simulation

2.5.1 TE mode

TE mode is the fundamental mode in which there is no electric field in the direction of propagation of light wave. In Fig. 2.6 the electric field lines (blue) are perpendicular to the plane of incidence in TE mode. The plane of incidence is the plane in which optical waves strike the surface of the waveguide.

2.5.2 TM mode

TM mode is the fundamental mode in which there is no magnetic field in the direction of propagation of light. In Fig. 2.6 it can be seen that magnetic field (red lines) are perpendicular to the plane of incidence in TM mode.

2.5.3 Quasi-TE and Quasi-TM mode

Practically, waveguide cores have electric and magnetic fields that slice through air and the cladding substrate. Hence they do not support pure TE and TM modes. However, since most the power is contained under the waveguide core and inside just the cladding, TE and TM modes can be a good approximation. Generally, in these modes there is some field component in the direction of propagation as well. This is known as quasi-TE and quasi-TM mode.

2.6 Jones calculus

Polarized light can be represented using Jones calculus. Polarized light is represented using a *Jones vector* and linear optical elements are represented by *Jones matrices*. When light crosses an optical element the resulting polarization of the emerging light is found by taking the product of the Jones matrix of the optical element and the Jones vector of the incident light. *Jones calculus* is only applicable to light that is fully polarized [42].

2.6.1 Jones vector

The Jones vector describes the SOP of light in free space or another homogeneous isotropic non-attenuating medium, where the light can be properly described as transverse waves [42]. The Jones vector is a complex vector that is a mathematical representation of a real wave. A typical representation of the electric field for the optical wave described in 2.8 can be as follows:

$$\mathbf{E} = \begin{pmatrix} E_x(t) \\ E_y(t) \\ 0 \end{pmatrix} = \begin{pmatrix} E_x e^{i(\omega t - kz + \phi_x)} \\ E_y e^{i(\omega t - kz + \phi_y)} \\ 0 \end{pmatrix} = \begin{pmatrix} E_x e^{i\phi_x} \\ E_y e^{i\phi_y} \\ 0 \end{pmatrix} e^{i(\omega t - kz)} \quad (2.17)$$

where ϕ_x and ϕ_y represent the phase of E_x and E_y fields. The Jones vector of the plane wave is described by:

$$\begin{pmatrix} E_x e^{i\phi_x} \\ E_y e^{i\phi_y} \end{pmatrix} \quad (2.18)$$

and the intensity of the optical wave, I wave can be written as,

$$I = |E_x|^2 + |E_y|^2 \quad (2.19)$$

Generally, a wave of unit intensity is used for the consideration polarization. So Jones vector is noted using an unit vector as,

$$\mathbf{E}\bar{\mathbf{E}} = 1, \quad (2.20)$$

where \bar{E} is the complex conjugate of E . In general the Jones representation of a normalized elliptically polarized beam with azimuth θ and elliptical angle ϵ is given by,

$$e^{i\phi} \begin{pmatrix} \cos \theta \cos \epsilon - j \sin \theta \sin \epsilon \\ \sin \theta \cos \epsilon - j \cos \theta \sin \epsilon \end{pmatrix} \quad (2.21)$$

where $e^{i\phi}$ is an arbitrary phase vector and $\phi = \phi_x - \phi_y$. So, for example a linear polarization of TE mode can be represented as,

$$\begin{pmatrix} 1 \\ 0 \end{pmatrix} \quad (2.22)$$

since, $\theta = 0$ and $\epsilon = 0$.

2.6.2 Jones matrix

Jones matrix is the formal representation of the various optical elements such as lenses, beam splitters, mirrors, phase retarders, polarizers at arbitrary angles that can modify polarization. They generally operate on Jones vectors and helps in comprehending situations which light encounters multiple polarization elements in sequence. In these situations the products of the Jones matrices can be used to represent the transfer matrix. This situation can be represented using,

$$[E_{output}] = J_{system}[E_{input}] \quad (2.23)$$

where E_{input} is the input field into the optical system and E_{output} is the generated output field represented using Jones vector. The matrix J_{system} is the Jones matrix of the optical system comprising of a series of polarization devices. If there are N devices in the system then the final transfer matrix comes out as,

$$J_{system} = J_N J_{N-1} \dots J_2 J_1 \quad (2.24)$$

where J_N is the Jones matrix for n^{th} polarizing optical element.

2.6.3 Jones matrix for polarizing optical systems

Polarizer and wave plates are fundamental components which is required in an optical test-bench. These are discussed using Jones Calculus in the following sections.

2.6.3.1 Polarizer

Polarizers have an index of refraction which depends on orientation electric field propagation. If any optical system has a transmission axis and an absorption axis for electric fields, then lights will be passed along the transmission axis and absorbed along the other axis. So, the Jones matrix of a polarizer making an angle θ with the X-axis will come out as,

$$\begin{pmatrix} \cos^2 \theta & \sin \theta \cos \theta \\ \sin \theta \cos \theta & \sin^2 \theta \end{pmatrix} \quad (2.25)$$

2.6.3.2 Wave plates

Wave plates are phase retarders which are made of birefringent crystals. Wave plates can be conceptualized as two polarizers kept apart at certain distance d , such that their polarization axes are apart orthogonally (90°). The phase difference as light passes through this setup of thickness d is [43],

$$(k_{slow} - k_{fast}) d = \frac{2\pi d}{\lambda_{vac}} (n_{slow} - n_{fast}) \quad (2.26)$$

In, general the Jones matrix for a wave plate is given by [43],

$$\begin{pmatrix} \cos^2 \theta + \xi \sin^2 \theta & \sin \theta \cos \theta - \xi \sin \theta \cos \theta \\ \sin \theta \cos \theta - \xi \sin \theta \cos \theta & \sin^2 \theta + \xi \cos^2 \theta \end{pmatrix} \quad (2.27)$$

where ξ is calculated based on the type of wave plate. The following equations addresses some specific scenarios:

$$\begin{cases} \xi = e^{i\pi/2}, & \text{where, } (k_{slow} - k_{fast}) d = \pi/2 + 2\pi m, \text{ for quarter-wave plate} \\ \xi = e^{i\pi}, & \text{where, } (k_{slow} - k_{fast}) d = \pi + 2\pi m, \text{ for half-wave plate} \end{cases} \quad (2.28)$$

and $m \in \mathbb{Z}$. ξ is the phase delay of the wave plates. Similar concept is used in the construction of PR waveguides which will be discussed in later sections shortly.

2.7 Poincaré sphere and state of polarization

To view a complete representation of all the polarization ellipses generated using Jones vectors, a spherical structure with unit radius is used, which is known as Poincaré sphere. If the orientation in space of the ellipse of polarization is determined by the azimuth, θ and ellipticity, ϵ then that point can be completely characterized by its longitude 2θ and latitude 2ϵ . The north and south poles represent the right-handed and left-handed circular polarization respectively. In general the diametrically opposite points represent pairs of orthogonal polarization. The SOP and its corresponding location in the Poincaré sphere is visualized in the Fig. 2.7. To go from one SOP to another the polarized light can be passed through various optical components which can be computed using the Jones matrix and the corresponding SOP can be represented on the Poincaré sphere.

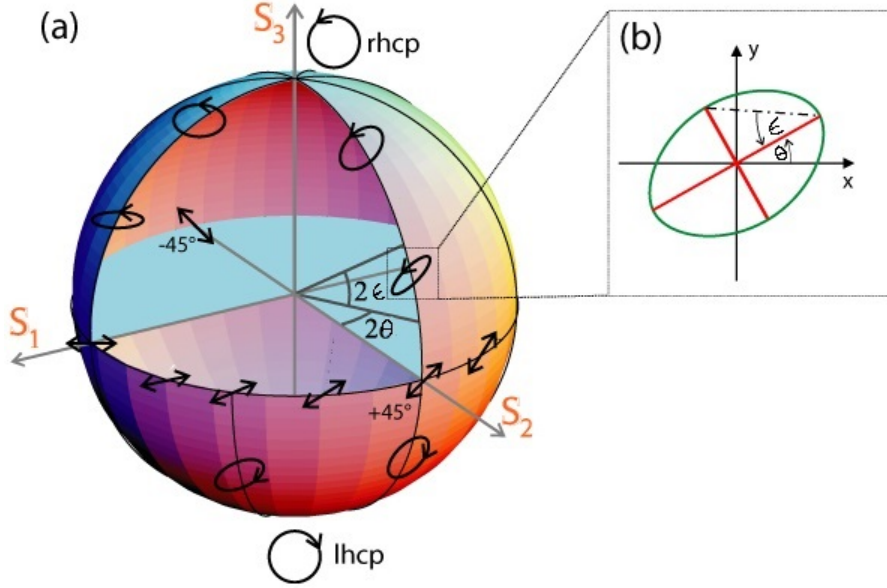


Figure 2.7: (a) Representation of the Poincaré sphere (b) Representation of the ellipse parameters [44]

For complete polarized light, the point on the Poincaré sphere must be fixed on time which requires,

$$\frac{E_x(t)}{E_y(t)} = \text{constant} \quad (2.29)$$

and,

$$\phi = \phi_x(t) - \phi_y(t) = \text{constant} \quad (2.30)$$

2.8 Stoke's parameter

Quasi-monochromatic waves are mathematically treated using Stokes parameters (S_0, S_1, S_2, S_3), which constitute a vector generally known as Stokes vectors. Stokes vectors are used to keep track of the partial polarization (and attenuation) of a light beam in terms of total intensity (I), degree of polarization (p) and ellipse parameters, as the light progresses through an optical system. A Stokes vector can generally be represented as,

$$\vec{S} = \begin{pmatrix} S_0 \\ S_1 \\ S_2 \\ S_3 \end{pmatrix} \quad (2.31)$$

where,

$$\begin{cases} S_0 = I \\ S_1 = I_p \cos 2\theta \cos 2\epsilon \\ S_2 = I_p \sin 2\theta \cos 2\epsilon \\ S_3 = I_p \sin 2\epsilon \end{cases} \quad (2.32)$$

Here, I_p , 2θ , 2ϵ are the spherical coordinates of the 3-D vector of Cartesian coordinates (S_1, S_2, S_3) . So, given the Stokes parameters, the spherical coordinates $(p, 2\theta, 2\epsilon)$ can be obtained and represented by a point inside the Poincaré sphere using the following:

$$\begin{cases} I = S_0 \\ p = \frac{\sqrt{S_1^2 + S_2^2 + S_3^2}}{S_0} \\ 2\theta = \tan^{-1} \frac{S_2}{S_1} \\ 2\epsilon = \tan^{-1} \frac{S_3}{\sqrt{S_1^2 + S_2^2}} \end{cases} \quad (2.33)$$

The prescribed notations are portrayed on the Poincaré sphere in the following Fig. 2.8.

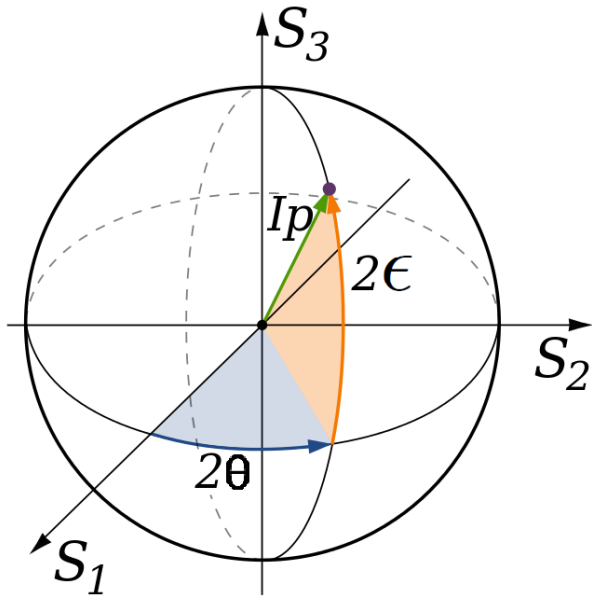


Figure 2.8: Poincaré sphere, on or beneath which the three Stokes parameters $[S_1, S_2, S_3]$ are plotted in Cartesian coordinates [45]

2.9 Coupled mode theory

In a waveguide, an ideal mode is an eigenvector of a propagation constant. Mode coupling enables transfer of energy from one ideal mode to another, during propagation. Mode coupling can be induced by introducing another independent waveguide structure in close proximity (coupled waveguides in close proximity are modeled as a single structure, forming supermodes). The pairwise coupling strength between two modes depends on a dimensionless ratio between the coupling coefficient (per unit length) and the difference between the two modal propagation constants. Hence, a given perturbation may strongly couple modes having nearly equal propagation constants, but weakly couple modes having

highly unequal propagation constants. PMD and PDL have long been described by field coupling models, in which phase dependent coupling of modal fields is described by complex coefficients. Field coupling models describe not only a redistribution of energy among modes, but also how eigenvectors and their eigenvalues depend on the mode coupling coefficients [46].

Perturbation Analysis: Supermodes can be represented as weighted sum of individual guided modes. If two modes are represented by $\psi_1(x, y)$ and $\psi_2(x, y)$ in the different waveguides along with the coupling between two modes as $X_i(z)$, then the supermode can be written using Helmholtz identity as,

$$\Psi(x, y, z) = X_1(z)\psi_1(x, y) + X_2(z)\psi_2(x, y) \quad (2.34)$$

The uncoupled modes, ψ_1 and ψ_2 satisfy the following propagation equations with propagation constants k_1 and k_2 ,

$$\begin{cases} \frac{dX_1}{dz} = -jk_1X_1 \\ \frac{dX_2}{dz} = -jk_2X_2 \end{cases} \quad (2.35)$$

A known solution for 2.35 is:

$$\begin{cases} X_1(z) = e^{-jk_1z} \\ X_2(z) = e^{-jk_2z} \end{cases} \quad (2.36)$$

Coupled mode theory postulates that to describe a perturbed system the linear coupling terms need to be added as,

$$\begin{cases} \frac{dX_1}{dz} = -jk_1X_1(z) - j(\kappa_{11}X_1 + \kappa_{12}X_2) \\ \frac{dX_2}{dz} = -jk_2X_2(z) - j(\kappa_{21}X_1 + \kappa_{22}X_2) \end{cases} \quad (2.37)$$

where, κ_{ij} , $\forall (i, j) \in [1, 2]$ are the linear coefficients which can be understood using the scattering matrix as,

$$\begin{pmatrix} \kappa_{11} & \kappa_{12} \\ \kappa_{21} & \kappa_{22} \end{pmatrix} \quad (2.38)$$

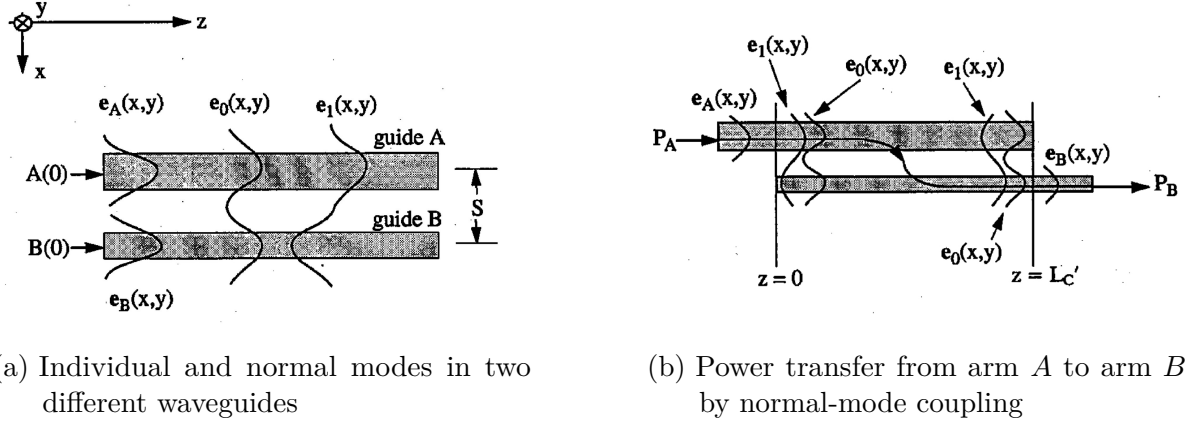
where,

$$\begin{cases} \kappa_{11} = \frac{1}{2}k_0^2 \int \int (n_{12}^2 - n_1^2)\psi_1^2 dx dy \\ \kappa_{12} = \frac{1}{2}k_0^2 \int \int (n_{12}^2 - n_1^2)\psi_1\psi_2 dx dy \\ \kappa_{21} = \frac{1}{2}k_0^2 \int \int (n_{12}^2 - n_2^2)\psi_1\psi_2 dx dy \\ \kappa_{22} = \frac{1}{2}k_0^2 \int \int (n_{12}^2 - n_2^2)\psi_2^2 dx dy \end{cases} \quad (2.39)$$

Here, κ_{11} and κ_{22} are the reflection coefficients and κ_{12} and κ_{21} are the coupling coefficients. Normally, it is assumed that the modes are normalized, and propagate in a lossless system with symmetric coupling coefficients. Hence,

$$\kappa_{12} = \kappa_{21} \quad (2.40)$$

Coupling coefficients and phase mismatch are important factors for power exchange between different modes. In 2.9a both the waveguides are excited where as in 2.9b only waveguide B is excited.



(a) Individual and normal modes in two different waveguides

(b) Power transfer from arm A to arm B by normal-mode coupling

Figure 2.9: Description of the directional coupler under coupled-mode and normal-mode

In 2.9b for no phase mismatch complete power exchange occurs. This is why phase matching is an important criteria for mode coupling. The coupling length is, $L_c = \pi/2\kappa$.

Coupling mode theory has been successfully applied to the modeling and analysis of various guided-wave optoelectronic devices, such as optical directional couplers made of thin film and channel waveguides, multiple waveguide lenses, phase-locked laser arrays, distributed feedback lasers and distributed Bragg reflectors, grating waveguides and couplers, nonparallel and tapered waveguide structures, Y-branch waveguides, TE/TM polarization converters, mode conversion and radiation loss in slab waveguides, residual coupling among scalar modes. It has also been used to study the wave coupling phenomena in nonlinear media such as harmonic generation in bulk and guided-wave devices, and nonlinear coherent couplers [47].

2.10 Figures of merit

The FOM represents the benchmarks present for comparing different optical waveguide components.

2.10.1 Confinement factor

The confinement factor is a measure of the proportion of the electric field power in a given mode that lies within the core.

$$\text{Confinement factor} = \frac{\int_{-w/2}^{w/2} E_x^2(y) dy}{\int_{-\infty}^{\infty} E_x^2(y) dy}, \quad (2.41)$$

where, w is the width of the waveguide core. Confinement factor is an important measure which is function of various factors like polarization, RI difference between the core and cladding, mode number etc.

2.10.2 Polarization extinction ratio

The Polarization extinction ratio (PER) is the ratio of optical powers of TE and TM polarizations. The PER is used to characterize the degree of polarization in a polarization maintaining device or fiber.

$$\begin{cases} PER_{TE-TM} = 10 \log_{10} \frac{P_{TM}}{P_{TE}} \\ PER_{TM-TE} = 10 \log_{10} \frac{P_{TE}}{P_{TM}} \end{cases} \quad (2.42)$$

2.10.3 Insertion loss

Insertion loss is the loss of signal power resulting from the insertion of a device in a transmission line or optical fiber and is usually expressed in decibels (dB). If the power transmitted to the load before insertion is P_{in} and the power received by the load after insertion is P_{out} , then the Insertion loss (IL) in dB is given by,

$$IL = 10 \log_{10} \frac{P_{in}}{P_{out}} \quad (2.43)$$

3 State of the art

Chapter 3

To develop a MEMS TPR for optical waveguides, the integrated passive and active PRs found in the recent literature and their underlying concepts are discussed in this chapter.

3.1 Polarization rotator (PR)

PRs help in rotating linearly polarized fields from one SOP to another in a controlled manner. Currently, both optical fiber and on-chip based PRs are available.

3.2 Optical fiber PR

In an ordinary (non-polarization-maintaining) fiber, TE and TM have the same nominal phase velocity due to the fiber's circular symmetry. However tiny amounts of random birefringence in such a fiber, or bending in the fiber, will cause a tiny amount of crosstalk from the TM to TE mode. And since even a short portion of fiber, over which a tiny coupling coefficient may apply, is many thousands of wavelengths long, even that small coupling between the two polarization modes, applied coherently, can lead to a large power transfer to the TE mode, completely changing the wave's net state of polarization. Since that coupling coefficient was unintended and a result of arbitrary stress or bending applied to fiber, the output state of polarization will itself be random, and will vary as those stresses or bends vary; it will also vary with wavelength.

Polarization-maintaining fibers work by intentionally introducing a systematic linear birefringence in the fiber, so that there are two well defined polarization modes which propagate along the fiber with very distinct phase velocities. The beat length L_b of such a fiber (for a particular wavelength) is the distance (typically a few millimeters) over which the wave in one mode will experience an additional delay of one wavelength compared to the other polarization mode. Thus a length $\frac{L_b}{2}$ of such fiber is equivalent to a half-wave plate. Now consider that there might be a random coupling between the two polarization states over a significant length of such fiber. At point 0 along the fiber, the wave in polarization mode 1 induces an amplitude into mode 2 at some phase. However at point $\frac{L_b}{2}$ along the fiber, the same coupling coefficient between the polarization modes

induces an amplitude into mode 2 which is now 180° out of phase with the wave coupled at point zero, leading to cancellation. At point L_b along the fiber the coupling is again in the original phase, but at $\frac{3L_b}{2}$ it is again out of phase and so on. The possibility of coherent addition of wave amplitudes through crosstalk over distances much larger than L_b is thus eliminated. Most of the wave's power remains in the original polarization mode, and exits the fiber in that mode's polarization as it is oriented at the fiber end [48].

Electrically driven polarization controller currently available provides a simple, efficient means to manipulate the state of polarization within a singlemode fiber. These operate with negligible insertion and return losses at 100Hz response speed with continuous polarization control capability at low voltage [49].

3.3 On-chip PR

The currently available OEIC PRs can be classified under two categories as passive and active PR. In the passive PRs the waveguide structures are designed in a specific way to manipulate the effective RI of the waveguide, in order to obtain the desired polarization. The RI cannot be manipulated or tuned once fabricated. Whereas, in active PRs, the effective RI can be manipulated by thermo-optic or quantum effects.

3.3.1 Passive PR

The fields in TE and TM mode are orthogonal (i.e. no coupling exists) and are of different geometry. Thus asymmetric structure in both horizontal and vertical directions are required to break the symmetry, which is accomplished by using different principles viz. mode coupling [33, 50, 32], mode evolution [51, 35, 52, 53, 54] and mode hybridization [55, 31, 56, 30], described in the following sections. All these principles are based on the coupling mode theory described in 2.9.

3.3.1.1 Mode coupling

Mode coupling PR includes a pair of waveguides running parallel to each other, with coupled evanescent fields within close proximity. When two modes with orthogonal polarizations have equal effective RIs, strong mode coupling occurs in between the waveguides (generally asymmetric directional couplers), and with proper taper orientation and design, length of coupling region, one mode can be effectively converted to the other.

- Design: Ultra-compact polarization splitter-rotator based on silicon nanowires

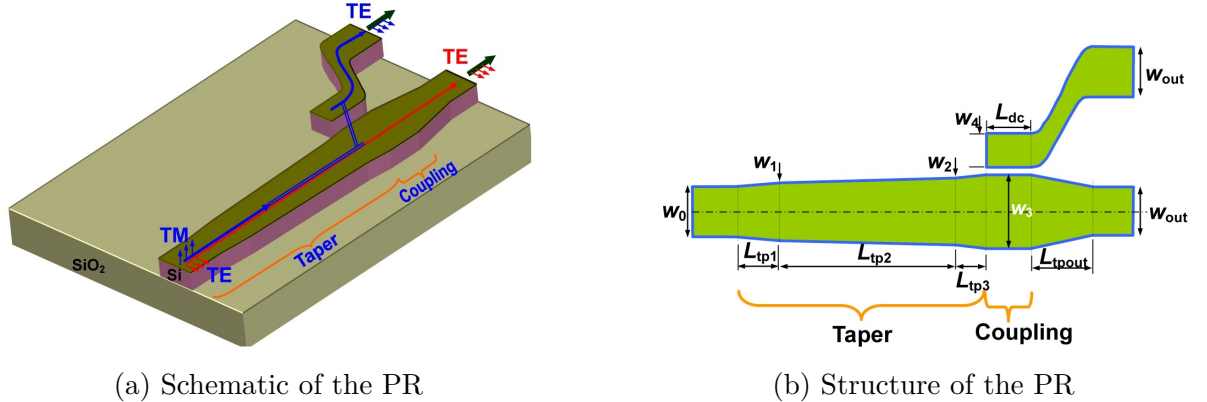


Figure 3.1: PR using mode coupling, by Dai and Bowers [33]

The coupler (Fig. 3.1a) consists of 2 waveguides parallel to each other. The section where coupling occurs is shown in Fig. 3.1b. The taper structure is singlemode at the input end (W_0) while it becomes multimode at the other end (W_3). When light propagates along the taper structure, the TM fundamental mode launched at the narrow end (W_0) is converted to the first higher-order TE mode at the wide end (w_3) because of the mode coupling between them. Another narrow optical waveguide (W_4) is then placed close to the wide waveguide (W_3) and an asymmetrical directional coupler is formed. By using this asymmetrical directional coupler, the first higher-order TE mode in the wide waveguide is then coupled to the TE fundamental mode of the adjacent narrow waveguide. In this way, the input TM fundamental mode at the input waveguide is finally converted into the TE fundamental mode at the cross port of asymmetrical directional coupler. On the other hand, the input TE polarization keeps the same polarization state when it goes through the adiabatic taper structure. In the region of the asymmetrical directional coupler, the TE fundamental mode in the wide waveguide could not be coupled to the adjacent narrow waveguide because of the phase mismatching. In this way, TE- and TM- polarized light are separated while the TM fundamental mode is also converted into TE fundamental mode [33].

Various other designs for mode coupling have also been proposed [32, 50], which work on the same principle.

- **Problem of mode coupling:** The main problem of mode coupling is that directional couplers are not very broadband. Moreover, due to the large birefringence of silicon waveguides, the conversion usually occurs between fundamental TM and high order TE modes and subsequently the high order TE mode is converted to the fundamental TE mode.

3.3.1.2 Mode evolution

The mode evolution based PR includes a single waveguide core. The waveguide is designed in such a way that the cross-section of the waveguide varies along the direction of propagation, both in width and height. This changes polarization from TE to TM or vice versa gradually in propagation direction, under adiabatic transition conditions. Since, the cross-section changes gradually and not abruptly, the PER is high in these type of PRs.

□ Design A: Mode evolution PR based on single taper

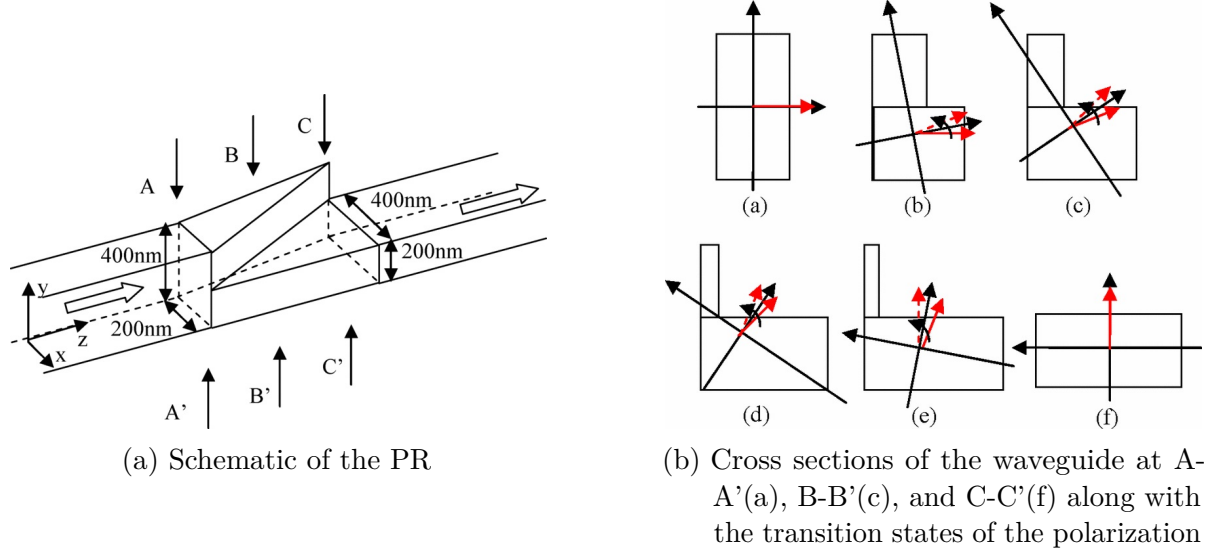


Figure 3.2: PR using mode evolution, by Zhang *et al.* [51]

The PR (Fig. 3.2a) consists of the variable cross section for polarization rotation. The transition region of the rotator was divided into N sections. Each section was considered as a uniform asymmetrical waveguide like the rotator in [57]. The length of each section was its half-beat length. The half-beat length of the n^{th} section is $L_\pi^n = (\pi / (\beta_1^n - \beta_2^n))$, where $\beta^n = (2\pi/\lambda) n_{eff}^n$ and β_1^n and β_2^n are the propagation constants of the two fundamental modes in the n^{th} section. After propagating in the n^{th} section, the polarization will rotate $2\Delta\varphi_n$ toward the optical axis, where φ_n is the angle between the optical axis and the polarization of the incident light. The overall rotator should satisfy $\sum_n 2\Delta\varphi_n = 90^\circ$, to achieve a rotation of 90° in the cascaded sections. Fig. 3.2b shows the rotation procedure [51].

- Design B: Mode evolution PR composed of an asymmetric-rib waveguide and a tapered waveguide

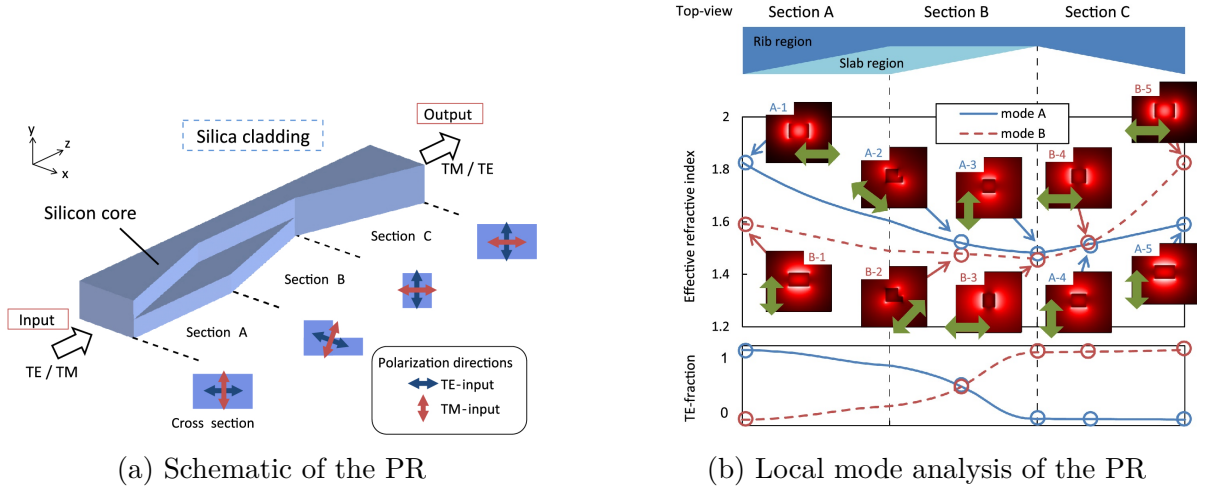


Figure 3.3: PR using mode evolution, by Goi *et al.* [54]

The PR (Fig. 3.3a) consists of the polarization rotation sections(A and B) with an asymmetric rib waveguide and the mode size conversion section(C) with a nano-tapered waveguide. This design provides both vertical and horizontal asymmetry.

Apart from these, other designs for mode evolution have also been proposed [35, 52, 53], which has the same basic principle.

- **Problem of mode evolution:** In mode evolution, silicon waveguide is specially designed with tapers to enable gradual mode conversion between orthogonal polarization states. This kind of design increases the complexity of fabrication. Also, sharp tips at the end of tapers necessary for low conversion loss are also difficult to make. A pure silicon solution is proposed in [51], but in their structure the input and output silicon waveguides have different thicknesses. The structure in [54] solves this problem at the cost of a longer device length of 230 μm . Efficient design of these kind of PRs require trade-off between scattering losses at the tapers versus the device length.

3.3.1.3 Mode hybridization

Mode hybridization works by abruptly breaking the symmetry of the silicon waveguide cross section. The propagation modes are hybridized due to introduced asymmetry, allowing optical power to be transferred periodically between the two desired polarization states. The propagation modes excite simultaneously the two fundamental hybrid modes of the asymmetric waveguide, which evolve with different propagation constant. The rotation of 90° is achieved through interference of the two hybridized modes for a length of L_π , according to the principle of wave plates described mathematically, using 2.28.

□ **Design A: Asymmetric silicon nanowire waveguide as compact PR**

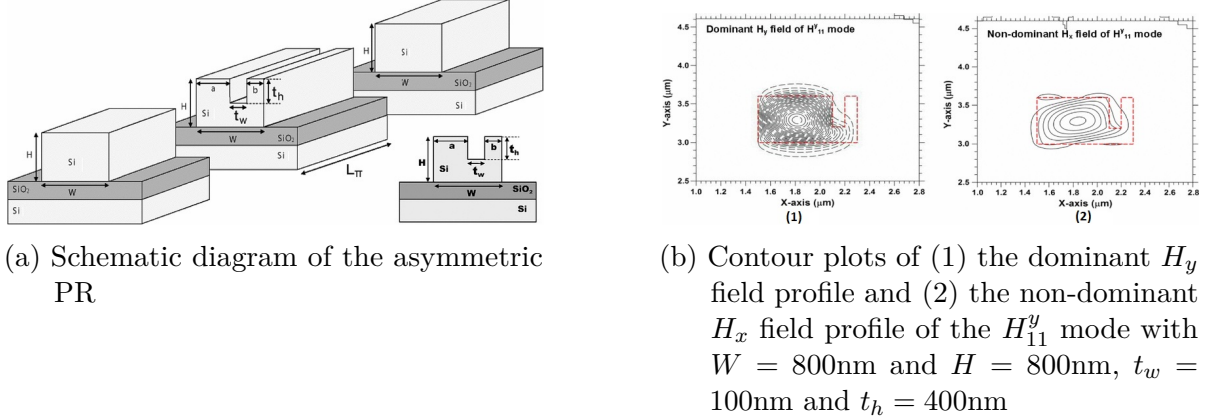


Figure 3.4: PR using mode hybridization, by Leung *et al.* [31]

Fig. 3.4a depicts the single-stage polarization rotator, which consists of two Si strip waveguides with straight sidewalls, where both are butt coupled to an Si asymmetric strip polarization rotator waveguide in the middle. In the design of a polarization rotator, an asymmetric section which supports the highly hybrid modes is sandwiched between two standard Si waveguides. When a quasi-TE (or quasi-TM) mode from a standard Si waveguide with its polarization angle at nearly zero degrees (or 90°) is launched into the asymmetric section (which supports highly hybrid modes with polarization direction $\pm 45^\circ$), then both of them are excited almost equally to satisfy the continuity of the E_t and H_t fields at that interface. These two highly hybrid modes travel along the asymmetric sections. The half-beat length is a key parameter used in order to identify the optimum length of this asymmetrical section to achieve the maximum polarization rotation. The half-beat length is defined as $L_\pi = \pi/\Delta\beta$, where $\Delta\beta$ is the difference between the propagation constants of the two hybrid modes. After propagating a distance $L = L_\pi$, the original phase condition between the highly polarized modes would be reversed, and the polarization state of the superimposed modes would be rotated by 90° . If a standard Si waveguide (with smaller modal hybridness) is placed at this position, this quasi-TM (or quasi-TE) mode would propagate without any further polarization rotation [31].

□ **Design B: Efficient silicon PR based on mode-hybridization in a double-stair waveguide**

Due to the sudden abruptness introduced in the previous design (Design A) of mode hybridization, the PER was low. Hence, the abruptness is introduced more gradually in the design, as shown in Fig. 3.5b. The design looks like two successive stairs and hence it is called double-stair waveguide. The PR [29], based on a double-stair silicon waveguide fabricated with three etch steps as described in Fig.3.5a is better compared to the two-etch-step structure with single-stair cross section [58] because of the higher PER and broader optical bandwidth achieved.

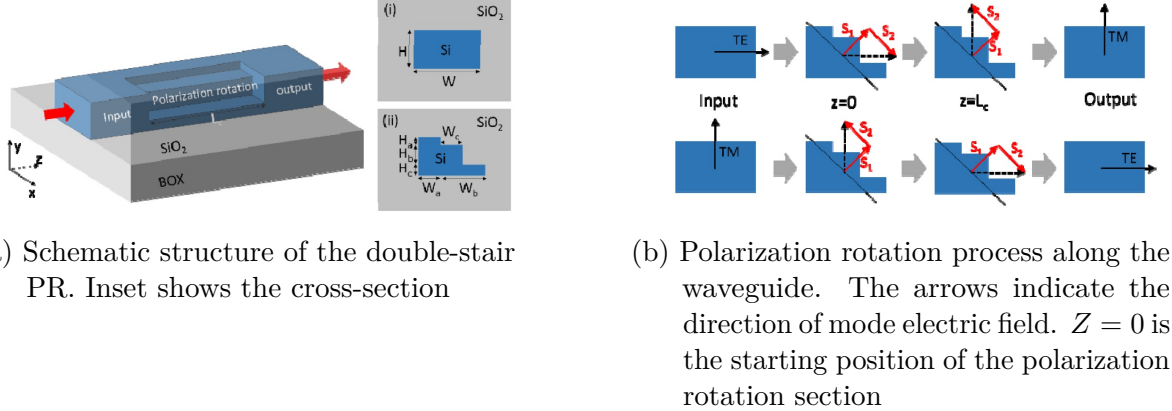


Figure 3.5: PR using double-stair waveguide mode hybridization, by Xie *et al.* [29]

The schematics of the PR (Fig. 3.5a) consists of the polarization rotation sections and describes the mode conversion along the waveguide.

Other designs for mode hybridization have also been proposed [55, 56], which work on the same principle.

- **Problem of mode hybridization:** The narrow trenches (~ 10 nm wide) required for mode hybridization are difficult to pattern and etch with controllable profiles. Recently, a PR [58] is realized on a simple strip waveguide by cutting one upper corner of the waveguide in a two-step etch process following the original idea in [57]. The pure silicon solution [58], without the need of extra materials is attractive, but the measured PER is relatively low around ~ 6 dB within a ~ 30 nm bandwidth. Although, the double-stair waveguide [29], offers good results but they exhibit wavelength-dependent loss because its working principle relies on interference.

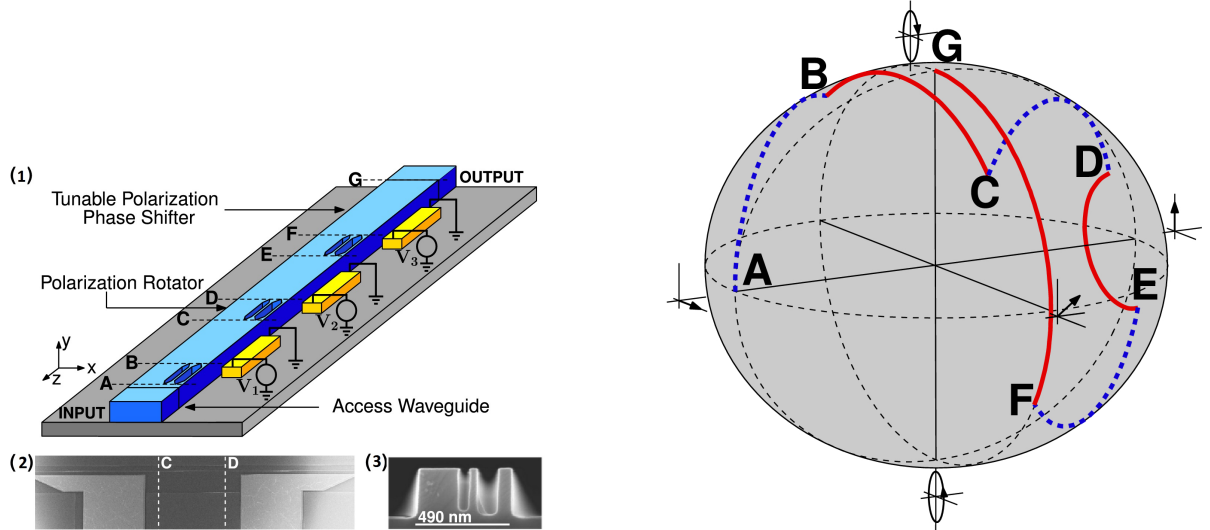
3.3.2 Active PR

An active PR is generally achieved by multiple tunable controllers which gives a good trade-off between integration and performance.

3.3.2.1 Tunable PR with thermo-optic effect

The PRs mainly change the PER, whereas the Tunable polarization phase shifters (TPPS) control the polarization phase. The TPPS are implemented using waveguide heaters placed alongside the waveguide to avoid losses due to interaction of the evanescent field with the metal. The intensity of the waveguide heaters are electrically controlled.

□ Design: Tunable PR with phase shifters



(a) Schematic of the polarization controller along with the cross section of the PR, which uses mode hybridization. The cross section of mode hybridization PR can be seen in (3)

(b) Evolution of SOP throughout the device

Figure 3.6: PR control using three PR and three TPPS, by Merenguel *et al.* [36]

In the passive PRs, the individual PR had to produce an exact polarization conversion. This was overcome by the design of the PR in Fig. 3.6a. The PR (Fig. 3.6a) consists of three PRs and three TPPS which control the SOP. The operation of the device is illustrated in Fig. 3.6b using the Poincaré sphere 2.7. First, a certain PR will be performed in the first PR (point B). Following the first PR there are two pairs of TPPS-PR. Each TPPS will tune the polarization phase in order to feed the PRs with the suitable polarization phase so that, at the output of the third PR (point F), the desired PER is achieved. The last TPPS then produces the appropriate polarization phase shift so that the desired SOP is obtained at the output (point G).

- **Drawbacks of PR with thermo-optic effect:** Although, the design offers good trade-off between performance and size but still it is limited by the fact that thermal effect can induce phase shift in other waveguides due to cross-talk. This may occur when this system is used in commercial designs with high packing density.

3.3.2.2 Tunable PR using Berry's phase

Berry's phase is a quantum-mechanical phenomenon that may be observed at the macroscopic optical level through the use of an enormous number of photons in a single coherent state [59]. In the special case of planar (non-helical) paths, such as the paths typically taken by planar optical waveguides, no significant optical rotation is

observed independent of the complexity of the path [60]. The key to manifest Berry's phase in photonic integrated circuits is to introduce out-of-plane three-dimensional waveguides to create a two-dimensional momentum space with non-zero (Gaussian) curvature.

□ Design: Tunable PR with Berry's phase

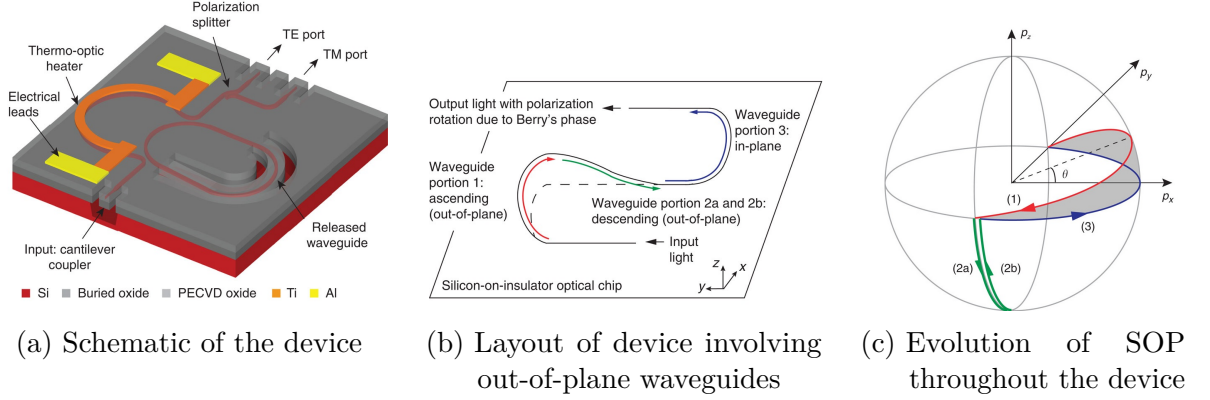


Figure 3.7: PR control using three PR and three TPPS, by Xu *et al.* [37]

Monochromatic light at wavelength λ carries a momentum given by $p = p_x\hat{x} + p_y\hat{y} + p_z\hat{z} = \hbar k$, where k is the propagation vector, with magnitude $2\pi/\lambda$ and \hbar is the Planck's constant divided by 2π . In physical space, the layout consists of three main portions. The first portion, shown in red in Fig. 3.7b, consists of an ascending out-of-plane 180° waveguide bend. The second portion, shown in green, consists of an out-of-plane waveguide that descends to the chip surface. Finally, the third portion consists of an in-plane 180° bend. In momentum space, the corresponding paths for each waveguide portion are shown in Fig. 3.7c using Poincaré sphere (2.7). Light propagation along the three-dimensional path in physical space results in a non-zero subtended solid angle in momentum space, shown as the shaded area in Fig. 3.7c. Therefore, the waveguide geometry will exhibit Berry's phase. A change in wavelength results in a change of the radius of the sphere in momentum space but not the solid angle. If the deflection angle of waveguide portion 1, in the physical space shown in Fig. 3.7b is θ , then the output light will appear with polarization rotation equal to 2θ due to Berry's phase because the magnitude of the solid angle extended by the grey area in momentum space, shown in Fig. 3.7c, is θ [37].

□ Drawbacks of PR using Berry's phase: This device uses out-of-plane ring cavity which uses the principles of ring resonator. The ring resonator is limited by its narrow band spectral features which limits bandwidth. Also, the device uses a non-birefringent waveguide, which is lossy in terms of photonic substrate, as an oxide cladding is used to confine light.

3.3.3 Other polarization tuning mechanisms

3.3.3.1 Thermal tuning

Thermal tuning mechanisms rely on the thermo-optic effect of materials, where their RI changes with temperature. In silicon, the thermo-optic coefficient (dn/dT) around 1550 nm and 300 K is about $+1.8 \times 10^{-4} K^{-1}$. Above room temperature, this coefficient increases with a weak quadratic dependence. Similarly, the thermo-optic coefficient of materials such as InP, GaAs, and SiC also increase quadratically with temperature.

3.3.3.2 MEMS tuning

MEMS tuning refers to the integration of MEMS with photonic devices. When applied to micro-resonators, the evanescent field of the resonant mode can be externally perturbed, either from the top or from the side. Two effects may result as a consequence of such perturbation: change in the effective index of refraction of the mode inside the resonator (since the evanescent tail of the mode sees a different cladding), and increase in the optical loss due to coupling/absorption of the propagating mode into/by the perturbing structure. Coupling ratios between bus waveguides and micro-resonators can also be modified through mechanical movement of suspended bus waveguides, normally needed for post-fabrication tuning or trimming [61]. Opto-mechanical tuning by electrostatic actuation can potentially provide a broad wavelength tuning range, while requiring low energy for operation.

4 Design and simulation

Chapter 4

TPR can be achieved in different ways, discussed in section 3.3.2. In this thesis, the goal is to achieve TPR using MEMS for a broadband transmission, including the C and L bands. Moreover, the idea is to optimize the design to achieve high PER and low IL.

4.1 Approach

MEMS TPR design can be approached in 2 ways. In a first approach, initially a passive PR can be designed by introducing asymmetry and a MEMS tunable waveguide is introduced which impedes polarization rotation by reintroducing symmetry in the effective waveguide. In a second approach, the technique is reversed i.e. the MEMS tunable waveguide is used to introduce asymmetry in the waveguide structure which rotates polarization. Without the MEMS structure the polarization is not rotated. In the design principle of the TPR described here, the first approach is being followed.

4.2 Designing TPR

To design the geometry of the waveguide, standard mode solver softwares are used. Both, Comsol[64] and CST [65] are used to solve the modes in equation 2.16. Mostly, in this thesis, Comsol is used to find and optimize the port modes in 2-D geometry. Whereas, CST is used to optimize the 3-D structure by studying the transmission parameters of the wave (S-parameters).

4.2.1 Design principle

To design a PR in nanometer scale, precision is a key factor. Meshing of the geometry, cladding dimensions and its material composition, frequency range of the solvers, boundary conditions, volume of simulated area chosen, etc. are the key things to watch for in designing the simulation in the mode solver softwares. As the idea is to make the TPR as broadband as possible, it is necessary to do frequency analysis simulation for a wide-band spectrum in which the optical fibers for telecommunications work. As the operating wavelength of the telecommunications optical fiber network in C-band and L-band are

between 1530 nm and 1625 nm, the corresponding frequency range becomes 195.94 THz - 184.48 THz.

4.2.2 Design: Mode hybridization based single stair Si waveguide with air cladding

If, a light source polarized at an angle θ , is incident on a half wave plate (2.6.3.2), then the final SOP is derived using Jones matrix (2.6.2), described as follows:

$$\begin{pmatrix} 1 & 0 \\ 0 & -1 \end{pmatrix} \begin{pmatrix} \cos \theta \\ \sin \theta \end{pmatrix} = \begin{pmatrix} -\cos \theta \\ -\sin \theta \end{pmatrix} = \begin{pmatrix} \cos(-\theta) \\ \sin(-\theta) \end{pmatrix}, \quad (4.1)$$

where, $\begin{pmatrix} 1 & 0 \\ 0 & -1 \end{pmatrix}$ is the Jones matrix for the half wave plate derived using 2.28 and $\begin{pmatrix} \cos \theta \\ \sin \theta \end{pmatrix}$ is the Jones vector representation of linearly polarized wave at an angle θ , with the horizontal, derived using 2.21. This concludes that an incidence of θ , produces an output of $-\theta$, when passed thorough a wave plate, which gives 2θ polarization rotation. Thus to rotate polarization by 90° , an incidence of 45° is necessary on the wave plate. The single stair waveguide acts as an wave plate due to its asymmetric structure which guides TE and TM modes at different speeds in different axes. To find out the dimensions for obtaining 45° hybridized modes in the single stair waveguide, Comsol 2D mode solver software is used.

4.2.2.1 Waveguide geometry

Throughout the next sections the dimensions of the stair waveguide are defined in terms of rib, slab and base described in Fig. 4.1.

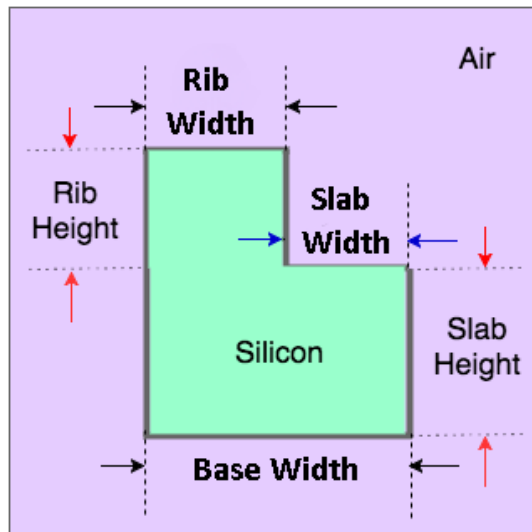


Figure 4.1: Stair waveguide geometry

4.2.2.2 Optimized dimensions of primary PR waveguide

The dimensions of the stair waveguide is optimized to get hybridized modes. At 45° , the components of the E-fields in the hybridized modes must be such that, $E_X \approx E_Y$. It is necessary to double check the E-fields orientation to make sure that only the correct modes are chosen because in simulation a larger cross-section than the waveguide cross-section is excited. This excitation might produce modes for which $E_X \approx E_Y$, but the modes are not hybridized at 45° . Hence, for modes hybridized at 45° , $\frac{\text{Avg}(E_{X_{mode}})}{\text{Avg}(E_{Y_{mode}})} \rightarrow 1$. As a result,

$$\text{Electric field ratio in hybrid modes} = \sum_{\text{mode}} \text{Real} \left| \log_{10} \frac{\text{Avg}(E_{X_{mode}})}{\text{Avg}(E_{Y_{mode}})} \right| \rightarrow 0. \quad (4.2)$$

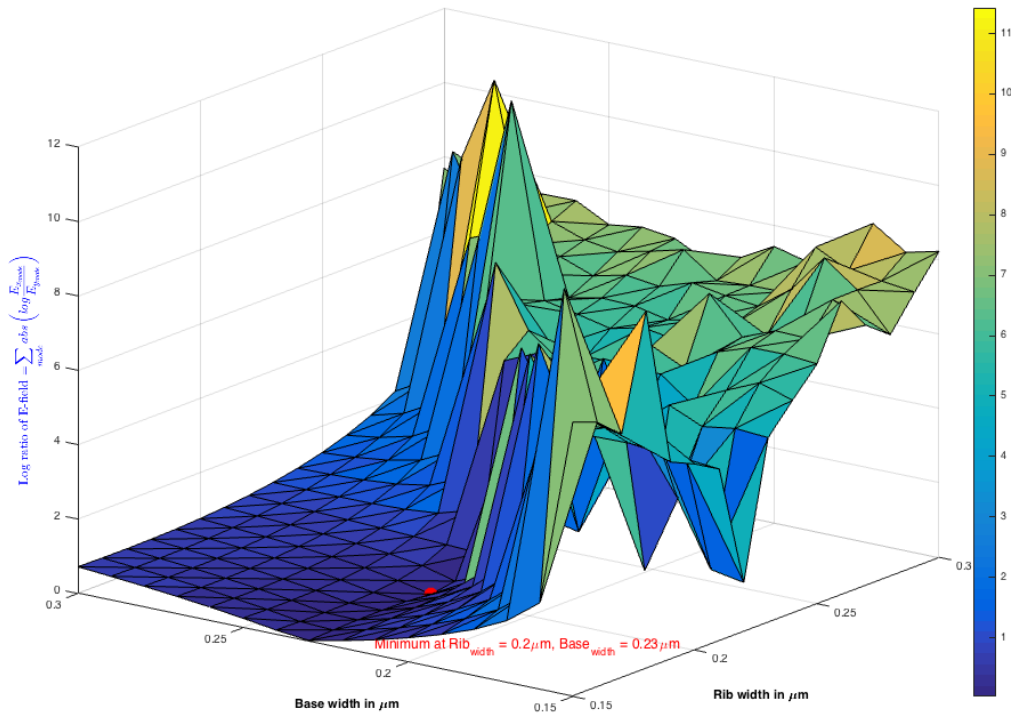


Figure 4.2: Summation of real part of absolute value of the logarithmic ratio of E_x and E_y fields plotted against rib and base width in an area chart using MATLAB

Hence, the minimum point on the graph represents the best dimensions on the waveguide for obtaining the hybridized modes at 45° . In this case the best dimensions were obtained at $\text{Base}_{\text{width}} = 230 \text{ nm}$ and $\text{Rib}_{\text{width}} = 200 \text{ nm}$. The total height of the waveguide is

220 nm and the $\text{Slab}_{\text{height}} = 110$ nm. It can be visualized that in the modes in Fig. 4.3a and Fig. 4.3b, that the effective modes are hybridized at 45° for the first 2 hybrid modes obtained using Comsol simulation. Lastly, the height in the geometry is chosen around 110 nm for the current limitation of the dry-etch step in the fabrication process present in the lab. A double stair waveguide could also have been chosen, but that would increase the fabrication steps.

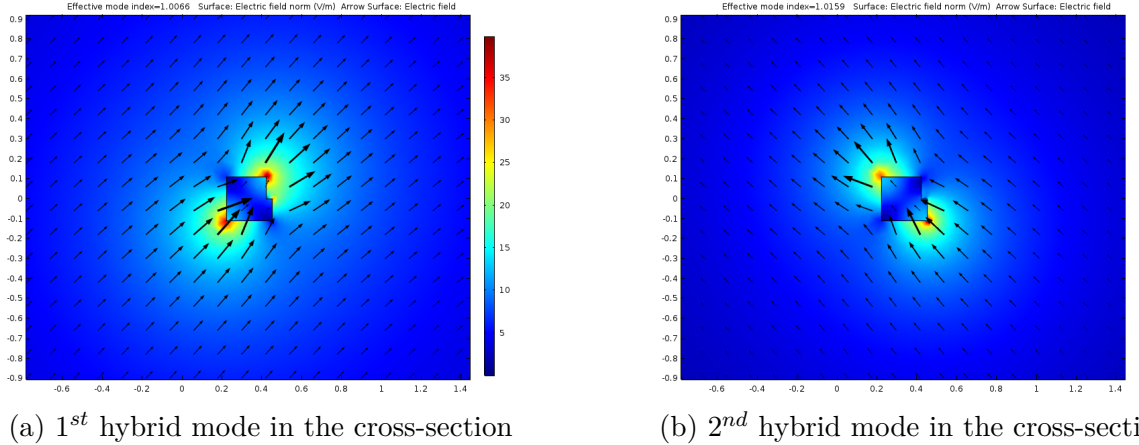


Figure 4.3: Fundamental hybrid modes in the cross-section with $\text{Rib}_{\text{width}} = 200$ nm, $\text{Rib}_{\text{height}} = 110$ nm, $\text{Base}_{\text{width}} = 230$ nm, $\text{Slab}_{\text{height}} = 110$ nm, obtained using Comsol 2-D eigenmode simulation

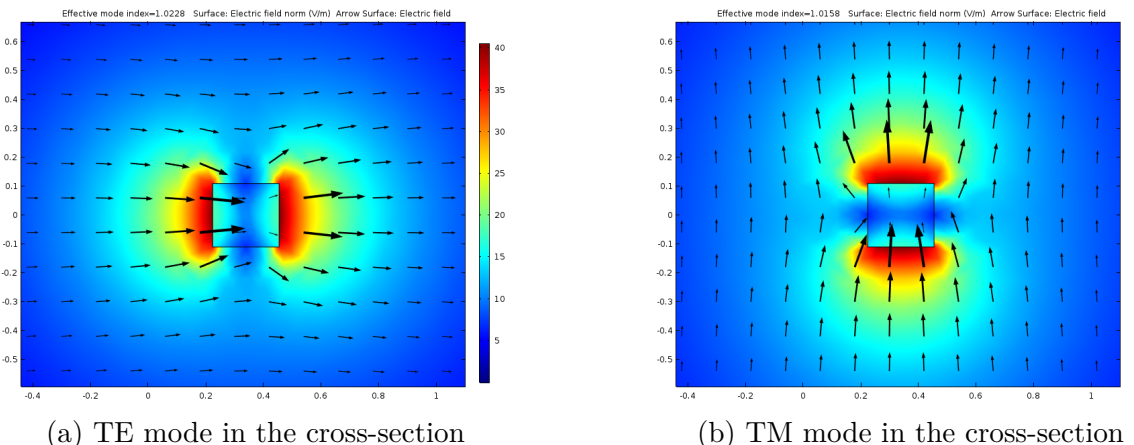


Figure 4.4: Fundamental modes in the cross-section with Width = 230 nm, Height = 220 nm, obtained using Comsol 2-D eigenmode simulation

Also, since the input and output port dimensions in the waveguide are different from the stair waveguide cross-section dimension, it is necessary to check if the 2 fundamental modes can be supported by the input and output ports. Hence, port mode simulation for the first two fundamental modes in waveguide with dimensions 230×220 nm are

calculated and the results obtained are displayed in Fig. 4.4a and Fig. 4.4b. This corroborates that the 2 fundamental modes TE and TM are supported in the input and output ports.

Next, the effective RI for both the port modes are obtained using CST by doing a parametric sweep over the operating frequencies of C and L-band. The results are displayed in Fig. 4.5.

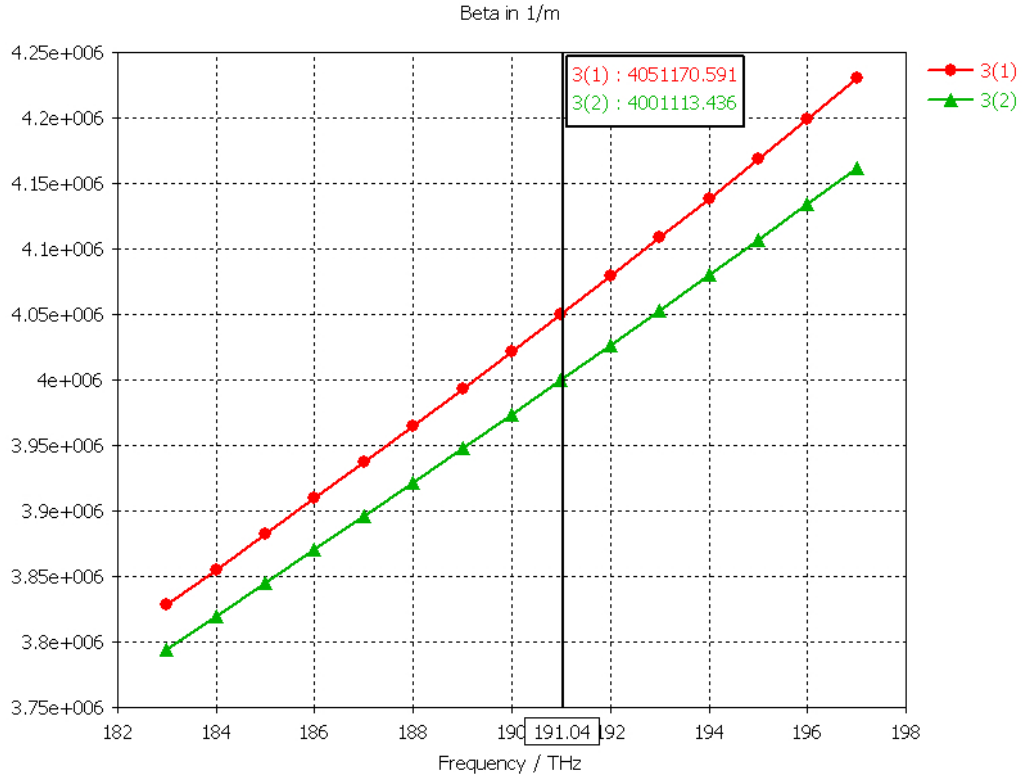


Figure 4.5: Simulated effective propagation constant for the port modes in the cross-section of $\text{Rib}_{\text{width}} = 200 \text{ nm}$, $\text{Rib}_{\text{height}} = 110 \text{ nm}$, $\text{Base}_{\text{width}} = 230 \text{ nm}$, $\text{Slab}_{\text{height}} = 110 \text{ nm}$, obtained using CST 3-D simulation

The required length of the cross-section is obtained using 2.26. Since, $\beta_1 = 4.051 \times 10^6$ and $\beta_2 = 4.001 \times 10^6$. Hence, $L = \frac{\pi}{\beta_1 - \beta_2} \approx 62 \mu\text{m}$. This means the length of the stair cross-section would be around $62 \mu\text{m}$. Effective RI is dependent on frequency and so the cross-section length is also dependent on the frequency. The length is calculated at around 191 THz, so that the whole of the band (184.48 THz - 195.94 THz) can be covered for a relative good performance. This results could have also been obtained from COMSOL from the effective RI calculation as shown in 4.3.

$$L_\pi = \frac{\pi}{\beta_1 - \beta_2} = \frac{\pi}{\frac{2\pi}{\lambda} (n_1 - n_2)} = \frac{\lambda}{2(n_1 - n_2)} \quad (4.3)$$

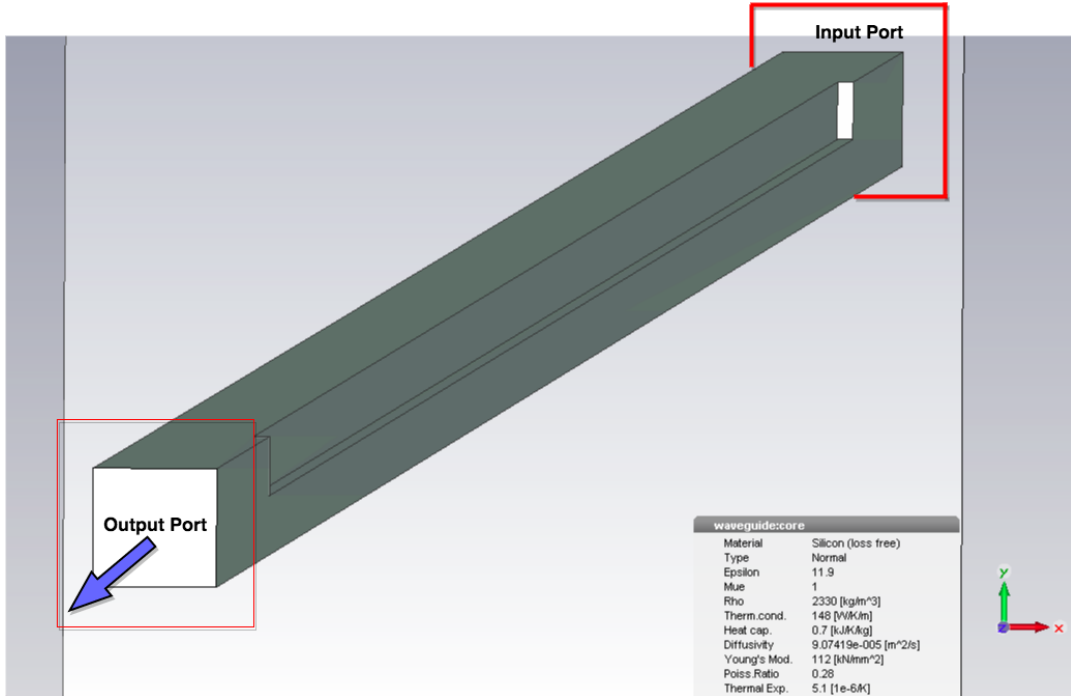


Figure 4.6: Design of single-stair waveguide with initial dimensions at the port as width = 230 nm and height = 220 nm. Stair cross-section dimensions are: Rib_{width} = 200 nm, Rib_{height} = 110 nm, Base_{width} = 230 nm, Slab_{height} = 110 nm, and cross-section length = 62 μ m. The output port is along the Z-axis, shown in the figure

The 3D-design is simulated in CST with air cladding and with the previously estimated dimensions. The input and output ports are defined on the waveguide, which supports the two fundamental modes. As shown in Fig. 4.6, the stair cross-section can be envisaged if a Z-plane is cut in the asymmetric part of the waveguide.

Next, the S-parameters of the design are verified. The S-parameters are labelled as follows,

$$SA(M), SB(N), \quad (4.4)$$

where A=output port, B=input port and M,N = mode number. For example, S2(2),S1(1) means that input port is 1 and the mode is 1 whereas, output port is 2 and the mode at the output port is 2. Hence, S2(1),S1(2) and S2(2),S1(1) needs to be checked along with S2(1),S1(1) and S2(2),S1(2) for calculating the PER. The S-parameters obtained from the simulation shown in Fig. 4.7 (for, 200×230 nm) verifies that the model works according to the design principle with good PER over the C and L-band.

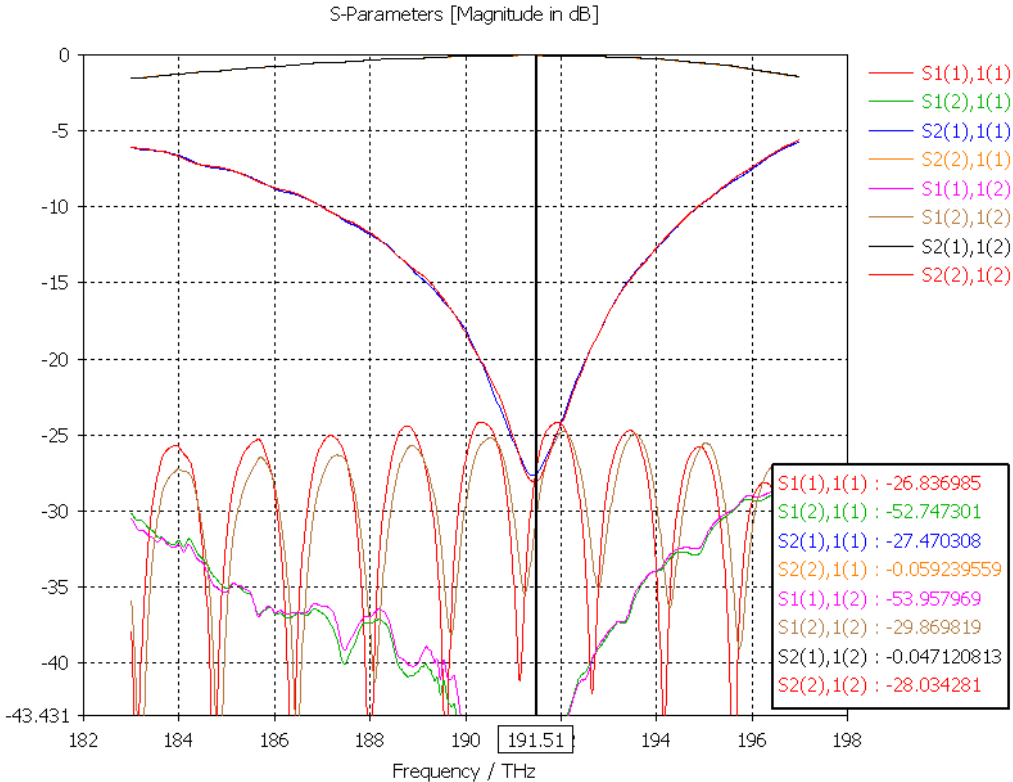


Figure 4.7: Simulated S-parameters in the single-stair waveguide with initial dimensions at the port as width = 230 nm and height = 220 nm. Stair cross-section dimensions are: Rib_{width} = 200 nm, Rib_{height} = 110 nm, Base_{width} = 230 nm, Slab_{height} = 110 nm, and cross-section length = 62 μ m obtained using CST 3-D simulation

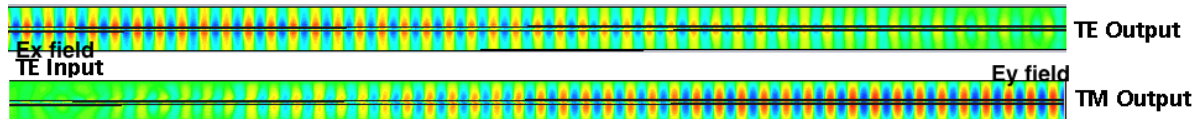


Figure 4.8: TE-TM mode conversion along the waveguide with decreasing E_x field and increasing E_y field

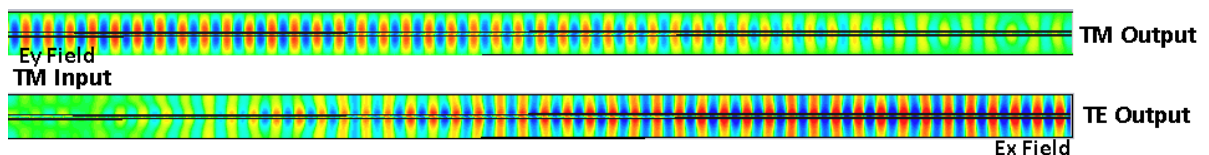


Figure 4.9: TM-TE mode conversion along the waveguide with decreasing E_y field and increasing E_x field

4.2.2.3 Optimized dimensions of MEMS waveguide

After finding the dimensions of the passive PR, the MEMS tunable waveguide was designed to cancel the effect of rotation. Intuitively, if any waveguide which is the mirror image of the bus waveguide is placed along side the bus waveguide, then PR effect would be nullified. This is verified by plotting the graph in Fig. 4.10. Since, at TE or TM mode, $E_X \gg E_Y$, or $E_Y \gg E_X$. Hence, $\left| \frac{\text{Avg}(E_{X_{\text{mode}}})}{\text{Avg}(E_{Y_{\text{mode}}})} \right| \rightarrow \infty$, or $\left| \frac{\text{Avg}(E_{Y_{\text{mode}}})}{\text{Avg}(E_{X_{\text{mode}}})} \right| \rightarrow \infty$, depending on TE or TM-mode. Hence,

$$\sum_{\text{mode}} \text{Real} \left| \log_{10} \frac{\text{Avg}(E_{X_{\text{mode}}})}{\text{Avg}(E_{Y_{\text{mode}}})} \right| \rightarrow \infty, \quad (4.5)$$

and the maximum points on the graph will represent the dimensions of the MEMS structure for which, there is no PR. Logarithmic scale is used to plot the data in a manageable way. The supermodes are also verified in the cross-section in Fig. 4.11a and Fig. 4.11b to make sure higher order modes are not excited.

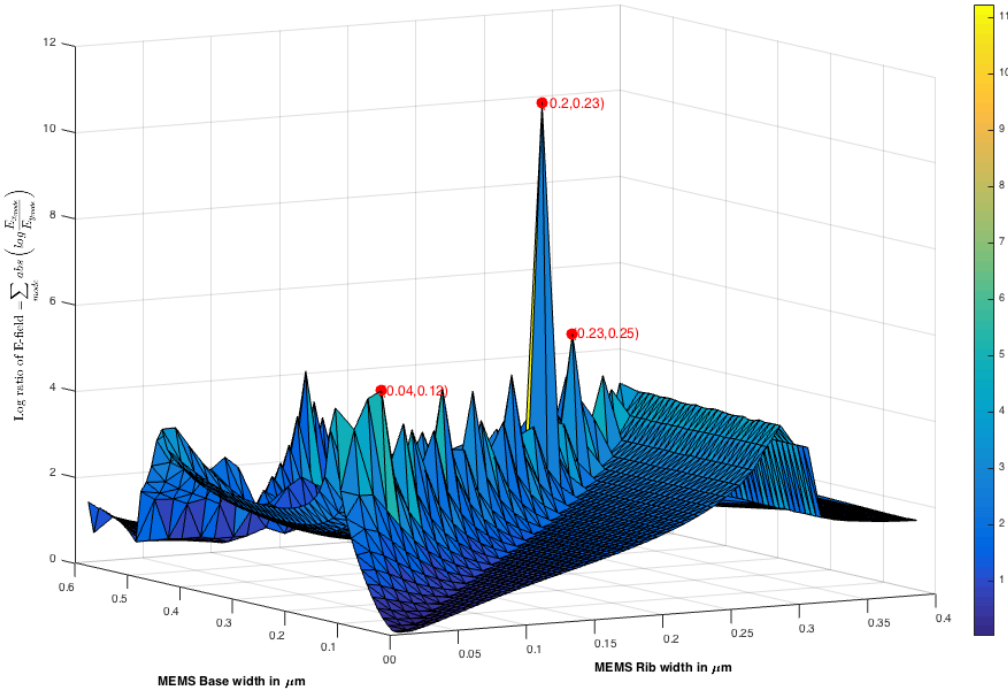
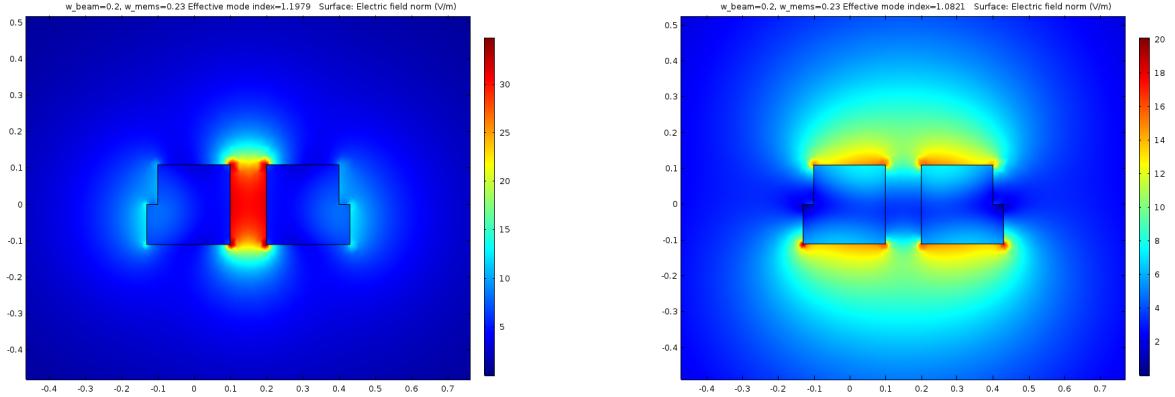


Figure 4.10: Summation of real part of absolute value of the logarithmic ratio of E_x and E_y fields plotted against rib and total width in an area chart using MATLAB



(a) TE mode with the MEMS cross-section

(b) TM mode with the MEMS cross-section

Figure 4.11: Modes in the cross-section with $\text{Rib}_{\text{width}} = 200\text{nm}$, $\text{Slab}_{\text{width}} = 30\text{ nm}$, $\text{Slab}_{\text{height}} = \text{Rib}_{\text{height}} = 110\text{ nm}$, in both bus and MEMS waveguide, obtained using Comsol 2-D simulation

In this case the best dimensions for the MEMS waveguide comes out as, $\text{Rib}_{\text{width}} = 200$ nanometer, $\text{Rib}_{\text{height}} = 110$ nanometer, $\text{Base}_{\text{width}} = 230$ nanometer, $\text{Slab}_{\text{height}} = 110$ nanometer. Fig. 4.11a and Fig. 4.11b, obtained using Comsol 2D simulation displays the port modes in the cross-section. This corroborates the claim that the MEMS waveguide must be mirror image of the bus waveguide to inhibit PR.

4.2.2.4 Design of primary PR waveguide with MEMS waveguide

Based on the simulations performed and the dimensions of the cross-section obtained the tunable PR was designed as depicted in Fig. 4.12. For quicker simulation purposes the remaining portions of the cantilever in the MEMS waveguide are not considered in the simulation design.

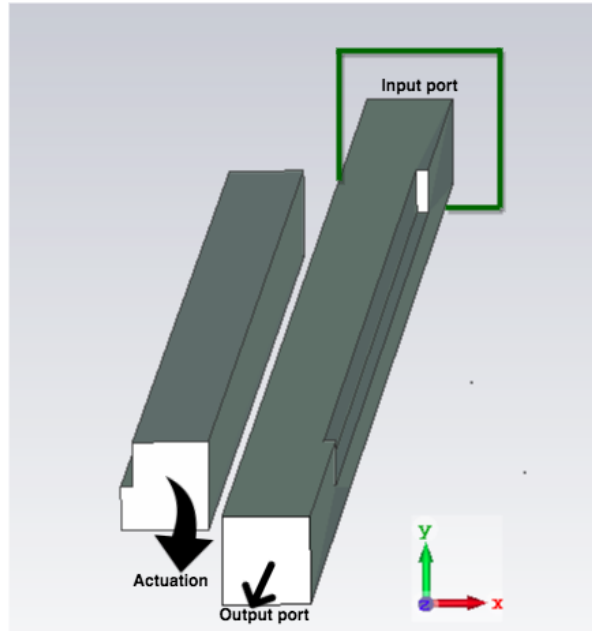


Figure 4.12: Design of single-stair waveguide with MEMS tuning waveguide. Stair cross-section dimensions are: $\text{Rib}_{\text{width}} = 200 \text{ nm}$, $\text{Rib}_{\text{height}} = 110 \text{ nm}$, $\text{Slab}_{\text{width}} = 230 \text{ nm}$, $\text{Slab}_{\text{height}} = 110 \text{ nm}$, and cross-section length = $62 \mu\text{m}$, in both the PR waveguide and MEMS waveguide. The output port is along the Z-axis

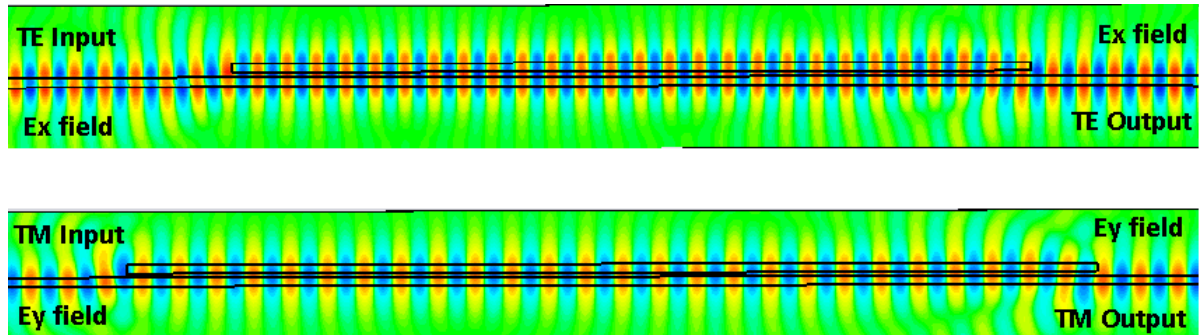


Figure 4.13: TPR transmission in silica cladding without MEMS waveguide actuation

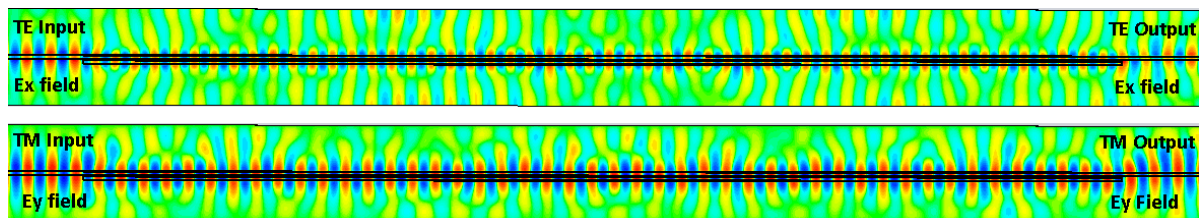


Figure 4.14: TPR transmission in air cladding without MEMS waveguide actuation

4.2.2.5 Device tolerance

When fabricating devices in nanometer scale often it is very difficult to control the device dimensions precisely. Hence, a brief study on simulation level is performed to check for deviance resulting due to variations in etch depth during the fabrication process discussed later in section 5.

Since the wafer used in the fabrication process is of height 220nm, the different etch depths considered are 100nm and 130nm which corresponds to 120nm and 90nm slab height respectively. First 20 minimum values of $\sum_{mode} \text{Real} \left| \log_{10} \frac{E_{X_{mode}}}{E_{Y_{mode}}} \right|$, is plotted against Rib_{width} and Slab_{width} in the following figure in Fig. 4.15 for an etch depth of 100nm.

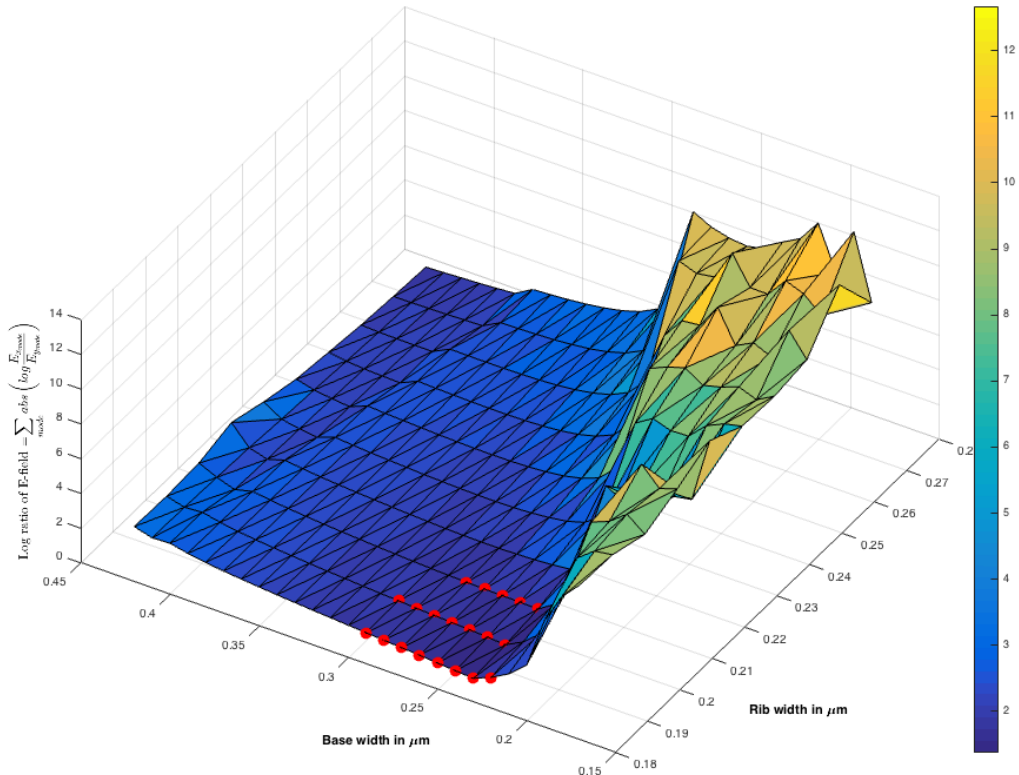


Figure 4.15: 20 least values, representing the summation of real part of absolute value of the logarithmic ratio of E_x and E_y fields, plotted against rib and total width in an area chart using MATLAB for Slab_{height} = 120 nm

It can be seen in the above Fig. 4.15 that the hybridized modes appear to be at 45° around $230 \text{ nm} \leq \text{Base}_{\text{width}} \leq 300 \text{ nm}$ and $180 \text{ nm} \leq \text{Rib}_{\text{width}} \leq 200 \text{ nm}$. So, if the Rib_{width} and

$\text{Base}_{\text{width}}$ are controlled in the fabrication process, the device can still function and needs to be characterized accordingly.

The same process is followed for a speculated etch depth of 130 nm and the 20 best dimensions are plotted which comes out to be $230 \text{ nm} \leq \text{Base}_{\text{width}} \leq 300 \text{ nm}$ and $160 \text{ nm} \leq \text{Rib}_{\text{width}} \leq 200 \text{ nm}$. The exact pairs can be identified in the Fig. 4.16.

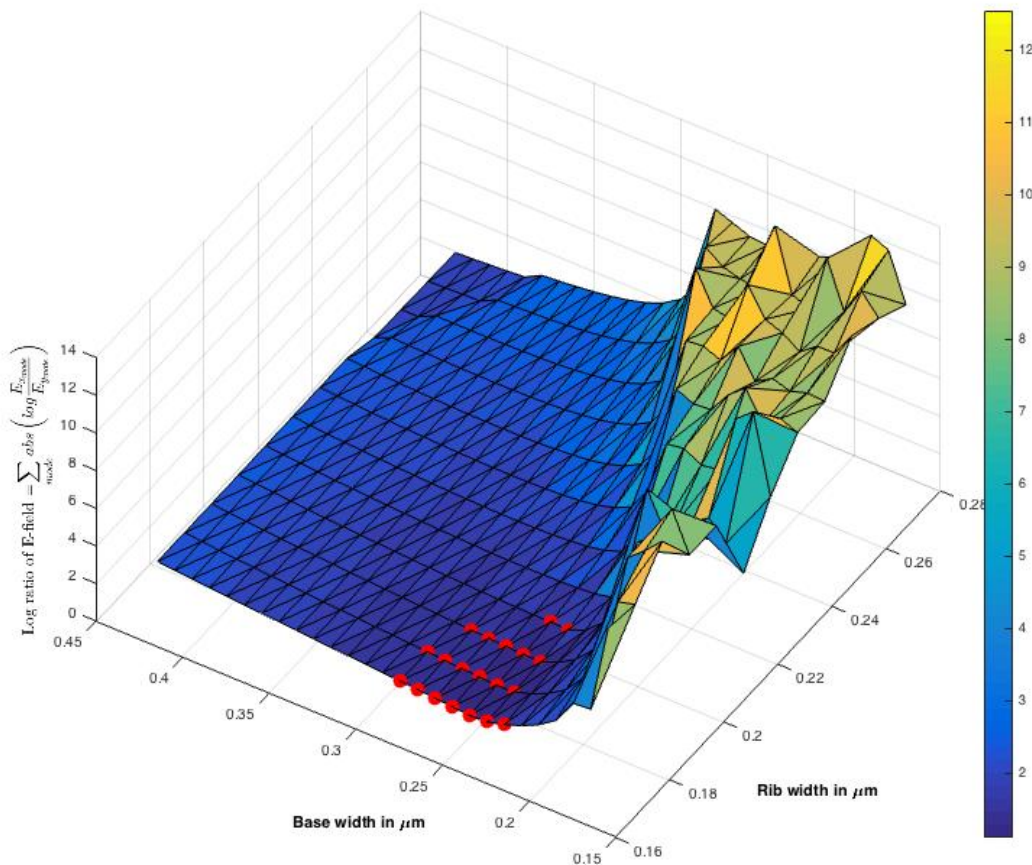


Figure 4.16: 20 least values, representing the summation of real part of absolute value of the logarithmic ratio of E_x and E_y fields, plotted against rib and total width in an area chart using MATLAB for Slab height = 90 nm

4.3 Designing auxiliary components for measurement setup

To test the TPR auxiliary components like grating couplers (TE & TM), tapers, Polarization Beam Splitter (PBS) are designed. The gratings are designed in way to couple

TE and TM-modes from the LASER to the waveguide. However the gratings have a width of $12\text{ }\mu\text{m}$ whereas, the TPR section in the waveguide has width of 230 nm . Hence, tapers are used to reduce the mode size and guide light into the TPR section. Finally, a PBS is designed which again splits the TE and TM-modes and guides them to the TE and TM grating couplers respectively via tapers where a photo-detector measures the intensity of output light. Another approach like butt-coupling can be used. But it is difficult to couple light into narrow waveguides in a low-loss manner as the mode size in fiber core is bigger than the mode size in the waveguide.

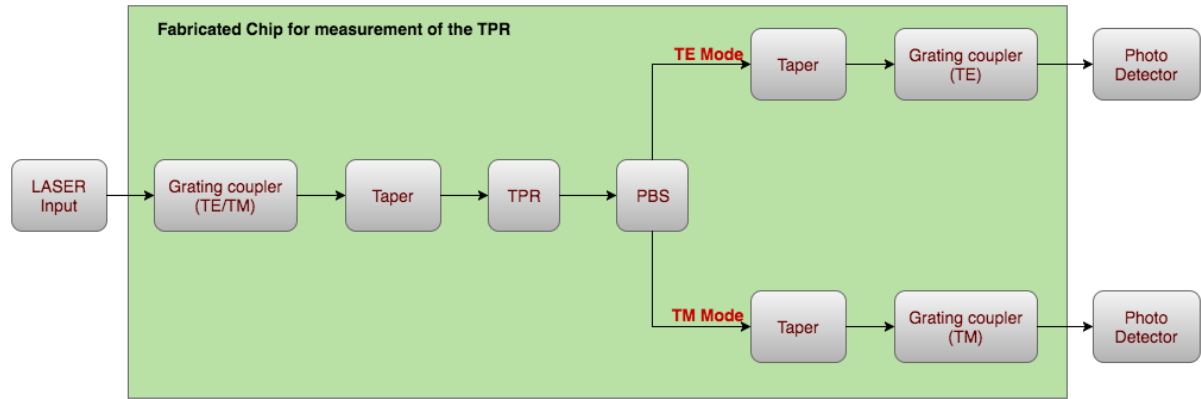


Figure 4.17: System level block diagram of the fabricated measurement setup

In the Fig. 4.17 a high level block diagram of the measurement setup is shown. Whereas, in Fig. 4.18 schematic top view of the low level system design is shown with gratings, tapers, TPR, TM coupler and bridges.

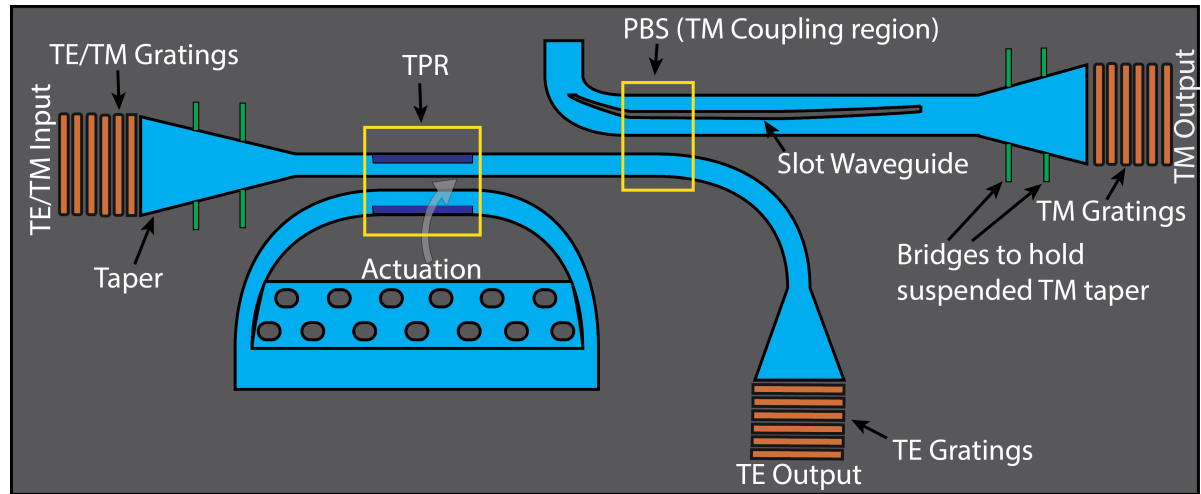


Figure 4.18: Low level schematic representation of the fabricated measurement setup

4.3.1 Grating coupler design

The high effective index and small mode dimensions of single mode silicon waveguides makes fiber coupling challenging. Waveguide-to-fiber surface grating couplers with fill factor apodization offer low back reflection into the silicon waveguide and a single required lithography step. Using surface grating couplers, the mode matching problem can be solved by expanding the width of the on-chip silicon waveguide, and etching a grating into the expanded section that diffracts light out of plane into a fiber placed normal to the surface. The approach taken increases the coupling efficiency by tailoring the leakage factor of the grating to the mode profile of the fiber. The main benefits of this approach are a low back reflection into the silicon waveguide and high efficiency in the coupling [66]. In the design, the gratings used are 12 μm wide which narrows down to a width of 230 nm in the PR section. The approach is shown in Fig. 4.19a.

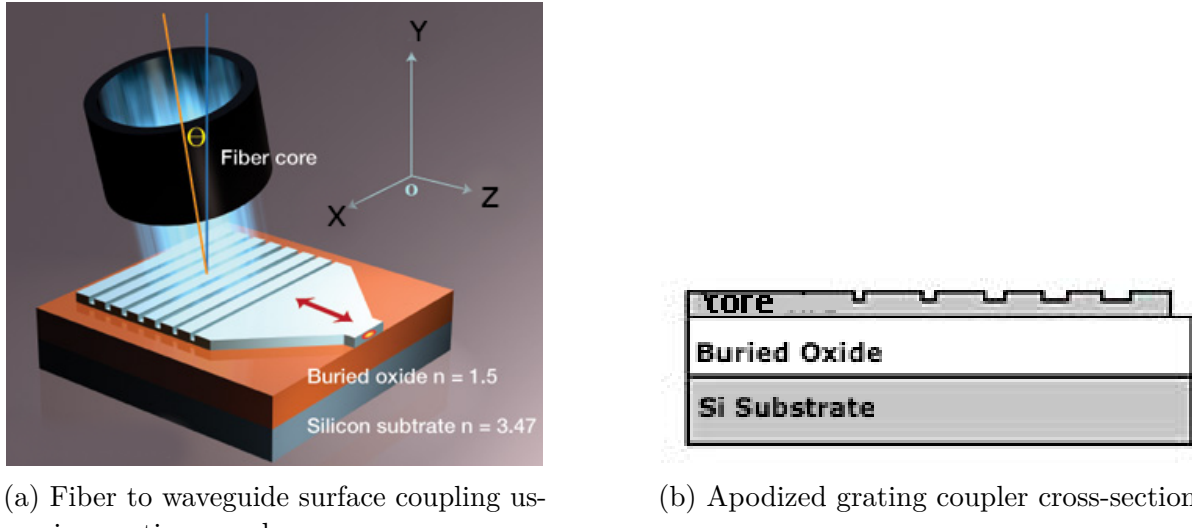


Figure 4.19: Overview of surface coupling from fiber to waveguide using apodized grating coupler with cross-sectional view

4.3.2 Taper with bridge design

While tapering down to the TPR cross-section from the grating coupler cross-section, the SiO_2 underneath is etched away. Hence, to support the structure from the side bridges are constructed which forms a slab like structure at certain cross-sections. These kinds of structures accommodate mode conversions between TM_0 and TE_3 . Also, these bridges are constructed in other places in the waveguide structure where support is necessary to hold the waveguide. For example, if the core waveguide width is 700 nm then a total base width (core and bridge) of 1500 nm must be avoided for mode conversion reasons. This is simulated using COMSOL and the results are plotted in Fig. 4.20. As, it can be seen that around 1500 nm base width there is a mode conversion between TM_0 and TE_3 represented in Fig. 4.21a and Fig. 4.21b. However, there is no mode conversion between

TM_0 and TE_2 , since the field distributions are not similar and hence they do not couple.

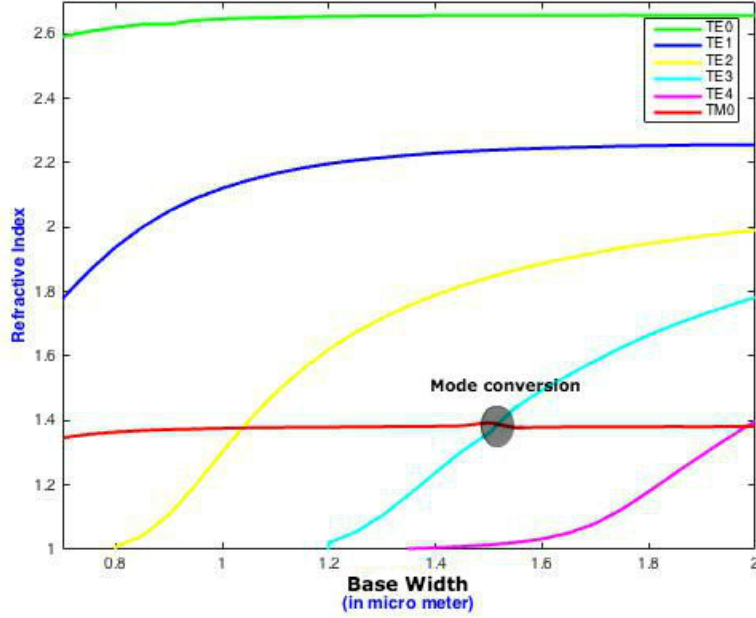


Figure 4.20: TE and TM modes at different base widths obtained using COMSOL mode solvers

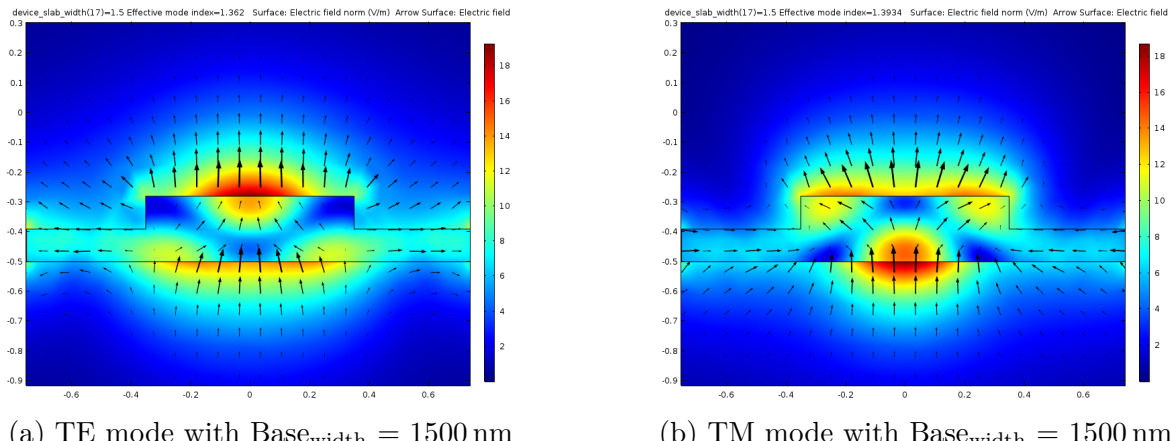


Figure 4.21: Mode conversion in Slab modes at $\text{Base}_{\text{width}} = 1500 \text{ nm}$, obtained using Comsol 2-D simulation

4.3.3 Polarization beam splitter design

The PBS is based on an asymmetrical directional coupler utilizing the evanescent coupling between a strip-waveguide and a nanoslot waveguide [67]. First, effective RI is calculated for different core widths with height = 220 nm. The results are displayed in Fig. 4.22.

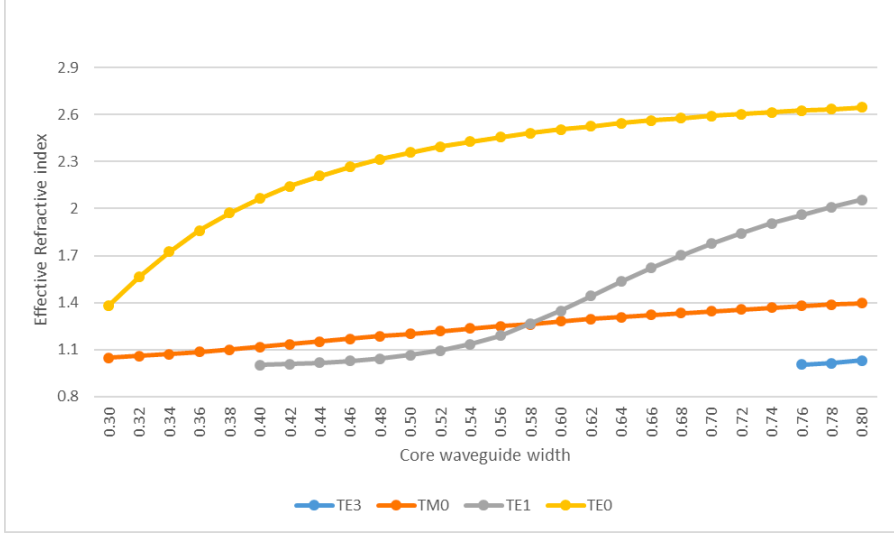


Figure 4.22: Effective RI for different dimensions of core waveguide width

Next, the RI is calculated for different widths of nanoslot waveguide with a height of 220 nm and slot width of 100 nm. The gap between the strip-nanowire and the nanoslot waveguide is 150 nm. The results are plotted in Fig. 4.23.

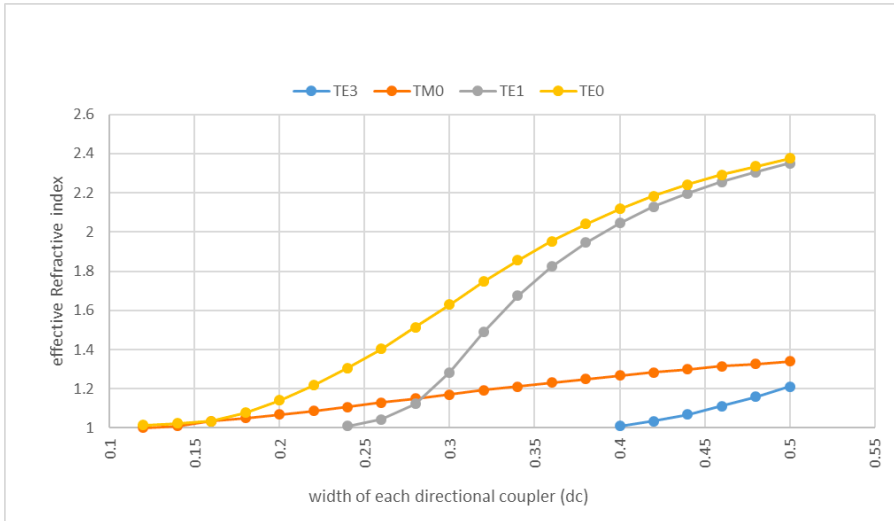


Figure 4.23: Effective RI for different dimensions of slot cross-section

It can be seen in Fig. 4.22 that the effective index of TM_0 at a width of 500 nm is 1.20. Whereas, it can be seen in Fig. 4.23 that the effective index of 1.20 in TE_1 is obtained around a width of 330 nm for each section of the nanoslot waveguide. Also, the supermodes are checked in the cross-section keeping the strip-nanowire and the nanoslot waveguide to understand the coupled modes shown in Fig. 4.24a and Fig. 4.24b.

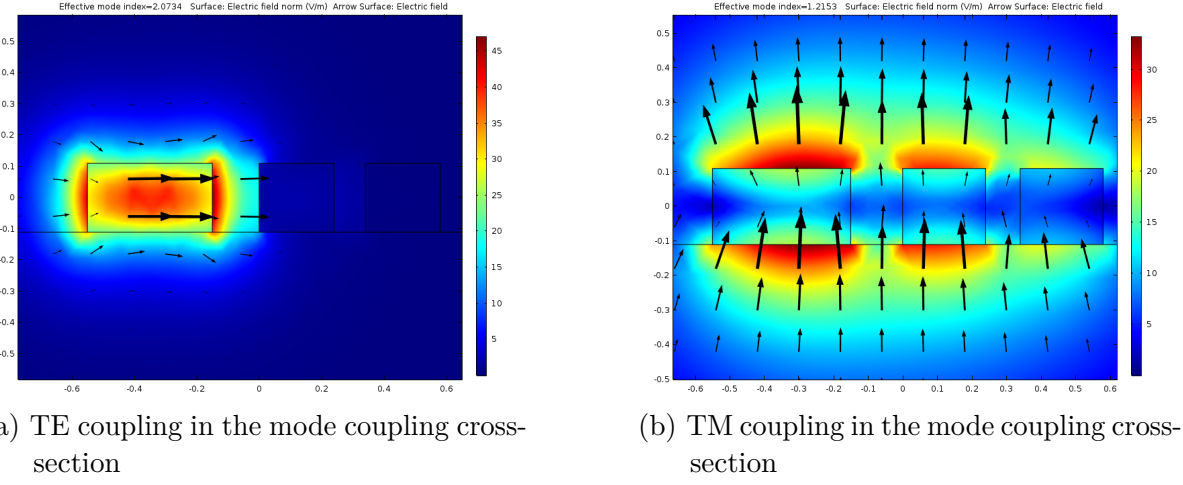


Figure 4.24: TE and TM coupling in PBS slot waveguide at the mode coupling region

Finally, the designed is simulated in 3-D using CST for checking the transmission with strip-nanowire of width 500 nm and nanoslot waveguide of width 330 nm each with slot width of 100 nm. The coupling length is estimated from 4.3. As, $n_{TE0} = 2.35$ and $n_{TM0} = 1.20$, hence $L_\pi = 1.4 \mu\text{m}$. As seen in Fig. 4.25a, the TE mode goes through without coupling. Whereas, as seen in Fig. 4.25b, the TM mode crosses through in the coupling region. As, it can be seen some portion of the TM mode goes through as well. However, the measured PER is more than 15 dB. The purpose of this setup is to make sure that both TE and TM modes can be measured at different ports. In the final design of the measurement setup the nanoslot waveguide is not bent after the coupling region to minimize losses for TM mode. As TM mode is highly deconfined, bends can cause lossy transmission for TM modes. Whereas, since TE mode is confined, the strip-nanowire core waveguide is given a sharp bend to minimize coupling beyond the coupling region. The idea can be viewed in Fig. 4.18.

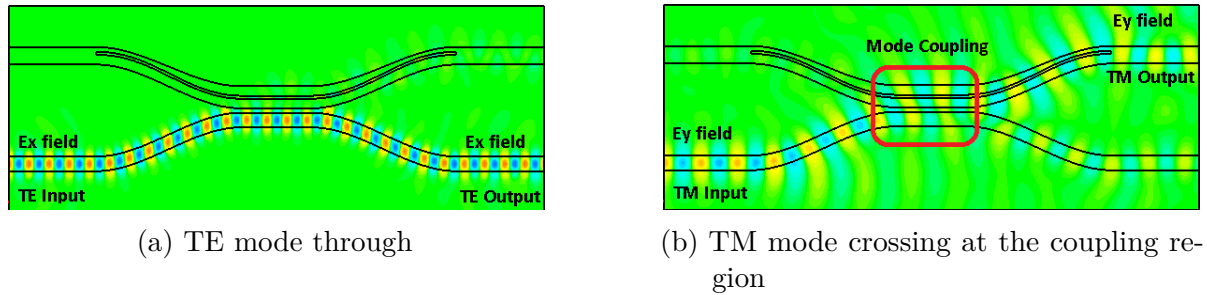


Figure 4.25: TE and TM mode propagation in a waveguide with PBS section. TE mode goes through, whereas, the TM mode crosses at the PBS region due to mode matching of the two waveguides in the PBS section

5 Chapter 5

Fabrication

The MEMS tunable device was fabricated using a standardized two step dry etch process on Silicon on Insulator (SOI) for the silicon device layer (resulting in two heights) and a wet SiO₂ under-etch [68]. The first lithography step defines the asymmetric shape of the ridge waveguides. The second lithography step and the wet under-etch defines the slab sections and free standing cantilever. The cantilever is delimited by the fully etched slot waveguides, and its free suspended area is determined by the placement of etch holes. The details of the fabrication process steps are described in the following section.

5.1 Piranha bath

The fabrication process starts with cleaning the SOI chip which has 220 nm crystalline silicon device layer and 2 μm buried oxide, in the piranha solution (Fig. 5.1 A). Piranha solution is a mixture of sulfuric acid (H₂SO₄) and hydrogen peroxide (H₂O₂), used to clean organic residues off substrates. Because the mixture is a strong oxidizing agent, it will remove most organic matter, and it will also hydroxylate most surfaces (add OH groups), making them highly hydrophilic (water-loving) [69].

5.2 HSQ resist spin

A Hydrogen silsesquioxane (HSQ) (Manufacturer: Dow Corning XR-1541-002) negative resist is spun on the SOI chip to create a thickness of 50 nm. This is achieved by spinning the chip on a spinner at 4000rpm for 30 seconds. The HSQ layer is hardened by baking the chip on a hot plate at 170° C for 5 minutes. To measure the thickness of resist a scratch is made on the chip and checked for depth variations using mechanical profilometer (KLA-Tencor). This is done to verify the profile depth of the resist mask.

5.3 First e-beam exposure

To pattern the chip, selective portions of the chip are exposed using e-beam lithography. The patterns are drawn using a CAD software (Raith 150 e-beam lithography). E-beam exposure exceeds patterning capability of optical lithography and creates patterns in

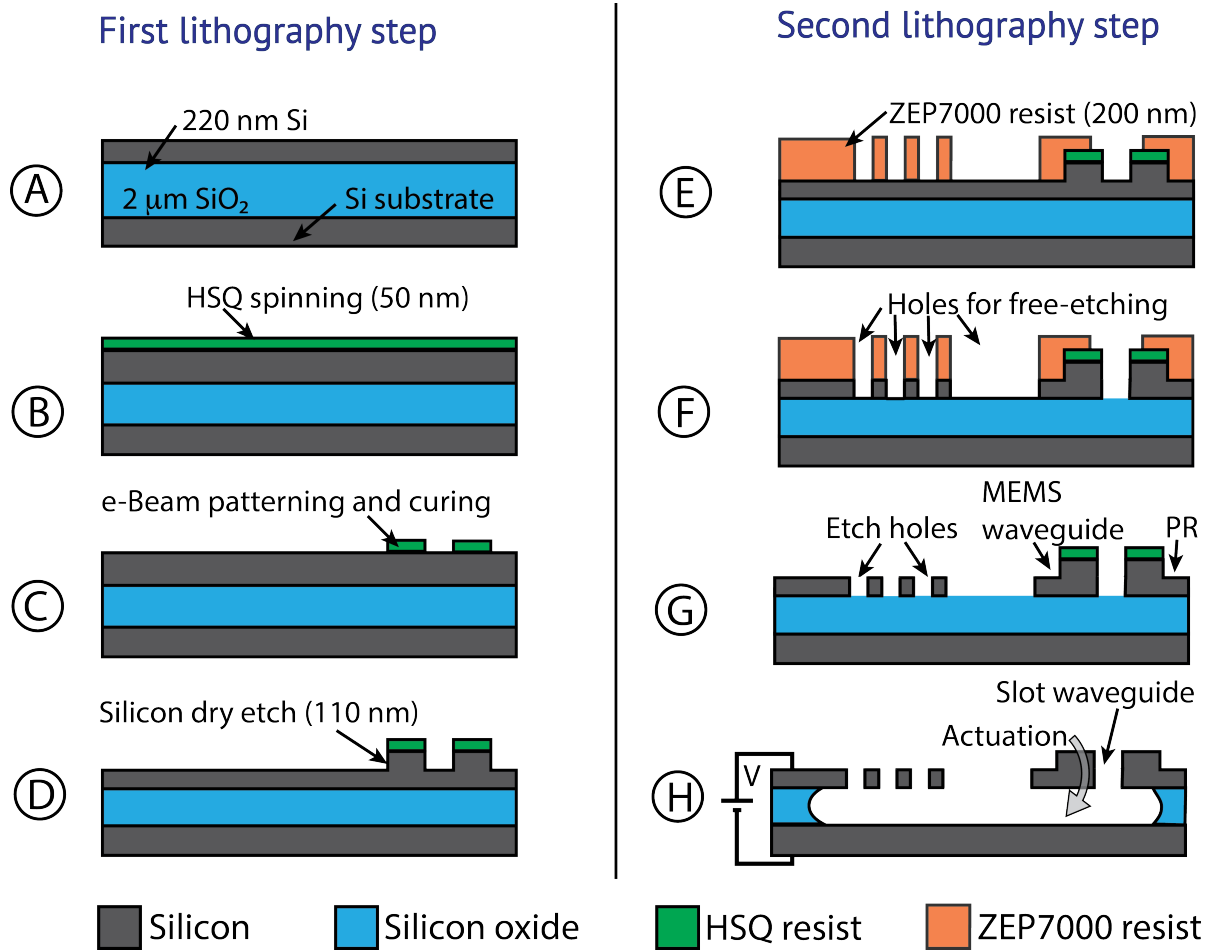


Figure 5.1: A cross-sectional schematic of the fabrication process

sub-microns scale. Initially, one corner of the chip is scratched to align the chip and find particles on the chip to focus the beam correctly. Write-field alignment is a very central adjustment in the process of getting the best possible e-beam lithographic result. It is the adjustment of the electromagnetic/electrostatic deflections system inside the column to the high precision X-Y-Z stage. The stage is considered to be “correct” and the e-beam deflection system is aligned to it. To increase the dose in certain portions of the chip, the scanning speed is slowed down so that more electrons can strike the HSQ surface and expose it with a higher dose. The chip is developed using ma-D 525 (Manufacturer: Micro resist technology) which dissolves non-hardened HSQ. The chip is then put in water to wash ma-D 525 and dried using nitrogen. Finally, the exposed HSQ on the chip is hardened more by putting it in an oven for 40 minutes at 400° C. Inside the oven the chip is covered with ceramic glass to avoid deposition of dust cloud. After this step the chip resembles the diagram in Fig. 5.1 C. Again a mechanical profilometer is used to verify the thickness of HSQ.

5.4 First dry etch step

The device pattern is finally transferred to the device layer by a timed (HBr) dry etching of silicon (≈ 35 seconds), resulting in ridge waveguides with 110 nm height on a 110 nm thick silicon slab (Fig. 5.1 D). The patterned HSQ remains on the chip for the next lithography step. Finally, optical profiling is performed to find out the depth of the silicon etch. This process marks the end of the first step lithography process.

5.5 ZEP7000 spin

An undiluted ZEP7000 (Manufacturer: Zeon Chemicals) resist (positive) is applied on the chip by using an Eppendorf pipette. To achieve a ZEP profile of 200 nm thickness the spinner is set at 3000 rpm for 45 seconds. The sample is baked at 170° C for 3 minutes to make the ZEP layer harder. After this, a scratch is then made on the sample and the profile depth is measured using a mechanical profilometer.

5.6 Second e-beam exposure

Initially, before the second e-beam exposure the beam is focused correctly and alignment to existing structures is performed because it is a two-step fabrication process. Some unique and easily recognizable feature like plus symbol is selected as a mark, patterned in the first exposure. Write-field alignment is performed in all the cells manually for maximum dimensional precision [70]. Since ZEP is a positive resist, the exposed portions are developed using p-Xylene solvent and MIBK. After developing the chip, the cross-section looks like Fig. 5.1 E.

5.7 Second dry etch step

The double step device pattern is obtained in the device layer when the unmasked silicon (without ZEP resist) is etched. This is done via another dry etch step similar to the previous one (≈ 35 seconds). The goal of this dry etch process is to etch through the remaining silicon via the holes created using ZEP resist. The ZEP polymer is cleaned via resist stripping using oxygen plasma. After this process the device cross-section looks like Fig. 5.1 F.

5.8 Wet etching and critical point drying

The final step in the fabrication is the removal of the HSQ and the underlying SiO₂ to form the free-standing MEMS waveguide with cantilever and the PR waveguide with a gap of 100 nm. The process starts with wet etching of HSQ and SiO₂ using HF for 200 seconds. The HF is diluted using cold water and then the chip is transferred to

isopropanol ($\text{CH}_3\text{CHOHCH}_3$). The surface tension of the isopropanol in a micro device is at the point at which a change from liquid to gaseous state can destroy the device through capillary forces. Also, drying free standing waveguides in air or under vacuum can drastically alter their structures or even destroy them completely. A gentle method for such purposes is critical point drying. By increasing the pressure and temperature of the substrate it is possible to dry without crossing a phase boundary. This is possible because once the critical point has been passed, the density of liquid and gas are the same. CO_2 is a good transitional fluid for which the critical point temperature and pressure are relatively low and hence the MEMS structures are not destroyed. Hence, in the critical point drying machine, initially the isopropanol is replaced with liquid CO_2 slowly and then liquid CO_2 is dried. After the critical point drying the device is developed with the structure as in Fig. 5.1 H.

5.9 Fabricated product

To view the patterns in the device after fabrication SEM images are developed by scanning the sample with a focused beam of electrons. This helps in analyzing the results conducted during the experiment. It can be seen in Fig. 5.3 that TE tapers are not suspended. The cross-sectional pattern of the MEMS TPR is viewable in Fig. 5.4. However, the dimensions of the stair waveguide are 160×260 nm as patterning 200×230 nm is challenging in the lab environment setup. However, the TM gratings and tapers both are suspended and can be viewed in Fig. 5.5 and Fig. 5.7. In Fig. 5.5 the bridges are visible which holds the suspending waveguide and taper. In Fig. 5.7, the TM gratings can be seen. The gratings are suspended because of under-etching through the holes. The cross-section of the waveguide at the cantilever section can be seen in Fig. 5.6. A suspended PBS can be viewed in Fig. 5.2.

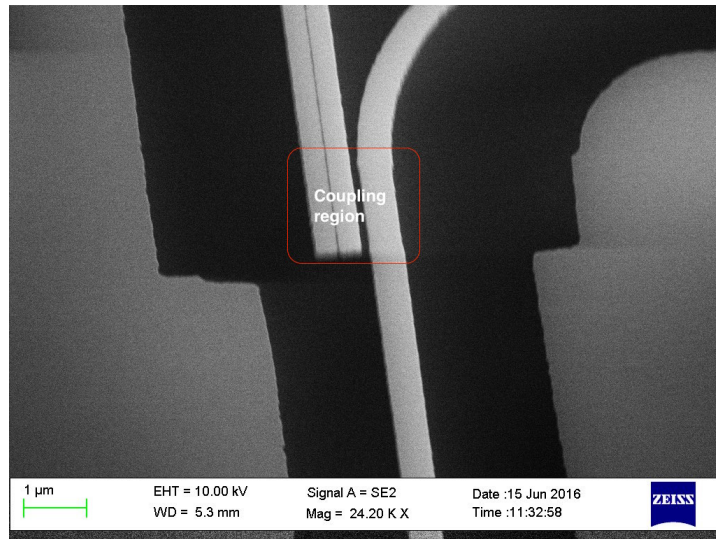


Figure 5.2: Suspended PBS with TM cross-port and TE through

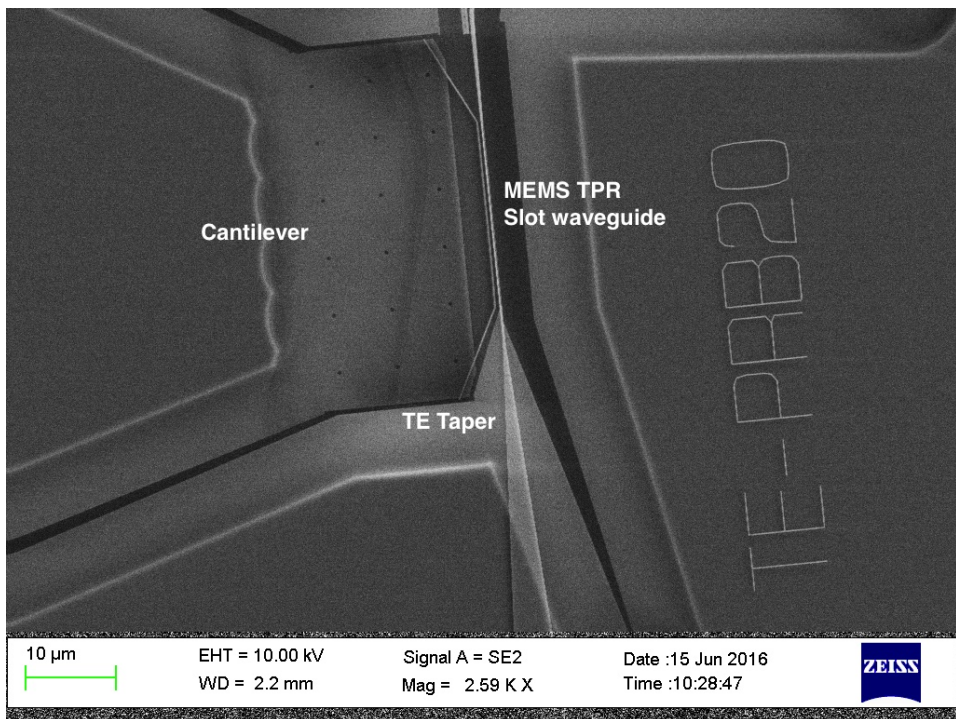


Figure 5.3: TE input with tapers, PBS and MEMS cantilever viewed in SEM

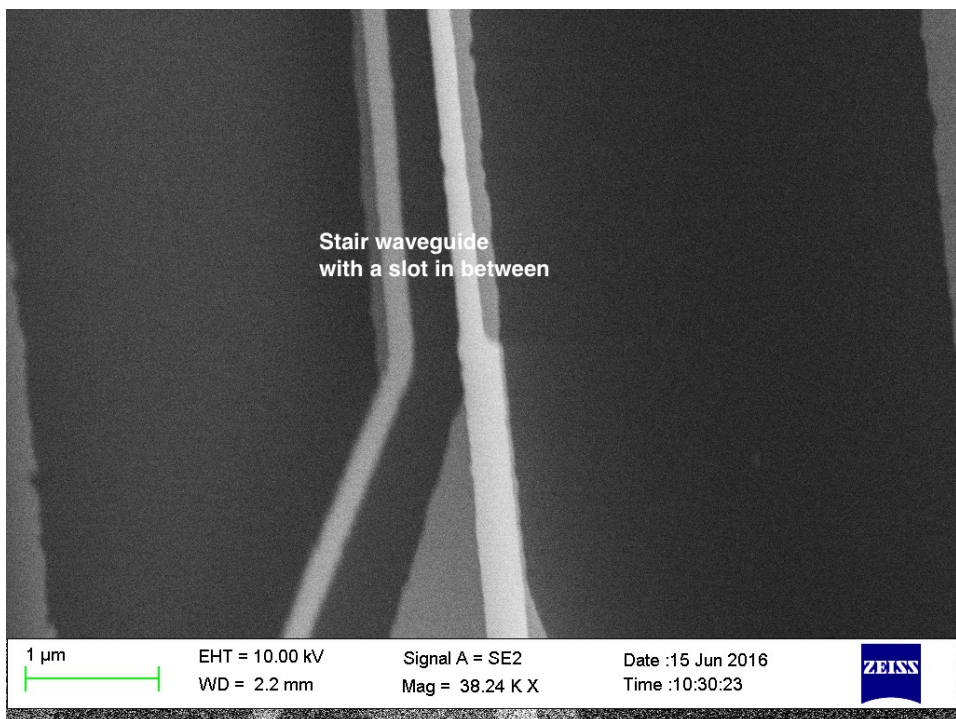


Figure 5.4: Cross-section with MEMS tuned waveguide and core waveguide for TE input.
Only the stair slot waveguide looks like the structure in Fig. 4.12

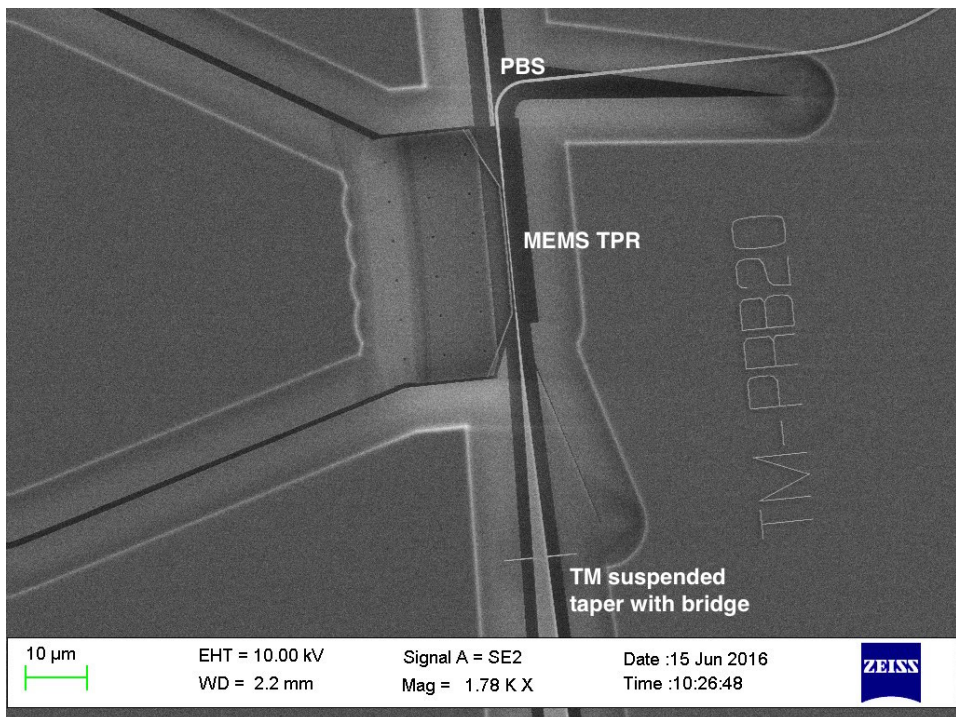


Figure 5.5: TM input with tapers, PBS and MEMS cantilever viewed under SEM

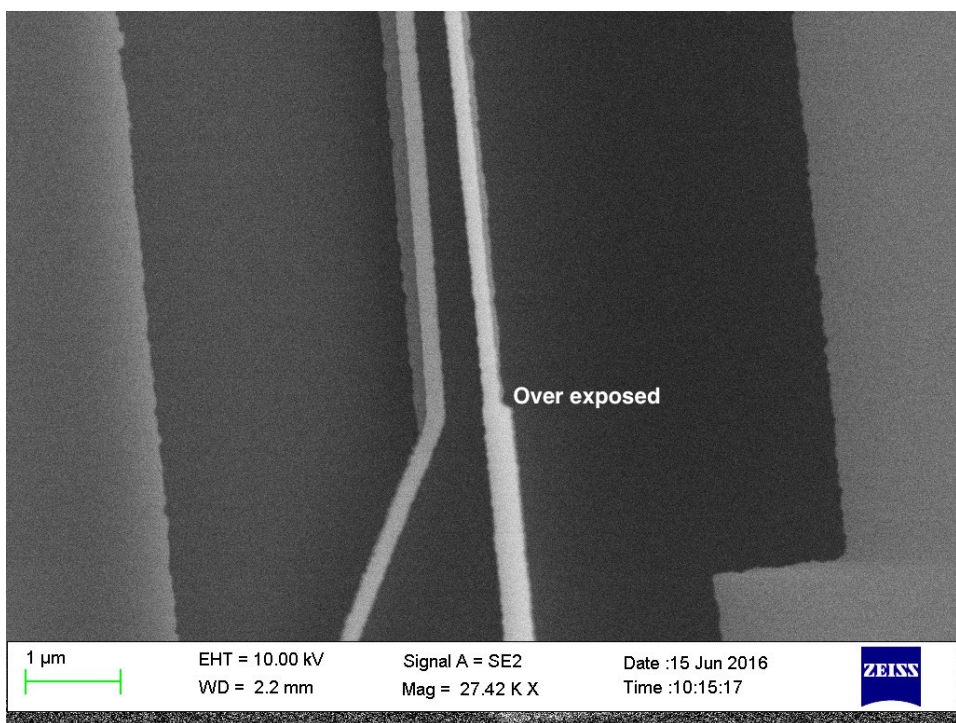


Figure 5.6: Cross-section in the slot region with MEMS tuned waveguide and core waveguide for TM input

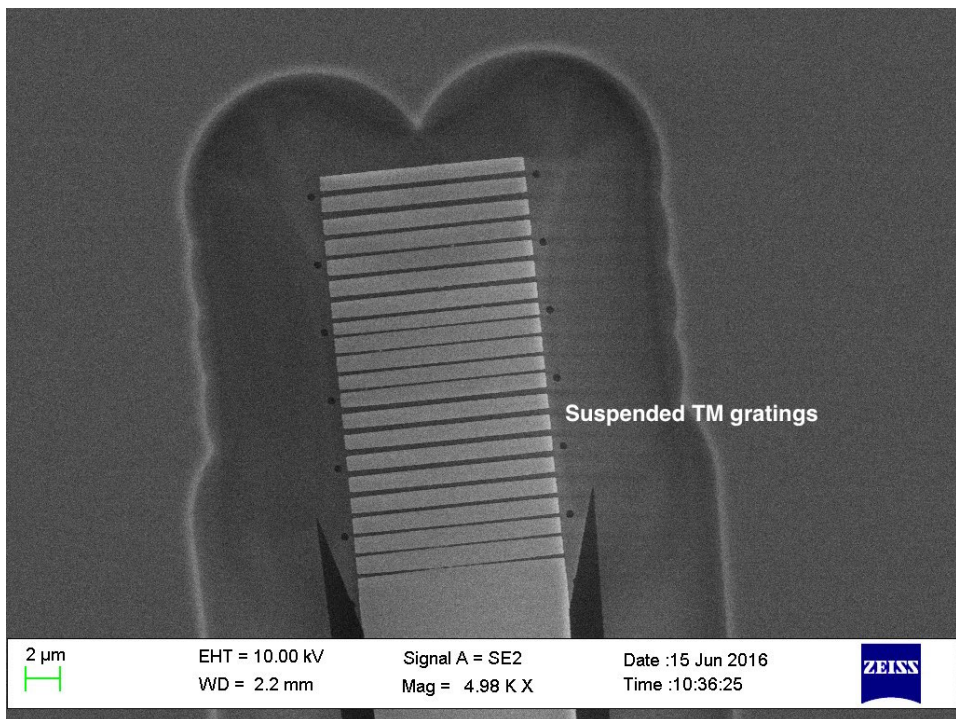


Figure 5.7: TM suspended gratings viewed under SEM

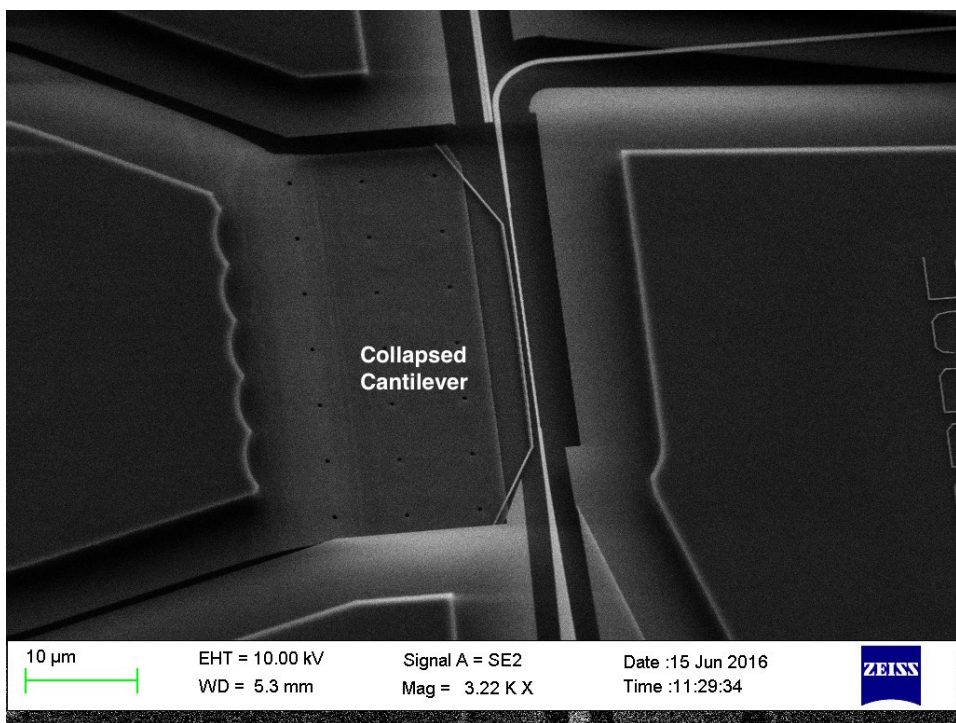


Figure 5.8: Stiction problem on applying a voltage more than the pull in voltage

6 Experiments

Chapter 6

6.1 Unit tests

To analyze the design various tests are performed. The strategy followed resembles similarity to unit tests where each of the components are tested and verified to understand the design. Also, the results are normalized to analyze the performance of MEMS TPR. The test cases followed during the fabrication process are discussed below.

- **Dose test:** The first test requires to verify the dose of HSQ and ZEP7000 (ZEP) used in masking to prevent the damage of masked Si. For this different doses are applied on different portion of the chip by using similar CAD model.
- **TE/TM—TE/TM grating with a normal waveguide:** To check any optical design it is necessary to couple the light into the chip with good transmission. That is why gratings are necessary. To check PR design, it was necessary first to check the TE and TM transmissions. Hence, the first test case was to check the TE/TM grating with a normal waveguide. This give an idea of transmission parameters and the next results were referenced to this value. This test ensured that the gratings worked as intended.
- **TE/TM—TE/TM grating with tapers:** The next test was to check the transmission parameters of the tapers, which was obtained by just putting the tapers end-to-end after the gratings from both ends. In this test it was made sure that the TE and TM modes were guided through the tapers.
- **TE/TM—TM/TE grating with taper, normal waveguide and PBS:** Next it was necessary to check the PBS design based on asymmetrical directional coupler, required for the characterization of the converted modes. This test ensures that both TE and TM mode can be guided to the respective ports and the PER can be measured.
- **TE/TM—TE/TM grating with taper and thinner waveguide:** Since, the PR was on a thinner waveguide of thickness 230 nm whereas the gratings had a thickness of 12 μm , it was necessary to use tapers to connect the gratings to the PR section. But before checking the PR, it was necessary to check if the transmission in a normal waveguide without the PR. That is why this test was performed.

- **TE/TM grating with PR and PBS:** Now that all the auxiliary components have been tested, the PR design was tested as well with PBS and TE/TM grating for different lengths with taper.
- **Cantilever actuation with separation strategy:** Since, the actuation is done by applying a voltage it is necessary to check that the cantilever actuates properly on applying voltage and does not stick after removal of voltage. This is done by segregating the cantilever portion from other parts of the chip so that other portions of the chip are not affected.
- **TE/TM Grating with PR, PBS, MEMS waveguide and actuation:** Finally, if all the previous tests have succeeded, the final design is tested with all the components and characterized.

The goal of the unit test strategy was to find and understand any short-comings which might occur at any stage of the fabricated process.

6.2 Characterization

An optical test bench setup was used to characterize the product. The test bench consisted of a LASER, microscope, optical fibers, polarizer and soft probes (for applying voltage to the chip without damaging it). A high level block diagram of the whole schematic is depicted in Fig. 4.17. The experiments were performed at a wavelength of 1550 nm (since, telecommunications operate at this wave length) with a span of 50 nm. Moreover, since it was difficult to pattern the 200×230 nm cross-section in the PR section, a cross-section of 160×260 nm was designed by choosing from the points on graph in Fig. 4.2 to balance between PR and patterning.

6.2.1 Polarization beam splitter

To analyze the results of the MEMS TPR, first of all it was necessary to design the PBS and check the transmission in TE and TM ports. A well designed PBS helps in tracking both the TE and TM mode intensities in the two ports. If a TPR is achieved then in one port the mode intensity will increase/decrease while in the other port the mode intensity will decrease/increase at real time. With the help of a PBS design, the TE and TM modes can be segregated and that is why its design is very important. Moreover, since in the TM transmission the waveguide is under-etched, a suspended PBS was needed. Hence, based on the idea of slot waveguide mode coupling [67], a PBS was designed. The novelty of design in this thesis work lies in the fact that it is air cladded and is free-standing (helpful for sensing applications of deconfined modes), and can couple TM modes. Also, the length of the PBS section is only $1.4 \mu\text{m}$, which is the shortest designed PBS till date (according to my knowledge), with air cladding.

The notation TE-PBS-TE in Fig. 6.1 means that TE light is coupled into TE gratings and then it travels through PBS and finally goes through to the TE port. Initially, the

normal TE-TE transmission is checked. Then the transmission through the TE-PBS-TE is checked which follows the normal TE-TE transmission. Now, it can be seen that PER for TE transmission is more than 20 dB, which can be obtained by comparing TE-PBS-TE and TE-PBS-TM in 1525 nm - 1575 nm. Similarly, analysis with TM-PBS-TM and TM-PBS-TE gives a PER between 15 dB - 20 dB over the band from 1525 nm - 1575 nm.

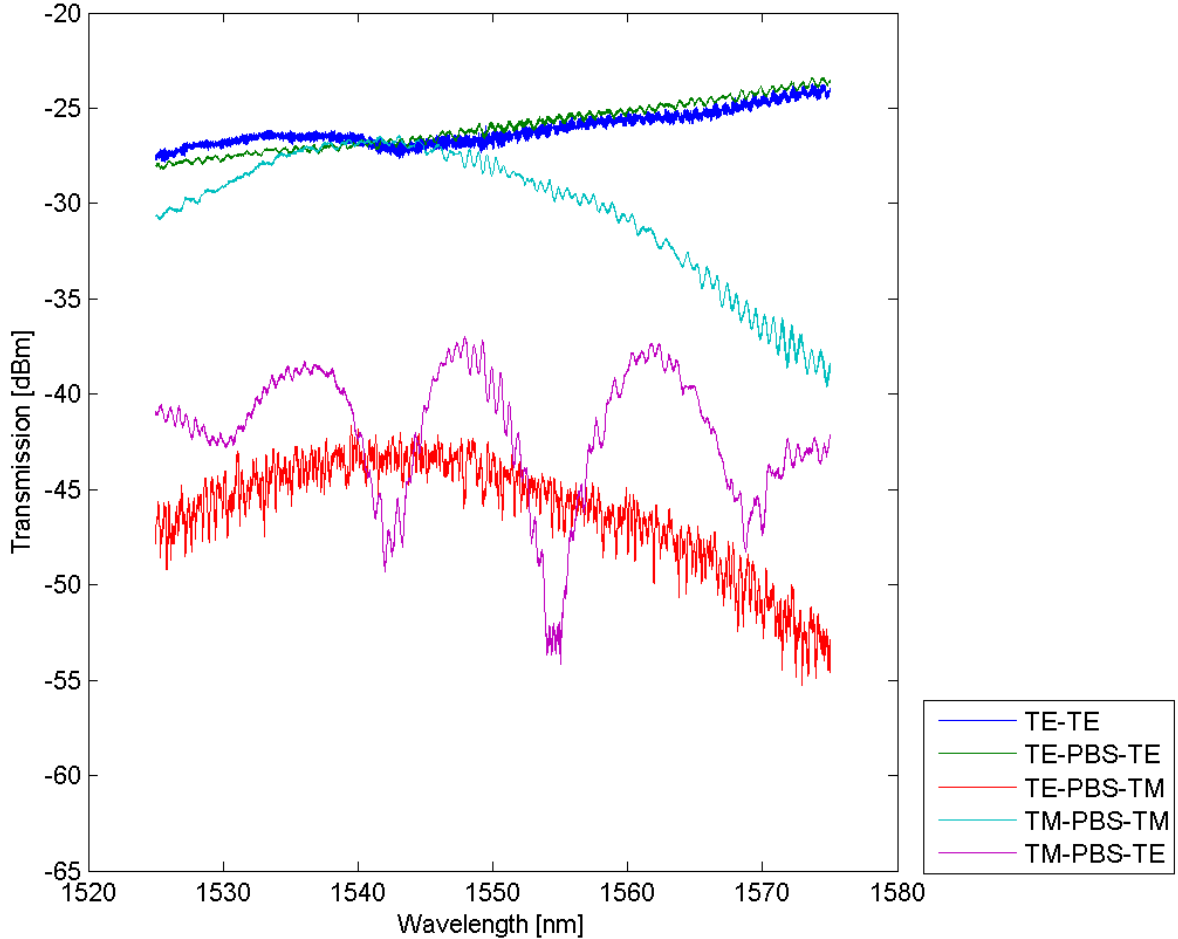


Figure 6.1: PBS with TE/TM input

6.2.2 Passive polarization rotator

To analyze the data of the TPR it is necessary to have a benchmark. Since, the idea of TPR is based on canceling the effect of passive PR the base measurements of polarization rotation by the PR will help to evaluate the results of TPR. Since, the cross-section of the stair waveguide is 160×260 nm the L_π is calculated accordingly. However, as the modes in the stair waveguide are deconfined, there can be coupling from the evanescent fields. That is why different L_π lengths are being tried out. In Fig. 6.2, the graph shows four plots which has TE input and both TE and TM outputs for different lengths of L_π . The notation TE – PRB20 – TM_{pas} means that the input is TE and it passes through a

passive PR of length 20 μm and the output is TM. The results in Fig. 6.2 shows that the passive PR is rotating polarization by around 5 dB after comparing it to Fig. 6.1. In this passive PR, the TE transmission has shifted down by 5 dB - 10 dB, whereas, the TM transmission has been lifted up by 5 dB - 10 dB, which can be seen by comparing Fig. 6.2 and Fig. 6.1.

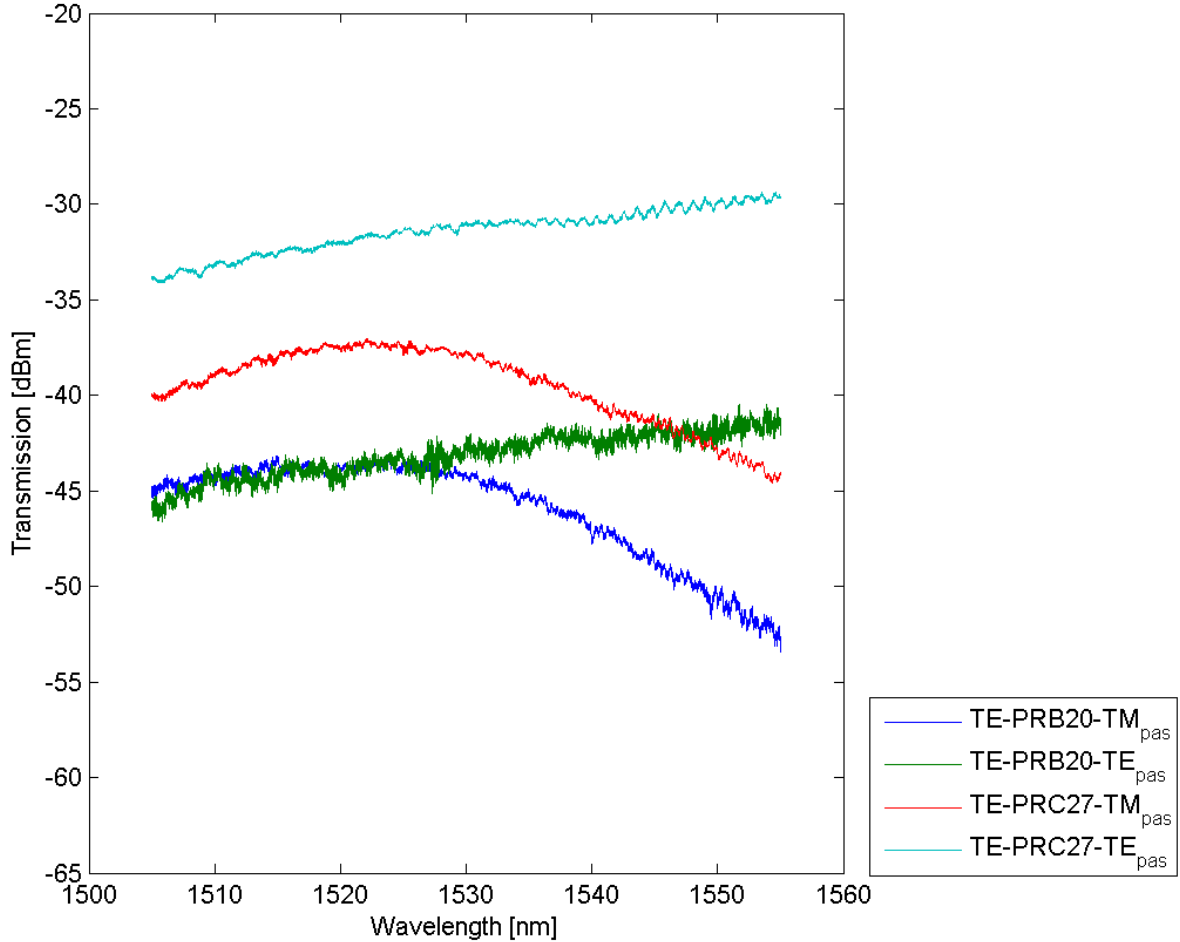


Figure 6.2: Passive PR with TE input for different cross-section lengths

6.2.3 Active polarization rotator

To characterize the TPR, it is necessary to normalize the results from the results obtained from the PBS in 6.1. Also, due to the coupling of the evanescent fields in the deconfined modes, different L_π lengths are being tried out ($L_\pi = 25 \mu\text{m}, 20 \mu\text{m}$).

As seen in Fig. 6.3, at 0 V the TE-TE and TE-TM transmission follows the same curve as in 6.1. After applying 4 V, the TE-TE transmission drops by 3 dB - 5 dB, whereas, the TE-TM transmission increases by 5 dB - 10 dB over 1530 nm - 1575 nm wavelength spectrum. By applying 7 V, the TE - TE transmission decreases even further in the whole spectrum from 1525 nm - 1575 nm, except in 1530 nm - 1545 nm, where the

transmission increases by 1 dB - 2 dB, which might have occurred due to any abrupt wavelength dependent geometry in the PR cross-section. However, by applying 7 V, the TE - TM transmission increases in the whole spectrum from 1525 nm - 1575 nm as expected. However, when the voltage was tuned off, the TE-TE and TE-TM did not come back to their initial state as shown in Fig. 6.4 (labels: TE-PR25-TE(0Vback), TE-PR25-TM(0Vback)), which suggests that the cantilever might have been collapsed as shown in Fig. 5.8.

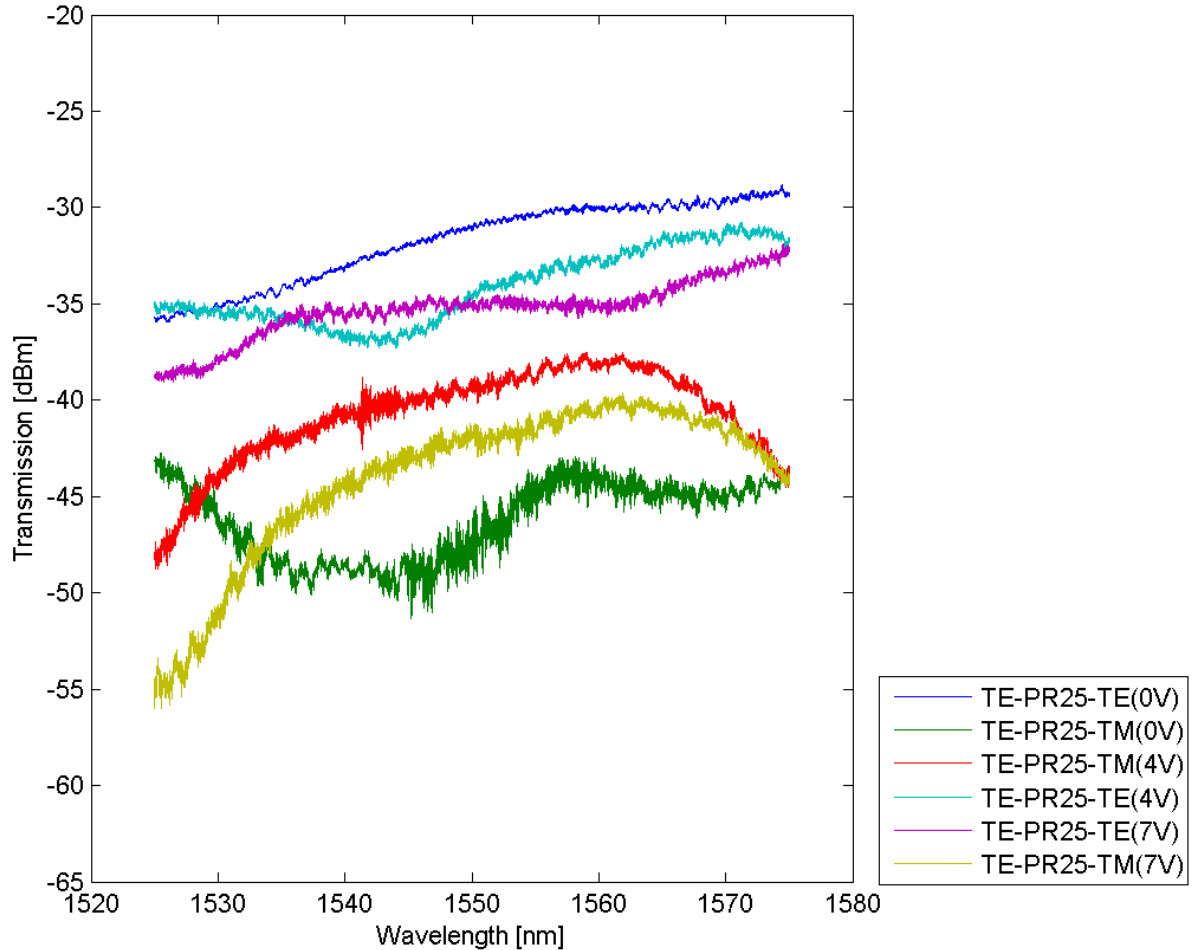


Figure 6.3: TPR with TE input at different voltage inputs for $L_\pi = 25 \mu\text{m}$

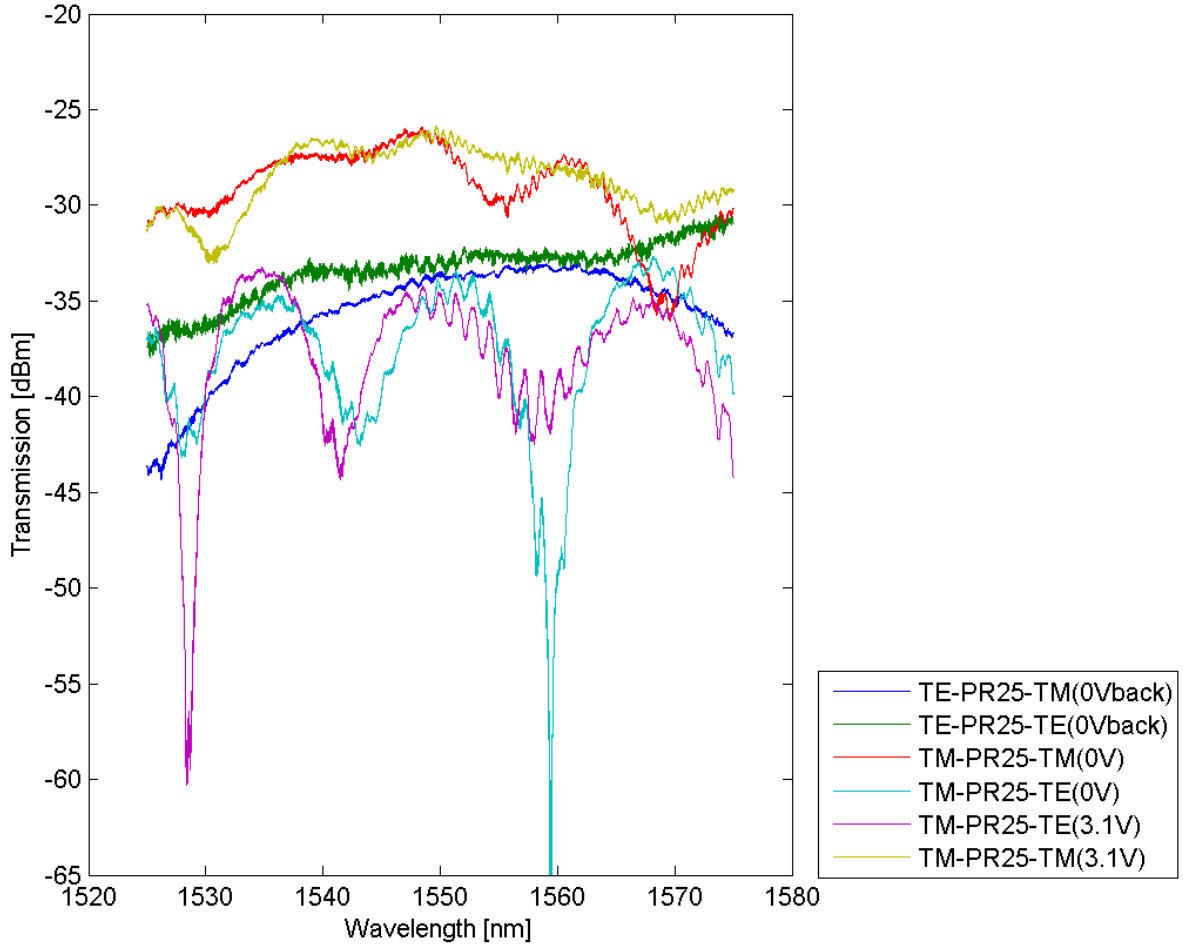


Figure 6.4: TPR with TM input at different voltage inputs for $L_\pi = 25 \mu\text{m}$

The TM-TE TPR shown in Fig. 6.4 does not show any promising results as the PR cross-section was not well patterned due to over-exposure during the fabrication which can be seen in Fig. 5.6. Also, there is a interference pattern in the TM-TE transmission which might have arise due to the under-etched cavity in the TM gratings and taper.

Finally, as shown in Fig. 6.5 the TE-TM TPR is analyzed for a cross-section length of $20 \mu\text{m}$. The results obtained at 0 V follows the simulation in Fig. 4.7. When applying 3 V and 3.4 V consecutively, the TE transmission drops by 1 dB and 6 dB, whereas, the TM transmission increases by 5 dB and 8 dB respectively in 1525 nm - 1570 nm wavelength spectrum.

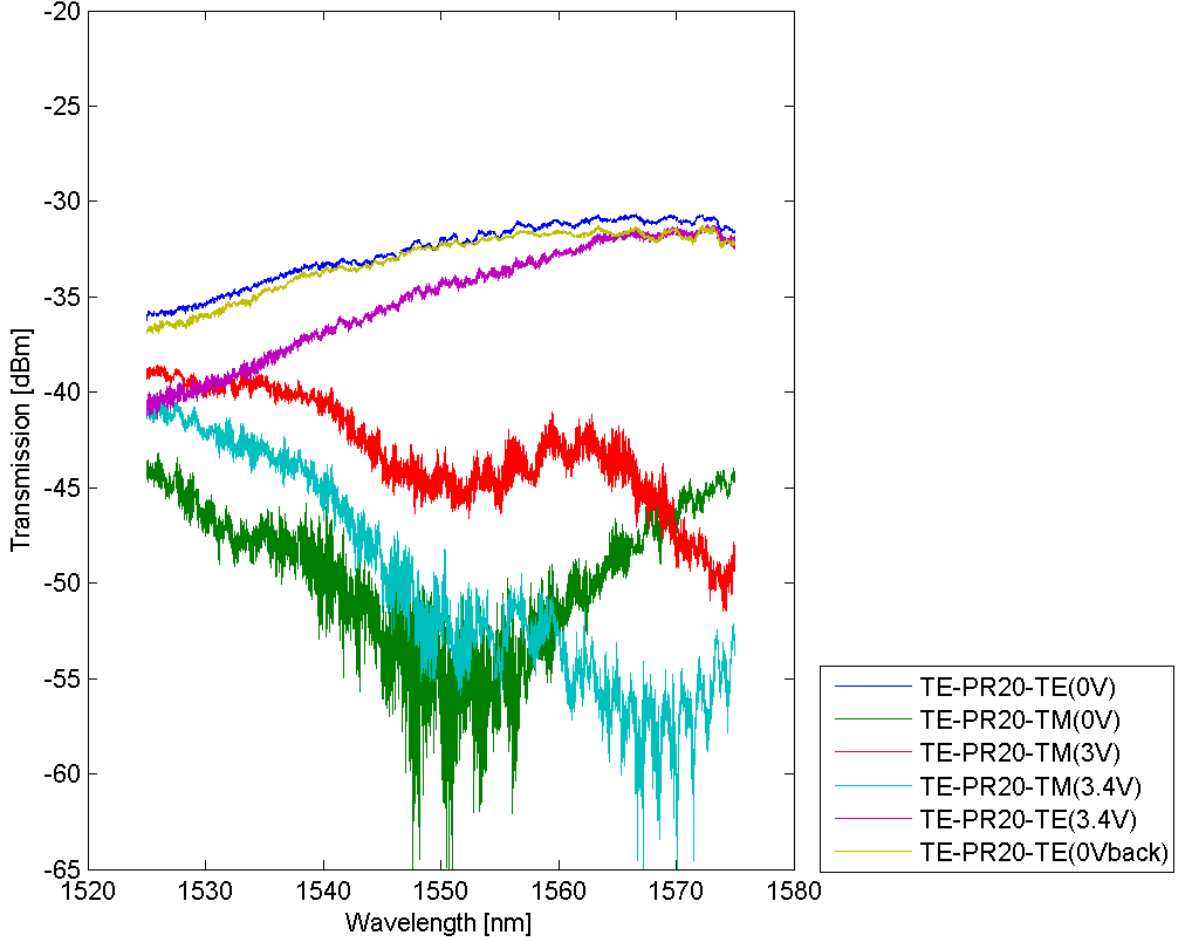


Figure 6.5: TPR with TM input at different voltage inputs for $L_\pi = 20 \mu\text{m}$

6.3 Analysis

The results obtained shows that the PBS works as intended with $\text{PER} \geq 20 \text{ dB}$ in 1525 nm - 1575 nm wavelength spectrum. However, some interference pattern arises in the TM transmission as a result of formation of standing waves due to the presence of under-etched cavity in the TM gratings and taper. Also, as seen in Fig. 5.6, the stair waveguide cross-section at the beginning of the PR is over-exposed in the TM input TPR. This might also induce reflections in the results obtained, which can create interference. Also, it is difficult to understand from the SEM the position of the cantilever. For the TPR to work, the cantilever must be in same plane or above, than the plane of the suspended bus waveguide. This can happen if the cantilevers are long. So, shorter cantilevers are required to fabricate in plane cantilevers and get promising results. Finally, from the results obtained it can be concluded that the concept of MEMS TPR works. Although, much more precise fabrication and characterization is necessary to achieve a high PER in the C and L bands. The current fabricated MEMS TPR with a length of $25 \mu\text{m}$, produces a PER of 5 dB - 10 dB in the 1530 nm - 1570 nm wavelength spectrum.

7

Chapter 7

Discussion

MEMS TPR can establish new horizons for on-chip integrated photonics. The power consumption of the MEMS TPR is very low and thus can be used for low powered devices. Furthermore, if the current problems are fixed, a cascade of MEMS TPR can be designed to yield broadband polarization rotation without the bandwidth constraints. The measurement setup developed during the thesis work with grating couplers, tapers and PBS can be reused further to test future integrated photonic components which uses TE and TM modes. Also, a shortest free-standing PBS with air cladding has been designed during this thesis, which can be useful for deconfined mode coupling with high packing density.

TPR designing principle	Length	PER	Bandwidth	Limitations
TPR using phase shifter [3.3.2.1]	~ 700 μm	40 dB	1530 - 1570 nm	Thermal cross-talk, Inefficient packing density
TPR using Berry's phase [3.3.2.2]	> 200 μm	19 dB	1556 - 1562 nm	Narrow bandwidth, Thermal cross-talk, Inefficient packing density
MEMS TPR	~ 25 μm	5 - 10 dB	1530 - 1570 nm	Low PER in the current fabricated product, MEMS cantilever stiction issue

Table 7.1: Comparative analysis of the MEMS TPR with the state-of-the-art TPR

The comparative analysis of the MEMS TPR designed in the thesis shows a significant improvement in terms of device length. Also, as the tuning is done mechanically, it is devoid of thermal cross-talk problem. Although, the MEMS TPR has some problems, it can be improved to achieve better results in terms of PER and bandwidth.

7.1 Limitations

The development process of the TPR gave a broad understanding of the working and fabrication of micro-optic based devices. The outcome of the understanding are discussed as follows:

- **Mode evolution design issue:** In the thesis work the mode hybridization based design is used for the TPR. However, in the literature review and simulation work performed, mode evolution based design showed promising results. But this design was not used since the length of the device is difficult to estimate. This estimation would have taken more fabrication iterations.
- **200×230 nm dimension stair waveguide, with a cantilever at 100 nm gap patterning problem:** In the simulation, the best dimensions of the stair waveguide were obtained at 200×230 nm. However, it is difficult to pattern such dimensions due to proximity effect. Hence, it was only possible to pattern a device dimension of 160×260 nm. Moreover, the gap between the MEMS waveguide and the passive PR waveguide was 100 nm during simulation. However due lateral stiction problem the MEMS waveguide and the passive PR were stuck together. Hence, a gap of 200 nm was used.
- **Thinner resist:** The resist used during the fabrication procedure must be thinner as thicker resist on the small device layer can break the device pattern.
- **Small write-field alignment:** Write-filed alignment is a very central adjustment in the process of getting the best possible e-beam lithographic result. Smaller write-field alignment ensures precise positioning of the stage under the e-beam deflection system.
- **Cantilever stiction problem:** If the MEMS cantilever are not characterized properly, they can stick to the bottom and can be damaged permanently.
- **Cantilever bending problem:** Longer cantilever bends in the fabrication process. Hence, it is necessary to design shorter cantilevers. Shorter cantilevers are stiffer and do not bend out of plane.
- **Dry-etching problem:** The gratings and the stair waveguide are designed for 110 nm slab height. However, the dry-etch procedure in the lab is difficult to control to achieve precise etching. So, device tolerance simulations should be performed to analyze the results.

7.2 Future work

Since, the MEMS TPR could not be developed with high PER due to several problems, the first step would be pattern the stair waveguide with optimized dimensions (200×230 nm with the MEMS cantilever at 100 nm gap) and characterize it. Then the mode

evolution design can be evaluated with a redesigned MEMS cantilever (for optimized PR cancellation) and tried out. Moreover, more simulations can be carried out on the cantilever design to avoid the stiction and out-of-plane bending problem. To make the device broadband a cascade of TPR design can be evaluated furthermore if necessary.

8

Chapter 8

Conclusions

The idea of electrically controllable optical polarization rotation, utilizing MEMS in silicon photonics establishes new horizons for on-chip integrated photonics. Dynamic control of optical polarization rotation can be utilized to realize a new class of components in integrated photonics including polarization mode modulators, multiplexers, filters, and switches for advanced optical signal processing, coherent communications, and sensing. The TPR can also be used for developing integrated polarization stabilizer, PMD mitigation, PDL mitigation and PMD and PDL measurement systems. Also, since the power consumption of the TPR is very low, this can be used for reconfiguration of network topology at low power. Additionally, TPR can help in multiplying the data rate of the existing deployed network infrastructure. Furthermore, the concept can be useful in situations where polarization tuning is necessary under adiabatic conditions e.g. in photon entanglement. Photon entanglement promises the development of even smaller micro-electronic devices along with secure communication channels, which can be very helpful in the future.

In this thesis work, the polarization tuning capability between the two fundamental modes (TE & TM) has been characterized. Although, the design was simulated to achieve a TPR in C and L bands with PER ≥ 10 dB, but at present, a PER of 5 dB - 10 dB was achieved for a limited bandwidth (1530 nm - 1570 nm) with a TPR length of 25 μm . In addition to the TPR, in this thesis work, a free standing PBS of length 1.4 μm with air cladding (the shortest reported to-date to our knowledge) is designed which can be helpful in spectrometric analysis of deconfined modes. Also, in this thesis, a test setup with grating couplers, TE tapers, free-standing TM tapers with bridges and PBS is developed which can be used further to evaluate integrated photonic components with smaller mode sizes. All these concepts and devices will be helpful in the future where only light would be the fundamental means of communication in integrated electronics.

Appendix A: Abbreviations

BPM Beam propagation method. 10

CAGR Compound Annual Growth Rate. 4

CMOS Complementary Metal-Oxide Semiconductor. 3, 4

EM Electromagnetic. 6, 8

FDTD Finite difference time domain. 10

FEM Finite element method. 10

FIT Finite integration technique. 10, 11

FOM figures of merit. 6, 19

HSQ Hydrogen silsesquioxane. 49–51, 53

IC Integrated Circuit(s). 3

ICT Information and Communication Technology. 2

IL Insertion loss. 20, 32

IoT Internet of Things. 1

MEMS Microelectromechanical systems. 4, 5, 21, 30, 32, 39–41, 49, 51–53, 56

NLC Nematic liquid crystals. 30

OEIC Optoelectronic Integrated Circuit(s). 3, 4, 22

PBS Polarization Beam Splitter. 43, 44, 46, 48, 52–54

PD λ polarization dependent wavelength characteristics. 4

PDL polarization dependent loss. 4, 18, 56

PER Polarization extinction ratio. 20, 24, 26–28, 32, 37, 48

PMD polarization mode dispersion. 4, 18, 56

PR Polarization Rotator. 4–6, 15, 21–29, 32, 33, 39, 40, 45, 51, 53, 54

RI Refractive index. 9, 11, 20, 22, 30, 36, 46, 47

SOI Silicon on Insulator. 49

SOP state of polarization. 6, 13, 15, 21, 28, 29

TE Transverse Electric. 9, 12–14, 19–24, 26, 35, 39, 40, 43, 44, 48, 52–54

TEM Transverse Electromagnetic. 8

TM Transverse Magnetic. 9, 12, 13, 19–24, 26, 35, 39, 40, 43, 44, 48, 52–54

TPPS Tunable polarization phase shifters. 27–29

TPR Tunable Polarization Rotator. 4, 5, 21, 32, 41, 43–45, 53, 56

ZEP ZEP7000. 53

Appendix B: Graph generation script

```
1 %% Initialize variables.
2 filename = '/Users/Sandipan/Desktop/Test/mems.csv';
3 delimiter = ',';
4 startRow = 6;
5
6 %% Format string for each line of text:
7 % For more information, see the TEXTSCAN documentation.
8 formatSpec = '%f%f%q%f%[^\\n\\r]';
9 fileID = fopen(filename, 'r');
10
11 %% Read columns of data according to format string.
12 dataArray = textscan(fileID, formatSpec, 'Delimiter',
13     delimiter, 'EmptyValue', NaN, 'HeaderLines', startRow-1,
14     'ReturnOnError', false);
13 fclose(fileID);
14
15 %% Allocate imported array to column variable names
16 K=100;
17 w_RR = dataArray{:, 1};
18 w_slab = dataArray{:, 2};
19 %Slab width actual sizie scaling
20 w_slab = w_slab + 0.15;
21 w_RR(:) = round(w_RR(:)*K);
22 w_slab(:) = round(w_slab(:)*K);
23
24 lambda = abs(str2double(dataArray{:, 3}));
25 % Ratio of the polarization
26 rp = abs(real(log10(dataArray{:, 4})));
27 k = lambda>=1;
28 sums = accumarray( { w_RR(k), w_slab(k)}, rp(k), [], [], [],
29     true );
29 [i,j,k] = find(sums);
30
31 %% Draw area chart
32 figure
33 hold on
```

```

34 matrix = [i/K j/K k];
35 tri = delaunay(matrix(:,1),matrix(:,2));
36 trisurf(tri,matrix(:,1),matrix(:,2),matrix(:,3))
37 shading faceted
38 grid on
39 hold off
40
41 %%Draw 5 max on graph
42 hold on
43 N = 5;
44 [sortedX, sortedInds] = sort(k(:), 'ascend');
45 topN = sortedInds(1:N);
46 [m] = ind2sub(size(k), topN);
47
48 h = scatter3(i(m)/K,j(m)/K,k(m), 'filled', 'MarkerFaceColor',
49 'red');
50 h.SizeData = 100;
51
52 text(i(m)/K,j(m)/K,k(m), strcat('(', num2str(i(m)/K), ',',
53 num2str(j(m)/K), ')'), 'HorizontalAlignment', 'left', 'Color',
54 'red', 'FontSize', 12)
55 hold off
56
57 %% Labels
58 xlabel('Rib width in \mu m', 'FontSize', 18, 'FontWeight', 'bold',
59 'Color', 'black')
60 ylabel('Base width in \mu m', 'FontSize', 18, 'FontWeight', 'bold',
61 'Color', 'black')
62 zlabel_eq = '$$\\sum_{mode}\\{abs\\left(log \\frac{E_{x_{mode}}}{E_{y_{mode}}}\\right)}$$';
63 zlabel(strcat('Log ratio of E-field = ', zlabel_eq), 'FontSize', 22, 'FontWeight', 'bold', 'Color', 'black', 'Interpreter', 'latex')
64
65 %% Clear temporary variables
66 clearvars filename delimiter startRow formatSpec fileID
67 dataArray ans;

```

Bibliography

- [1] "Gartner says the internet of things installed base will grow to 26 billion units by 2020." <http://www.gartner.com/newsroom/id/2636073>, 2013. [Online; accessed 26-Jan-2016].
- [2] "Internet of things connected devices to almost triple to over 38 billion units by 2020." <http://www.juniperresearch.com/press/press-releases/iot-connected-devices-to-triple-to-38-bn-by-2020>, 2016. [Online; accessed 09-June-2016].
- [3] "Ericsson Mobility Report: 70 percent of world's population using smartphones by 2020." <http://www.ericsson.com/news/1925907>, 2015. [Online; accessed 06-Feb-2016].
- [4] "Number of Internet Users (2015) - Internet Live Stats." <http://www.internetlivestats.com/internet-users/>, 2015. [Online; accessed 22-Jan-2016].
- [5] "Ericsson traffic exploration infographic." <http://www.ericsson.com/TET/trafficView/loadBasicEditor.ericsson>, 2015. [Online; accessed 06-Feb-2016].
- [6] "What Happens in an Internet Minute [Infographic] | Daily Infographic." <http://www.dailyinfographic.com/what-happens-in-an-internet-minute-infographic>, 2013. [Online; accessed 29-Jan-2016].
- [7] "Silicon photonics." https://en.wikipedia.org/wiki/Silicon_photonics/, 2015. [Online; accessed 06-Feb-2016].
- [8] "ARK | Your Source for Intel® Product Specifications." <http://ark.intel.com/>, 2015. [Online; accessed 06-Feb-2016].
- [9] "Cisco Global Cloud Index: Forecast and Methodology, 2014–2019 White Paper." http://cisco.com/c/en/us/solutions/collateral/service-provider/global-cloud-index-gci/Cloud_Index_White_Paper.html. [Online; accessed 04-Feb-2016].
- [10] G. Reed and A. Knights, *Silicon Photonics: An Introduction*. Wiley, 2004.
- [11] N. Savage, "Linking Chips With Light." <http://spectrum.ieee.org/semiconductors/optoelectronics/linking-chips-with-light>, 2015. [Online; accessed 06-Feb-2016].

- [12] R. Stabile, A. Albores-Mejia, A. Rohit, and K. A. Williams, “Integrated optical switch matrices for packet data networks,” *Microsystems & Nanoengineering*, vol. 2, p. 15042, Jan. 2016.
- [13] M. C. Wu, T. J. Seok, S. Han, and N. Quack, “MEMS-Enabled Scalable Silicon Photonic Switches,” *Optics Letters*, p. FW3B.2, 2015.
- [14] D. Nikolova, S. Rumley, D. Calhoun, Q. Li, R. Hendry, P. Samadi, and K. Bergman, “Scaling silicon photonic switch fabrics for data center interconnection networks,” *Optics Express*, vol. 23, p. 1159, Jan. 2015.
- [15] L. Lu, L. Zhou, X. Li, and J. Chen, “Low-power 2x2 silicon electro-optic switches based on double-ring assisted Mach-Zehnder interferometers,” *Optics Letters*, vol. 39, p. 1633, Mar. 2014.
- [16] P. Dong, C. Xie, L. L. Buhl, Y.-K. Chen, J. H. Sinsky, and G. Raybon, “Silicon In-Phase/Quadrature Modulator With On-Chip Optical Equalizer,” *Journal of Lightwave Technology*, vol. 33, pp. 1191–1196, Mar. 2015.
- [17] C. Chen, C. He, D. Zhu, R. Guo, F. Zhang, and S. Pan, “Generation of a flat optical frequency comb based on a cascaded polarization modulator and phase modulator,” *Optics Letters*, vol. 38, p. 3137, Aug. 2013.
- [18] Y. Urino, Y. Noguchi, M. Noguchi, M. Imai, M. Yamagishi, S. Saitou, N. Hirayama, M. Takahashi, H. Takahashi, E. Saito, T. Shimizu, M. Okano, N. Hatori, M. Ishizaka, T. Yamamoto, T. Baba, T. Akagawa, S. Akiyama, T. Usuki, D. Okamoto, M. Miura, J. Fujikata, D. Shimura, H. Okayama, H. Yaegashi, T. Tsuchizawa, K. Yamada, M. Mori, T. Horikawa, T. Nakamura, and Y. Arakawa, “Demonstration of 12.5-Gbps Optical Interconnects Integrated with Lasers, Optical Splitters, Optical Modulators and Photodetectors on a Single Silicon Substrate,” *Optics Letters*, p. Tu.4.E.1, 2012.
- [19] C.-M. Chang, J. H. Sinsky, P. Dong, G. de Valicourt, and Y.-K. Chen, “High-power dual-fed traveling wave photodetector circuits in silicon photonics,” *Optics Express*, vol. 23, p. 22857, Aug. 2015.
- [20] S. Garcia and I. Gasulla, “Design of heterogeneous multicore fibers as sampled true-time delay lines,” *Optics Letters*, vol. 40, p. 621, Feb. 2015.
- [21] M. Mattarei, A. Canciamilla, S. Grillanda, and F. Morichetti, “Variable Symbol-Rate DPSK Receiver Based on Silicon Photonics Coupled-Resonator Delay Line,” *Journal of Lightwave Technology*, vol. 32, pp. 3317–3323, Oct. 2014.
- [22] S. Janz, A. Densmore, D.-x. Xu, P. Waldron, J. Lapointe, G. Lopinski, T. Mischki, P. Cheben, A. Delâge, B. Lamontagne, and J. H. Schmid, “Silicon Waveguide Photonics for Biosensing Applications,” *Optics Letters*, p. IWA1, 2007.

- [23] G. Lim, U. P. DeSilva, N. R. Quick, and A. Kar, "Laser optical gas sensor by photoexcitation effect on refractive index," *Applied Optics*, vol. 49, p. 1563, Mar. 2010.
- [24] E. Ryckeboer, R. Bockstaele, M. Vanslembrouck, and R. Baets, "Glucose sensing by waveguide-based absorption spectroscopy on a silicon chip," *Biomedical Optics Express*, vol. 5, p. 1636, May 2014.
- [25] B. Jalali and S. Fathpour, "Silicon Photonics," *Journal of Lightwave Technology*, vol. 24, pp. 4600–4615, Dec. 2006.
- [26] "Silicon photonics market to grow at CAGR of 38% from \$25m in 2013 to \$700m in 2024." http://www.semiconductor-today.com/news_items/2014/JUL/YOLE_180714.shtml, 2014. [Online; accessed 06-Feb-2016].
- [27] D. J. Richardson, J. M. Fini, and L. E. Nelson, "Space-division multiplexing in optical fibres," *Nat Photon*, vol. 7, pp. 354–362, May 2013. Review.
- [28] J. Hecht, "Is Keck's Law Coming to an End?." <http://spectrum.ieee.org/semiconductors/optoelectronics/is-kecks-law-coming-to-an-end>, Jan. 2016. [Online; accessed 18-Feb-2016].
- [29] A. Xie, L. Zhou, J. Chen, and X. Li, "Efficient silicon polarization rotator based on mode-hybridization in a double-stair waveguide," *Optics Express*, vol. 23, p. 3960, Feb. 2015.
- [30] A. V. Velasco, M. L. Calvo, P. Cheben, A. Ortega-Moñux, J. H. Schmid, C. A. Ramos, i. M. Fernandez, J. Lapointe, M. Vachon, S. Janz, and D.-X. Xu, "Ultracompact polarization converter with a dual subwavelength trench built in a silicon-on-insulator waveguide," *Optics Letters*, vol. 37, p. 365, Feb. 2012.
- [31] D. Leung, B. Rahman, and K. Grattan, "Numerical Analysis of Asymmetric Silicon Nanowire Waveguide as Compact Polarization Rotator," *IEEE Photonics Journal*, vol. 3, pp. 381–389, June 2011.
- [32] J. Wang, B. Niu, Z. Sheng, A. Wu, X. Wang, S. Zou, M. Qi, and F. Gan, "Design of a SiO₂ top-cladding and compact polarization splitter-rotator based on a rib directional coupler," *Optics Express*, vol. 22, p. 4137, Feb. 2014.
- [33] D. Dai and J. E. Bowers, "Novel concept for ultracompact polarization splitter-rotator based on silicon nanowires," *Optics Express*, vol. 19, p. 10940, May 2011.
- [34] J. C. Wirth, J. Wang, B. Niu, Y. Xuan, L. Fan, L. Varghese, D. E. Leaird, and A. Weiner, "Efficient Silicon-on-Insulator Polarization Rotator based on Mode Evolution," *Optics Letters*, p. JW4A.83, 2012.
- [35] L. Chen, C. R. Doerr, and Y.-K. Chen, "Compact polarization rotator on silicon for polarization-diversified circuits," *Optics Letters*, vol. 36, p. 469, Feb. 2011.

- [36] J. D. Sarmiento-Merenguel, R. Halir, X. Le Roux, C. Alonso-Ramos, L. Vivien, P. Cheben, E. Durán-Valdeiglesias, I. Molina-Fernández, D. Marris-Morini, D.-X. Xu, J. H. Schmid, S. Janz, and A. Ortega-Moñux, “Demonstration of integrated polarization control with a 40 dB range in extinction ratio,” *Optica*, vol. 2, p. 1019, Dec. 2015.
- [37] Q. Xu, L. Chen, M. G. Wood, P. Sun, and R. M. Reano, “Electrically tunable optical polarization rotation on a silicon chip using Berry’s phase,” *Nature Communications*, vol. 5, p. 5337, Nov. 2014.
- [38] M. Ibrahim, J. H. Schmid, A. Aleali, P. Cheben, J. Lapointe, S. Janz, P. J. Bock, A. Densmore, B. Lamontagne, R. Ma, D.-X. Xu, and W. N. Ye, “Athermal silicon waveguides with bridged subwavelength gratings for TE and TM polarizations,” *Optics Express*, vol. 20, p. 18356, July 2012.
- [39] “Wave–particle duality.” https://en.wikipedia.org/wiki/Wave%20%93particle_duality, Jan. 2016. [Online; accessed 07-Feb-2016].
- [40] “Maxwell’s equations.” https://en.wikipedia.org/w/index.php?title=Maxwell%27s_equations&oldid=702587090, Jan. 2016. [Online; accessed 07-Feb-2016].
- [41] G. T. Reed, *Silicon Photonics: The State of the Art*. New York, NY, USA: Wiley-Interscience, 2008.
- [42] J. M. Burch and A. Gerald, *Introduction to Matrix Methods in Optics*. John Wiley & Sons, 1st ed., 1975.
- [43] J. Peatross and M. Ware, *Physics of Light and Optics*. 2015.
- [44] F. Flossmann, U. T. Schwarz, M. Maier, and M. R. Dennis, “Stokes parameters in the unfolding of an optical vortex through a birefringent crystal,” *Optics Express*, vol. 14, no. 23, p. 11402, 2006.
- [45] “Optical polarization waves.” http://www.wikiwand.com/en/Polarization_waves, 2015. [Online; accessed 09-Feb-2016].
- [46] J. M. Kahn, K.-P. Ho, and M. B. Shemirani, “Mode coupling effects in multi-mode fibers,” in *Optical Fiber Communication Conference*, p. OW3D.3, Optical Society of America, 2012.
- [47] H. Haus and W. Huang, “Coupled-mode theory,” *Proceedings of the IEEE*, vol. 79, pp. 1505–1518, Oct 1991.
- [48] “Polarization maintaining fiber.” https://en.wikipedia.org/wiki/Polarization-maintaining_optical_fiber, 2016. [Online; accessed 29-May-2016].

- [49] “Polarization control devices in industry.” <http://www.amstechnologies.com/es/products/optical-technologies/equipment/fiber-optic-test-measurement/measurement-of-fiber-properties/polarisation-mode/view/electrically-driven-polarization-controllers-scramblers/>, 2016. [Online; accessed 29-May-2016].
- [50] Y. Ding, H. Ou, and C. Peucheret, “Wideband polarization splitter and rotator with large fabrication tolerance and simple fabrication process,” *Opt. Lett.*, vol. 38, pp. 1227–1229, Apr 2013.
- [51] J. Zhang, M. Yu, G.-Q. Lo, and D.-L. Kwong, “Silicon-waveguide-based mode evolution polarization rotator,” *Selected Topics in Quantum Electronics, IEEE Journal of*, vol. 16, pp. 53–60, Jan 2010.
- [52] H. Zhang, S. Das, J. Zhang, Y. Huang, C. Li, S. Chen, H. Zhou, M. Yu, P. Guo-Qiang Lo, and J. T. L. Thong, “Efficient and broadband polarization rotator using horizontal slot waveguide for silicon photonics,” *Applied Physics Letters*, vol. 101, no. 2, 2012.
- [53] J. C. Wirth, J. Wang, B. Niu, Y. Xuan, L. Fan, L. Varghese, D. E. Leaird, and A. Weiner, “Efficient silicon-on-insulator polarization rotator based on mode evolution,” *Conference on Lasers and Electro-Optics 2012*, p. JW4A.83, 2012.
- [54] K. Goi, A. Oka, H. Kusaka, K. Ogawa, T.-Y. Liow, X. Tu, G.-Q. Lo, and D.-L. Kwong, “Low-loss partial rib polarization rotator consisting only of silicon core and silica cladding,” *Opt. Lett.*, vol. 40, pp. 1410–1413, Apr 2015.
- [55] H. Fukuda, K. Yamada, T. Tsuchizawa, T. Watanabe, H. Shinojima, and S. ichi Itabashi, “Polarization rotator based on silicon wire waveguides,” *Opt. Express*, vol. 16, pp. 2628–2635, Feb 2008.
- [56] D. Vermeulen, S. Selvaraja, P. Verheyen, P. Absil, W. Bogaerts, D. Van Thourhout, and G. Roelkens, “Silicon-on-insulator polarization rotator based on a symmetry breaking silicon overlay,” *Photonics Technology Letters, IEEE*, vol. 24, pp. 482–484, March 2012.
- [57] Z. Wang and D. Dai, “Ultrasmall Si-nanowire-based polarization rotator,” *Journal of the Optical Society of America B*, vol. 25, p. 747, May 2008.
- [58] M. Aamer, A. Gutierrez, A. Brumont, D. Vermeulen, G. Roelkens, J.-M. Fedeli, A. Hakansson, and P. Sanchis, “CMOS Compatible Silicon-on-Insulator Polarization Rotator Based on Symmetry Breaking of the Waveguide Cross Section,” *IEEE Photonics Technology Letters*, vol. 24, pp. 2031–2034, Nov. 2012.
- [59] R. Y. Chiao and Y.-S. Wu, “Manifestations of berry’s topological phase for the photon,” *Phys. Rev. Lett.*, vol. 57, pp. 933–936, Aug 1986.

- [60] A. Tomita and R. Y. Chiao, “Observation of berry’s topological phase by use of an optical fiber,” *Phys. Rev. Lett.*, vol. 57, pp. 937–940, Aug 1986.
- [61] I. Elfadel and G. Fettweis, *3D Stacked Chips: From Emerging Processes to Heterogeneous Systems*. Springer International Publishing, 2016.
- [62] W. D. Cort, J. Beeckman, R. James, F. A. Fernández, R. Baets, and K. Neyts, “Tuning of silicon-on-insulator ring resonators with liquid crystal cladding using the longitudinal field component,” *Opt. Lett.*, vol. 34, pp. 2054–2056, Jul 2009.
- [63] R. Soref and B. Bennett, “Electrooptical effects in silicon,” *IEEE Journal of Quantum Electronics*, vol. 23, no. 1, pp. 123–129, 1987.
- [64] COMSOL Development Core Team, *Comsol Multiphysics*. COMSOL, Stockholm, Sweden, 2016.
- [65] CST Development Core Team, *CST: 3D EM simulation software*. Computer Simulation Technology, Darmstadt, Germany, 2016.
- [66] “Grating couplers.” <https://www.kth.se/en/ees/omskolan/organisation/avdelningar/mst/research/optics/apodized-waveguide-to-fiber-surface-grating-couplers-1.315473>, 2016. [Online; accessed 28-May-2016].
- [67] D. Dai, Z. Wang, and J. E. Bowers, “Ultrashort broadband polarization beam splitter based on an asymmetrical directional coupler,” *Opt. Lett.*, vol. 36, pp. 2590–2592, Jul 2011.
- [68] C. Errando-Herranz, F. Niklaus, G. Stemme, and K. Gylfason, “A low-power MEMS tunable photonic ring resonator for reconfigurable optical networks,” in *2015 28th IEEE International Conference on Micro Electro Mechanical Systems (MEMS)*, pp. 53–56, Jan. 2015.
- [69] “Piranha solution.” https://en.wikipedia.org/wiki/Piranha_solution/, 2016. [Online; accessed 30-Apr-2016].
- [70] “Write field alignment.” <http://www.nanophys.kth.se/nanophys/facilities/nfl/manual/wfalign/align.html>, 2016. [Online; accessed 02-May-2016].